

AD-A067 075

MICHIGAN UNIV ANN ARBOR DEPT OF PHYSICS
THREE RESONANT NONLINEAR OPTICAL PROCESSES IN ATOMIC CESIUM. (U)
MAY 77 A V SMITH

F/G 7/4

AFOSR-77-3225

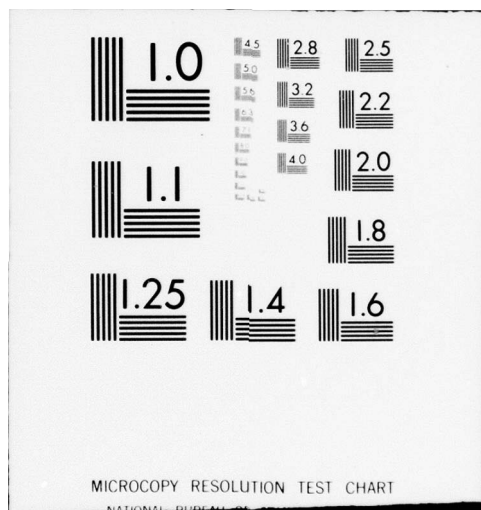
UNCLASSIFIED

AFOSR-TR-79-0366

NL

1 OF 2
AD
A067075





AFOSR-TR- 79 - 0366

LEVEL

(5)
Sc

Three Resonant Nonlinear Optical Processes in Atomic Cesium

ARLEE VIRGIL SMITH



May 1977

Supported in part by:
U.S. Air Force Office of Scientific Research



Department of Physics

Approved for public release;
distribution unlimited.

AIR FORCE OFFICE OF SCIENTIFIC RESEARCH (AFOSR)
NOTICE OF TRANSMITTAL TO DDC
This technical report has been reviewed and is
approved for public release IAW AFR 190-12 (7)
Distribution is unlimited.
A. D. MASON
Technical Information Officer

Approved for public release;
distribution unlimited.

DDC FILE COPY AD A067075

ABSTRACT

THREE RESONANT NONLINEAR OPTICAL PROCESSES IN ATOMIC CESIUM

by

Arlee Virgil Smith

Chairman: John F. Ward

We have investigated three resonant nonlinear processes in atomic cesium vapor. They are third harmonic generation, two photon absorption, and parametric frequency conversion. Resonant enhancement of each is provided by tuning the ruby laser near half the 6S - 9D transition frequency of $28828.90/\text{cm}^{-1}$. The parametric process involves, in addition, a resonance with one of the P states.

The experimental apparatus consists of a tuneable, narrow bandwidth, Q-switched, ruby laser with maximum power of 1 MW, a sample cell containing .1 torr or less of cesium vapor, and beam optics and optical detectors.

We have studied the variation of each of the three processes with laser intensity and frequency. At exact resonance the THG is found to be proportional to the square of the laser intensity and the TPA is proportional

→ next page

to laser intensity over a large power range. The resonance lineshape for both processes is found to be power dependent. A detailed analysis of these two processes based on steady state density matrix calculations and including A. C. Stark shifts, photoionization, and beam geometry is shown to accurately describe most of our observations.

Signals have been observed at 348 nm, 362 nm, 389 nm, 459 nm, 3 μm and 1.4 μm corresponding to transitions from 10P, 9P, 8P, and 7P to 6S and from $9D_{3/2}$ to 7P and 8P respectively and have been shown to be produced by a four photon parametric process. The signals are radiated colinearly with the laser beam and the four high frequency signals attain maximum powers of a few watts. Exponential gain has been measured for each at low powers and compared with calculated values of gain. Saturation is observed in each case. We show that this is probably caused by populating the P states. The effect of $9D_{3/2}$ population on the value of the gain coefficient is also discussed and shown to be important.

18 AFOSR

19 TR-77-0366

6

THREE RESONANT NONLINEAR OPTICAL PROCESSES
IN ATOMIC CESIUM,

9 Doctoral thesis

11 May 77

10

by

Arlee Virgil/Smith

12 156 p.

A dissertation submitted in partial fulfillment
of the requirements for the degree of
Doctor of Philosophy
(Physics)
in The University of Michigan
1977

15 ✓ AFOSR-77-3225

Doctoral Committee:

Professor John F. Ward, Chairman
Professor C. Wilbur Peters
Associate Professor Richard L. Sears
Professor Yukio Tomozawa
Associate Professor William L. Williams

228 720

slf

ACKNOWLEDGEMENTS

I thank Professor John Ward for providing me the opportunity to perform this research and for suggesting the topic. His physical insight and patient guidance throughout have been invaluable.

Kang Leung's help in the early stages of the work is gratefully appreciated. I thank also Irving Bigio for his advice and example while an officemate.

A special thanks to friend and colleague Charles Miller for his assistance and cooperation throughout and for his sense of humor.

I am especially grateful to my wife Elaine for cheerfully contributing many hours of work to the preparation of this manuscript and for her continued support and encouragement.

Finally, the financial support furnished by the United States Air Force Office of Scientific Research is acknowledged. Grant no. AFOSR-77-3225

ACCESSION for	
NTIS	Write Section <input checked="" type="checkbox"/>
DOC	Bull Section <input type="checkbox"/>
UNANNOUNCED	<input type="checkbox"/>
JUSTIFICATION	
BY	
DISTRIBUTION/AVAILABILITY CODES	
CONFIDENTIAL	
A	

TABLE OF CONTENTS

	Page
ACKNOWLEDGEMENTS	ii
LIST OF TABLES	v
LIST OF FIGURES	vi
LIST OF APPENDIXES	viii
CHAPTER 1. INTRODUCTION	1
CHAPTER 2. THE EXPERIMENTAL APPARATUS	8
2.1 The Cesium Cell	8
2.2 The Attenuator	13
2.3 The Detector & Monitor Boxes ...	13
2.4 The Data Acquisition System	17
2.5 The Laser	17
CHAPTER 3. BASIC THEORY OF TWO PHOTON ABSORPTION, THIRD HARMONIC GENERATION AND PARA- METRIC GAIN	26
3.1 Two Photon Absorption	30
3.2 Third Harmonic Generation	36
3.3 Parametric Gain	42
3.4 Summary	63
CHAPTER 4. THIRD HARMONIC AND TWO PHOTON ABSORP- TION EXPERIMENTS	65
4.1 Steady State Saturation Model ..	67

4.2	Comparison of Model and Experimental Results	81
4.3	Conclusions	108
CHAPTER 5.	PARAMETRIC FREQUENCY CONVERSION	109
5.1	The Data	110
5.2	Comparison of Data and Theory ..	113
5.3	Limitations of Theory and Modifications	121
5.4	Summary and Conclusions	127
APPENDIXES	129
REFERENCES	144

LIST OF TABLES

Table		Page
3.1	List of definitions and conventions	28
3.2	Matrix elements for atomic cesium	60
3.3	Calculated parametric gain coefficients and threshold powers	60
5.1	Comparison of measured and calculated power and density parametric gain coefficients and threshold powers	118

LIST OF FIGURES

Figure		Page
1.1	Energy level diagram of atomic cesium ..	6
2.1	Experimental layout	9
2.2	Cesium density calibration data	12
2.3	Fluorescence detection system	16
2.4	Laser cavity and tuning controls	19
2.5	Frequency dependence of laser tuning elements	20
2.6	Frequency calibration data	23
3.1	Graph of TPA cross section	35
3.2	Graph of THG efficiency	41
3.3	Graph of $\langle \chi_I^* \rangle$ for $x_9 = 0$	50
3.4	Graph of $\langle \chi_I^* \rangle$ for $x_9 = 1$	50
3.5	Graph of $\langle \chi_S \rangle$ for $x_9 = 0$	51
3.6	Graph of $\langle \chi_S \rangle$ for $x_9 = 1$	51
3.7	Graph of $\langle \chi_I^* \rangle \langle \chi_S \rangle$ for $x_9 = 0$	54
3.8	Graph of $\langle \chi_I^* \rangle \langle \chi_S \rangle$ for $x_9 = 1$	54
3.9	Lineshape of parametric gain for $x_9 = 0$.	56
3.10	Lineshape of parametric gain for $x_9 = 1$.	56
4.1	Measured power laws for TPA and THG	66
4.2	Calculated lineshapes for TPA	72
4.3	Calculated lineshapes for THG	72
4.4	Calculated power dependence of TPA	76
4.5	Calculated power dependence of THG	77

Figure		Page
4.6	Power law of THG with Stark shift	79
4.7	Oscilloscope traces of fluorescence	83
4.8	Fluorescence variation with cesium density	84
4.9	Hyperfine structure of atomic cesium ...	87
4.10	TPA and THG measured lineshapes (single mode laser)	90
4.11	Fit of computed and measured TPA line- shapes (single mode laser)	92
4.12	Fit of computed and measured THG line- shapes (single mode laser)	95
4.13	TPA and THG measured lineshapes (multi- mode laser)	97
4.14	Measured power laws of TPA and THG	98
4.15	Fit of computed and measured line- shapes (multimode laser)	99
4.16	Computed TPA power law	101
4.17	Computed THG power law	102
5.1	Observed signals and idlers	112
5.2	Temporal behavior of parametric signal .	112
5.3	Variation of 10P parametric signal with laser power	114
5.4	Variation of 9P, 8P, and 7P parametric signals with laser power	115
5.5	Variation of 8P and 10P parametric signals with cesium density	116
5.6	Lineshape of 10P parametric signal	120

LIST OF APPENDIXES

	Page
APPENDIX A. STEADY STATE DENSITY MATRIX CALCULATION	129
APPENDIX B. PHOTOIONIZATION OF $9D_{\frac{3}{2}}$ AND $6S_{\frac{1}{2}}$ STATES IN ATOMIC CESIUM	136
APPENDIX C. A. C. STARK SHIFTS OF THE $6S_{\frac{1}{2}}$ AND $9D_{\frac{3}{2}}$ STATES OF ATOMIC CESIUM BY 693.5 nm RADIATION	139

CHAPTER 1

INTRODUCTION

The electric polarization induced in matter by an applied electric field is, in general, nonlinear in the applied field. Consequently, for sufficiently small electric fields, it is useful to express the polarization as a power series in the field.

$$P = \mu + \chi_1 E + \chi_2 E^2 + \chi_3 E^3 + \dots \quad (1.1)$$

Here P represents the total electric polarization, μ the permanent polarization, E the applied field, and the coefficients (χ 's) are called susceptibilities.

The nonlinearity of P has many interesting consequences. For example, if χ_2 is nonzero and the electric field has a $\cos(\omega t)$ time dependence, then the term $\chi_2 E^2$ will produce polarization proportional to $\cos^2(\omega t)$ which has Fourier components at the frequencies 2ω and 0 . Likewise, the fourth term in the expansion, $\chi_3 E^3$, will produce polarization at the frequencies 3ω and ω , and higher order terms will generate various other harmonics. If the applied field has more than a single Fourier component, for example $E = E_1 \cos(\omega_1 t) + E_2 \cos(\omega_2 t)$, then the term $\chi_2 E^2$ will produce polarization at frequencies $(\omega_1 + \omega_2)$ and $(\omega_1 - \omega_2)$ as well as 0 , $2\omega_1$, and $2\omega_2$. The

fourth term will generate polarization at $(2\omega_1 + \omega_2)$, $(2\omega_1 - \omega_2)$, $(2\omega_2 + \omega_1)$, and so on.

The polarization which is induced at each point in the nonlinear material in turn radiates an electromagnetic wave with the same set of Fourier components as the polarization. The study of this phenomenon when the applied field has optical frequency components constitutes the field of nonlinear optics. Besides sum and difference frequency generation, such effects as self-induced transparency, optical nutation, Raman scattering, and multiphoton absorption are also included. Reviews of the subject may be found in articles by Giordmaine, Franken and Ward, and Bloembergen, among others.¹

The susceptibilities, although written as constants in eqn. 1.1, must, in general, be frequency dependent tensors in order to adequately relate applied electric fields of various directions of polarization and frequencies to the induced polarization of another polarization and frequency. The conventional notation for χ is illustrated in eqn. 1.2.

$$P_i^\omega = \chi_{ijk}(-\omega; \omega_1, \omega_2) E_j^{\omega_1} E_k^{\omega_2} \quad (1.2)$$

The subscripts here refer to the direction of polarization ($i, j, k = \hat{x}, \hat{y}, \hat{z}$) and the superscripts to the frequency. Each combination of Fourier components of the

applied field has a χ associated with it.

If the nonlinear sample material is an atomic gas, we can be more specific about the properties of the χ 's. The symmetry of the sample requires that all χ 's with an odd number of subscripts be zero and only certain tensor elements are allowed to be nonzero for χ 's with an even number of subscripts. To cite a familiar example, only diagonal elements of the linear susceptibility χ_{ij} are nonzero and they are equal ($\chi_{xx} = \chi_{yy} = \chi_{zz}$).

The form of the frequency response is also known for an atomic gas. For the example χ_{ij} , the response is described by the resonance denominator $D_1 = (\Omega - \omega)$ where Ω is $\omega_0 - \frac{i\Gamma}{2}$. Here ω_0 is a natural or resonance frequency and Γ is a damping factor. For χ_{ijklm} , the response is determined by the denominator $D_3 = (\Omega_a - \omega_1)(\Omega_b - \omega_2 - \omega_1)(\Omega_c - \omega_3 - \omega_2 - \omega_1)$.² This form leads to a variety of interesting phenomena including resonantly enhanced sum and difference frequency generation processes, two photon absorption or emission, and stimulated Raman scattering.

The present work is concerned primarily with resonant processes mediated by χ_{ijklm} in an atomic gas. Specifically, we have observed three resonant nonlinear processes in atomic cesium vapor. At least two of the applied fields are supplied by a ruby laser in each instance. The atomic cesium - ruby laser system is

convenient for the investigation of resonant processes because the laser is tunable over a range which includes the frequency $(E_{6S} - E_{9D_{3/2}})/2\hbar$, where E_{6S} and $E_{9D_{3/2}}$ are the energies of the 6S and $9D_{3/2}$ states of atomic cesium (see fig. 1.1). This means that the second term in the resonance denominator, D_3 , can be made very small. Each of the three processes and its relationship to this two photon resonance is described briefly below.

The first process is two photon absorption. When the laser is tuned to half the 6S - $9D_{3/2}$ transition frequency of cesium, two laser photons can be simultaneously absorbed by a ground state (6S) cesium atom inducing a transition to the $9D_{3/2}$ level. This nonlinear absorption is the consequence of χ_3 having an imaginary part in the same way that linear absorption is caused by the imaginary part of χ_1 . In this case the imaginary part of χ_3 is large at resonance because the middle term in the resonant denominator D_3 is imaginary.

The second process of interest is third harmonic generation. In this case, tuning the laser near the two photon resonance provides enhancement in the production of the third harmonic of the laser. Both real and imaginary parts of χ_3 contribute to this process. The energy levels involved in third harmonic generation are indicated in fig. 1.1.

The third process, parametric frequency conversion, can be regarded as two coupled difference frequency generating processes. One mixes the laser field with itself and with what is conventionally called the idler field to produce polarization at the signal frequency ω_S where $\omega_S = 2\omega_L - \omega_I$ (see fig. 1.1). The other mixes the laser field with itself and with the signal frequency field to produce the idler frequency polarization. Under some circumstances the coupling between these processes can provide positive feedback so that exponential growth of the signal and idler waves occurs. The end result is that energy is exchanged between the laser field and the signal and idler fields. Two resonances can provide enhancement of this process. One of them is the two photon resonance as before but the second is the single photon $6S - nP$ resonance, where n , the principle quantum number, can be 10, 9, 8, 7, or 6 (see fig. 1.1).

Each of these three nonlinear processes has been previously observed in a variety of nonlinear materials including atomic vapors.³ In particular, Leung has observed each in cesium vapor using much the same experimental apparatus we have employed.⁴ He observed the resonant enhancement of third harmonic generation obtained by tuning the laser to the two photon $6S - 9D_{3/2}$ resonance and demonstrated that it was correlated with

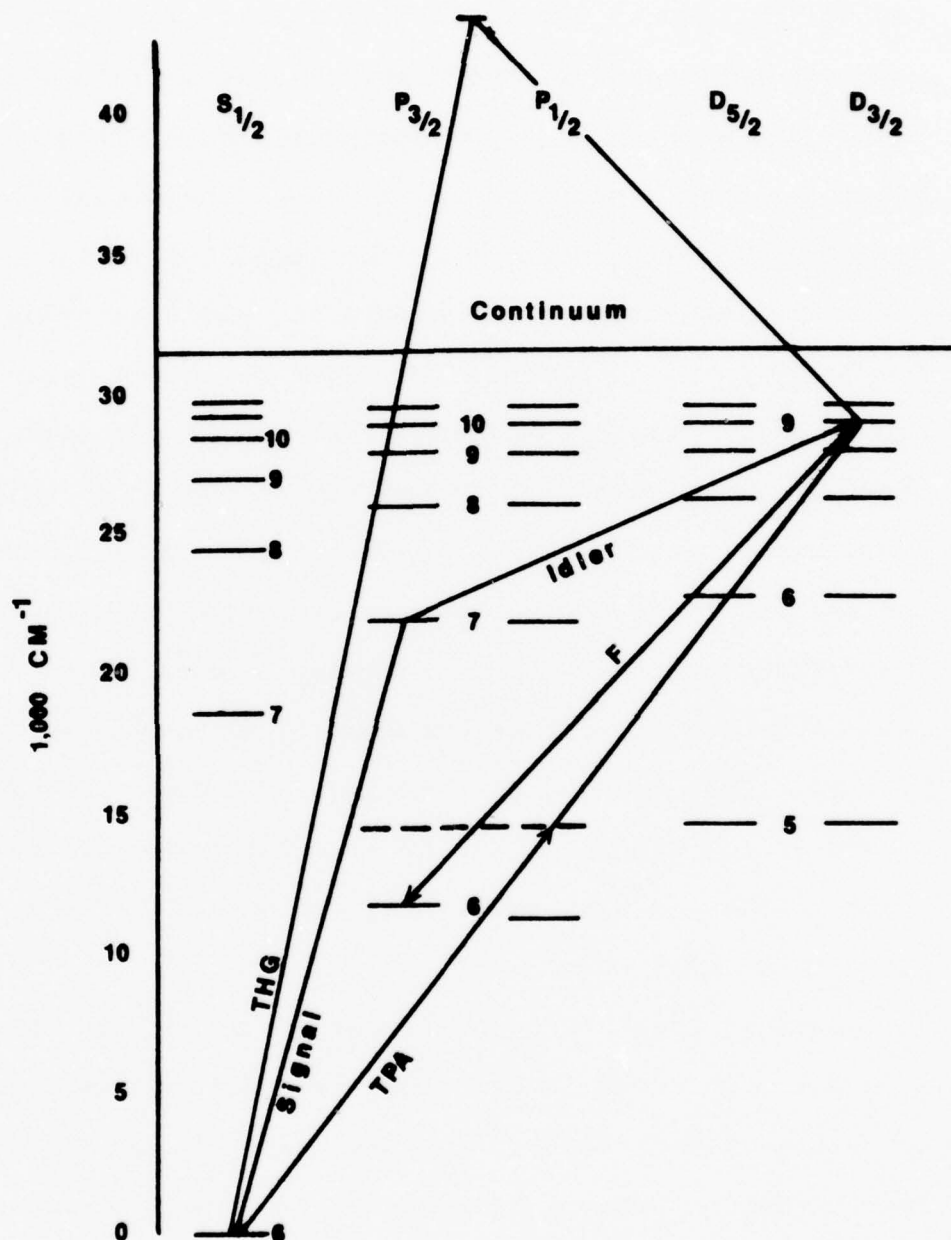


Fig. 1.1

Energy levels of atomic cesium and diagram
of the three nonlinear processes of interest.

two photon absorption. He also observed intense radiation at two of the $6S - nP$ transitions which were attributed to the parametric frequency conversion process.

This work should be considered an extension of Leung's observations. We have made more detailed measurements for each of the three processes emphasizing the dependence of each on laser intensity and laser frequency. The laser light source has been improved in bandwidth, mode structure, tunability, and stability compared with that used by Leung. The laser, other experimental apparatus, and experimental methods are described in chapter 2.

Our data involving third harmonic generation and two photon absorption is presented and discussed in chapter 4 and the parametric data and discussion are contained in chapter 5. In all three processes, important discrepancies are found between the observed behavior and that predicted by the simple theory of each which is presented in chapter three. Consequently, the theory is modified in chapters four and five to include such effects as saturation of atomic transitions, photoionization, and Stark shifts. We demonstrate that saturation of transitions is important in each case and limits frequency conversion efficiency.

CHAPTER 2

THE EXPERIMENTAL APPARATUS

The apparatus for a typical experiment consists of a tuneable ruby laser, a sample cell containing cesium vapor, three photomultiplier detectors and their associated optics, and an electronic data acquisition system. The laser is continuously tuneable in the range of 694.3 nm to 693.5 nm. Its wavelength is determined by the temperature of the ruby and by etalons in the laser cavity. Cesium vapor at pressures up to .5 torr is contained in a stainless steel cell fitted with three windows. Bursts of light are detected by the photomultipliers and the resulting electrical pulses are fed to the data acquisition system which digitizes the data. A more detailed description follows. See fig. 2.1 for a schematic diagram of the system.

2.1 The Cesium Cell

The cell containing the cesium vapor is about 20 cm long, constructed of stainless steel and fitted with three sapphire windows.⁴ It is lined with a thin sheet of copper felt in the central portion. These materials are chosen for their resistance to damage by the cesium. Before being filled with cesium, the cell is evacuated to about 10^{-7} torr and approximately one torr of neon is admitted to act as a buffer gas.

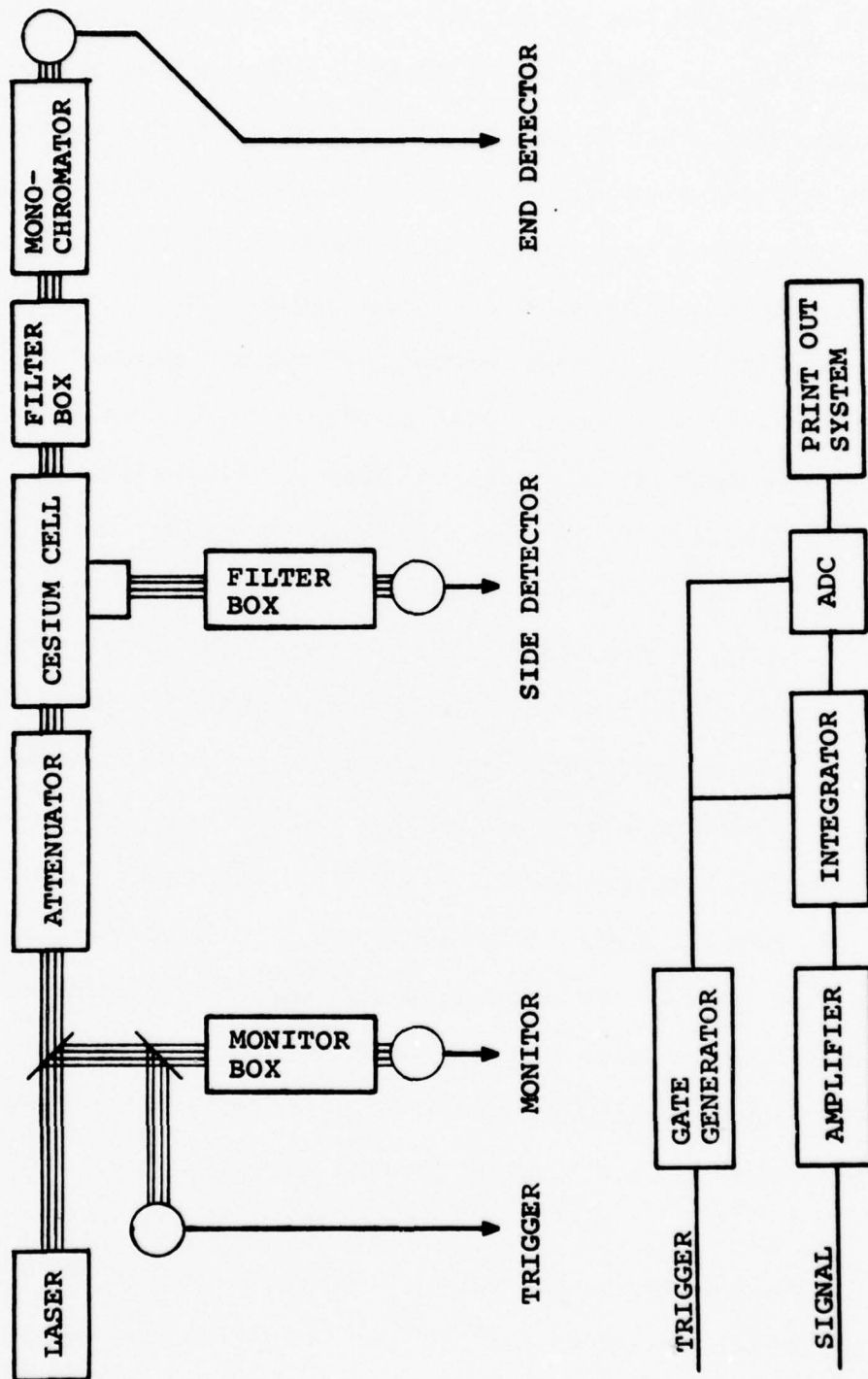


Fig. 2.1 Experimental layout

The distribution of cesium vapor inside the cell is determined by the temperature distribution of the cell. Basically, the central region is kept hot and the ends cool to produce a peaked distribution about 5 cm in width. Cesium vapor then circulates, being generated in the hot center and condensing at the cooler ends. The condensed liquid cesium is returned to the cell center by the copper felt which acts as a wick. The neon buffer gas ensures a gentle circulation and a smooth density distribution since its pressure is higher than that of cesium.

The vapor density is controlled by the temperature at the cell center. The signal from a thermocouple attached there is the input for a millivoltmeter and a time-proportioning temperature controller which maintains cell temperature within about 1°C of its set point. The useful temperature range is $100 - 300^{\circ}\text{C}$ corresponding to a cesium pressure range of roughly 10^{-4} to 1 torr. The temperature controller regulates the current through an insulated heating tape wound around the central part of the cell. The cooling is provided by water circulating through copper tubing wrapped around the cell near each end.

The cell windows are made of sapphire, which is more resistant to damage by hot cesium vapor than glass or fused quartz. Sapphire is a uniaxial crystal and its optical properties are temperature dependent. To prevent

problems, the end windows are maintained at a constant temperature somewhat higher than the rest of the cell. This ensures that no condensation on the windows can occur and that thermally induced changes in the optical properties are minimized. In addition the windows are oriented so that their optic axes lie in the plane of polarization of the laser light so that the polarization of light entering and exiting the cell is unaltered.

Since the integral of the cesium density along the length of the cell is the quantity of interest more often than the density at the cell center, the former is calibrated against cell temperatures. This is done by measuring THG versus cell temperature with the laser tuned near the cesium two photon resonance. A plot of this curve is shown in fig. 2.2. As will be shown in chapter 3, the signal at third harmonic is proportional to $\sin^2\left(\int_0^x \frac{\Delta k}{2} dx'\right)$ where Δk , the linear dispersion of cesium between third harmonic and laser frequencies, is proportional to cesium density. Thus the data of fig. 2.2 give a measure of the relative integrated density directly in coherence lengths where one coherence length (1 CL) is defined as the value of $\int N dx$ for which $\int \frac{\Delta k}{2} dz = \frac{\pi}{2}$. Most of the data will be presented with the number of coherence lengths as the unit of $\int N dx$. The conversion from coherence lengths to absolute density can be found in two ways. The first is to calculate Δk

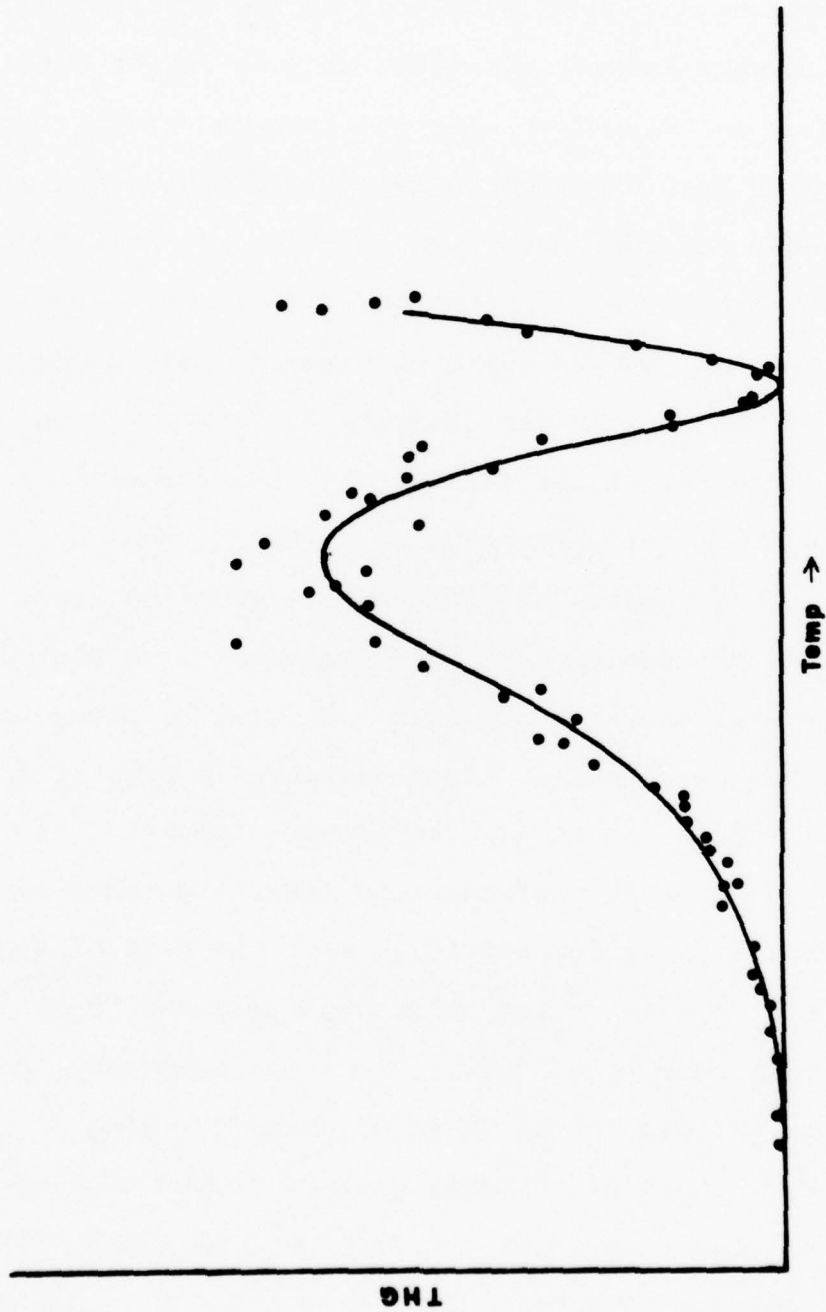


Fig. 2.2

and estimate the density distribution of cesium in the cell. The second is to use the data in fig. 2.2 and estimate the density and distribution at a specific number of coherence lengths. The two methods agree well that

$$1 \text{ CL} = .2 \text{ torr} \times 5 \text{ cm} \times 2^{\pm 1} \approx$$

$$4 \times 10^{15} \frac{\text{atoms}}{\text{cm}^3} \times 5 \text{ cm} \times 2^{\pm 1} \quad (2.1)$$

2.2 The Attenuator

The power of the radiation incident upon the cesium cell is systematically controlled by means of a variable attenuator while laser output is maintained at a constant level. This ensures that, at the cell, the beam characteristics such as time development and mode structure are constant while the power is varied. The attenuator is an absorption cell, filled with a solution of NiSO_4 in water, and has a path length variable from 0 - 15 mm. Transmission is calibrated by measuring power before and after the cell and is found to be $T = 10^{-t/5.6}$ where T is transmission and t is absorber thickness in mm.

2.3 The Detector & Monitor Boxes

There are three photomultiplier light detectors and associated optics (fig. 2.1). The first detector is

used to monitor the shot by shot performance of the laser. For this a fraction of the beam is split off by a pellicle reflector. The reflected beam is in turn split into two parts, one of which is directed to the trigger photodiode to trigger the data acquisition electronics. The remainder generates second harmonic in a quartz crystal. The harmonic is used because it is generally best to use an n th harmonic monitor if n th harmonic generation is being studied. The monitor and signal then both respond to fluctuations in the laser pulse shape in the same way so there is less scatter or systematic change in the ratio of signal to monitor. Third harmonic generation, two photon absorption, and parametric gain are of interest here so no single monitor is ideal. The second harmonic one is convenient, however, so it is used. Since there are no systematic changes in pulse shape this will not affect our results except to produce some additional scatter. The fundamental is removed by three centimeters of CuSO_4 solution and any other light is rejected by a narrow band interference filter leaving only the second harmonic to be detected by the RCA model 1P28 monitor photomultiplier. Its signal is fed to the monitor channel of the data acquisition system.

The fundamental or laser beam is next attenuated by the variable attenuator and in some cases focused into the center of the sample cell by an 18 cm focal length

lens. Light enters and exits the cell through the three sapphire windows which are transparent between 7000 and 200 nm.

The side detector located at the side window of the sample cell is used to measure the amount of fluorescence at 585 nm. The box contains a collecting lens, a CuSO_4 filter, a neutral density filter, a narrow bandpass interference filter at 585 nm and a 1P28 photomultiplier tube. Figure 2.3 is a diagram of this detector system.

The third detector looks at the third harmonic signal, one of the strong lines at the 6S to nP resonances, or any other radiation within the detector bandwidth (700 nm to 200 nm). The wavelength is selected by tuning a small quartz prism monochromator. The detector box contains an assortment of filters such as CuSO_4 , NiSO_4 , neutral density, and interference filters which is appropriate for the signal of interest. The phototube is a 1P28.

A different third detector (not shown) is used when infrared signals are under study. This consists of a gold-doped germanium detector operated at liquid nitrogen temperature, an interference filter at the proper wavelength, and colored glass filters to eliminate the laser light.

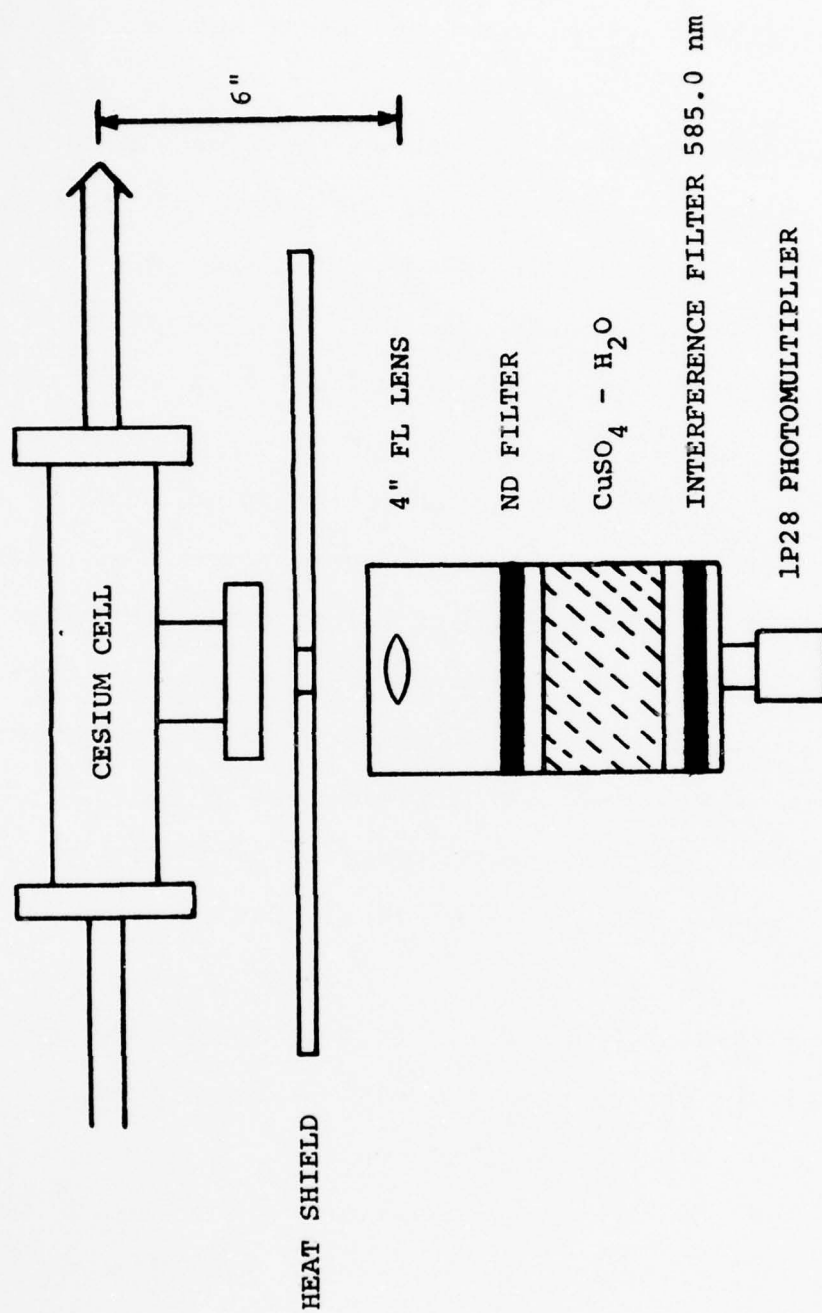


Fig. 2.3 Fluorescence detection system

2.4 The Data Acquisition System

There are three channels like the one drawn in figure 2.1 which share the gate generator.⁵ The pulses generated by the four photodetectors are routed via coaxial transmission lines to the electronics. The signals from the three photomultipliers are fed to three integrators and the fourth signal, the trigger, causes the gate generator to produce a pulse of preset duration adjusted to span the signal pulses. This pulse gates the integrators and strobes the ADCs. The voltage from each integrator is proportional to the charge from its photomultiplier and hence to the number of photons for that channel. The ADC converts this from an analog to a digital form and the result is typed out on a teletype. The net result is that each laser shot generates a print-out of three numbers proportional to the three signals. These data are then analyzed in a manner appropriate to the particular experiment.

2.5 The Laser

The laser is a Spacerays Model 1010c Q-switched ruby laser operated at about 1 MW peak power with pulse duration of twenty to fifty nanoseconds and a beam area of $.03 \text{ cm}^2$. The output has a narrow spectral width and is continuously tunable over the range of the two photon

resonance. Figure 2.4 is a schematic outline of the laser cavity.

The wavelength at which the laser operates is determined by three factors: the temperature of the ruby amplifying medium, the optical thickness of the front cavity reflector, and in some cases by the tuning of an intracavity etalon. The frequency dependences of these elements are shown in fig. 2.5.

The temperature of the ruby rod tunes the laser because the fluorescence peak of the lasing transition in ruby becomes narrower and shifts to shorter wavelength as the crystal is cooled. Since gain is large enough to support lasing only near the peak, the lasing frequency is determined within $.5 \text{ cm}^{-1}$ or so by ruby temperature. The lasing wavelength near 150°K is given by $\lambda_{\text{lasing}} = 693.54 + .0029 (T - 150)$ where the unit of λ is nm and that of T is degrees Kelvin.⁶

Ruby temperature is regulated by varying the rate of flow of liquid nitrogen past the rod. A temperature controller senses the temperature by a thermocouple attached to the rod holder and opens or closes a solenoid valve in the liquid nitrogen line as needed. In this manner the temperature at the time of firing the laser is maintained within about 1°K of the set point of the controller. The temperature actually cycles through a range of $3 - 5^\circ\text{K}$ with a period of 2 - 3 minutes and the

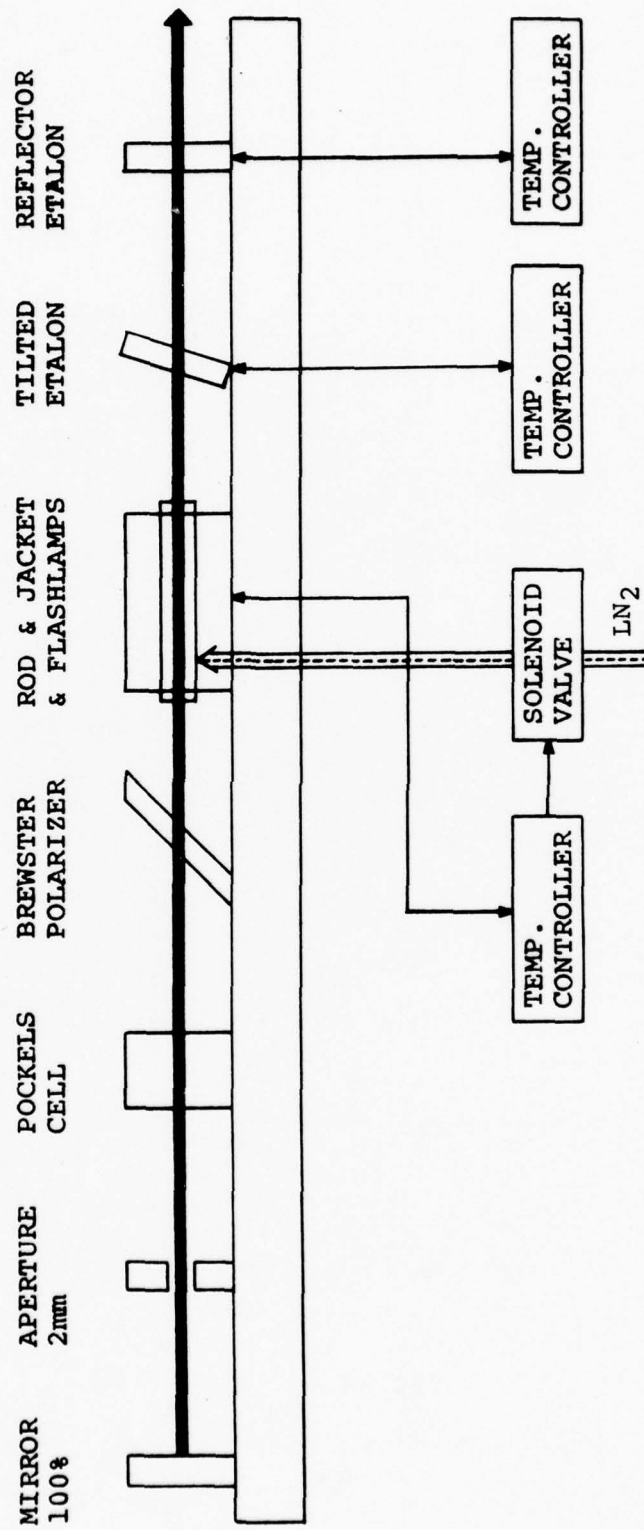


Fig. 2.4 Laser optical cavity and tuning system

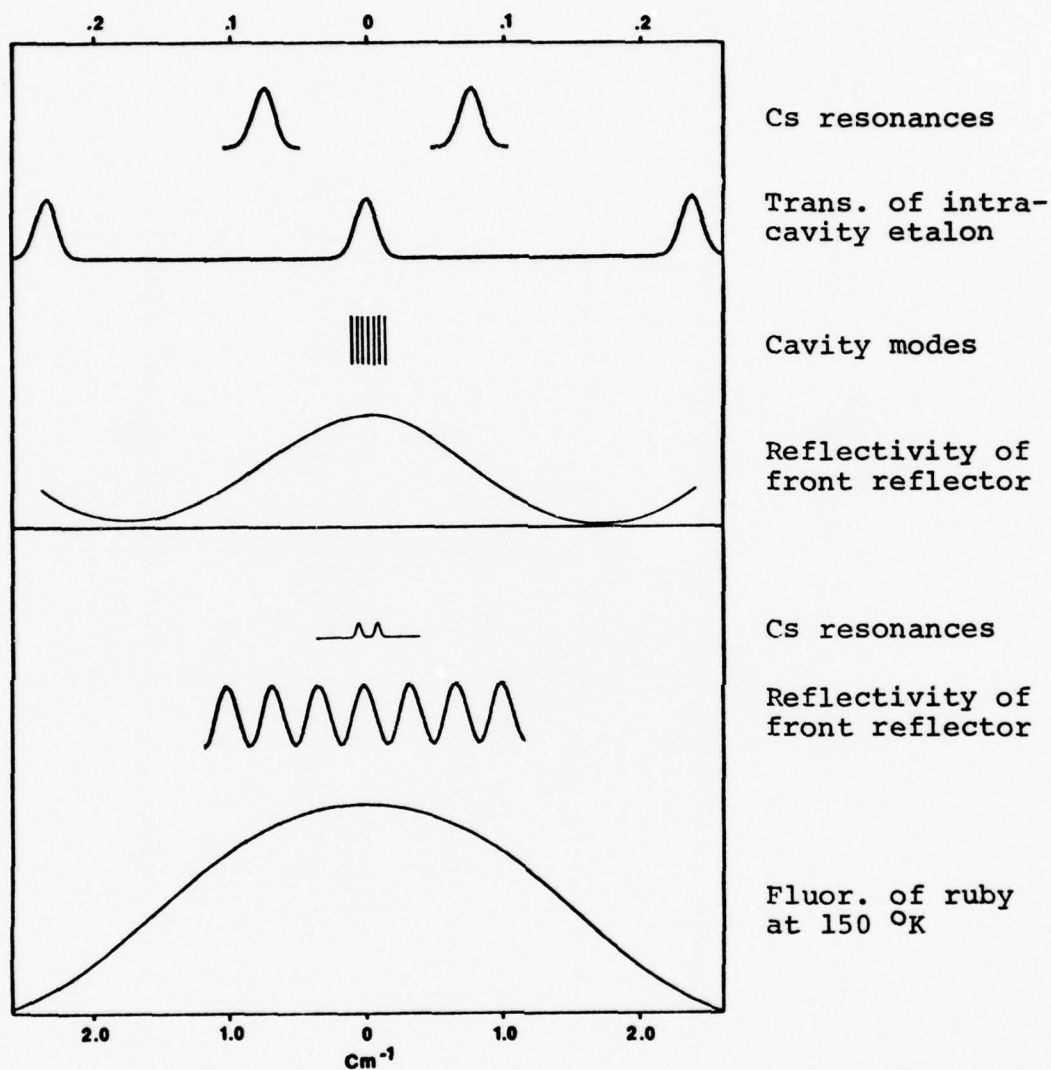


Fig. 2.5

Frequency dependence of laser tuning elements.

Note scale expansion by 10 in upper half.

laser is fired as it drifts through the proper temperature. The rod temperature necessary for resonance with cesium is about 150°K .

The second tuning element is the front reflector of the laser cavity. It consists of a temperature controlled, 1.0 cm thick, fused silica window with plane and parallel uncoated surfaces having the reflectivity indicated in fig. 2.5. Lasing is found to occur only within a small frequency range near the peaks of reflectivity and on only one such peak if that peak is near the ruby fluorescence maximum. In this case, usually 5 or 6 longitudinal modes of the laser cavity participate, and the intermode spacing is 125 Mhz. The ruby temperature is stable enough that lasing on only a single selected reflection peak is assured.

The positions of the reflectivity peaks are tuned by varying the temperature of the reflector and hence its optical thickness. Using the values of $\frac{1}{L} \frac{dL}{dT} = .06 \times 10^{-6}/^{\circ}\text{C}$ and $\frac{1}{n} \frac{dn}{dT} = 7 \times 10^{-6}/^{\circ}\text{C}$, where L is thickness and n is index of refraction,⁷ the tuning rate is determined to be one order per 2.5°C change in temperature. Since temperature stability is about $.05^{\circ}\text{C}$ the stability of the laser output is about $.005 \text{ cm}^{-1}$ with a width of about $.02 \text{ cm}^{-1}$. The relative distribution of power among the longitudinal modes is not constant, however, so effective stability is $\sim .01 \text{ cm}^{-1}$.

The tuning range is about 1 cm^{-1} . Most of the data was taken with these conditions.

To provide continuous tunability, the reflector and fluorescence peaks are brought into coincidence then tuned together to the desired frequency. The expected tuning is verified by examining the laser output with a Fabry-Perot interferometer. Figure 2.6 exhibits the resulting interferograms and a plot of the value of R^2 (where R is the radius of the ring in the photos) versus the ruby temperature. Knowledge of the plate separation allows a determination of the tuning curve in $\text{cm}^{-1}/^\circ\text{C}$ from the graph. The vertical lines and the sharper of the two ring patterns in each interferogram are produced by a helium-neon laser used to stabilize the Fabry-Perot. It is clear from the sloping lines in fig. 2.6 that tuning is well behaved. Similar interferograms reveal the spectral width and number of longitudinal modes in the laser output.

The third tuning element, the intracavity etalon, was used when a narrower spectral bandwidth was desired. When in place it allowed only one or two longitudinal modes to lase. Stability was sufficient to select any mode within the tuning range. Its insertion into the cavity lowered the power output by a factor of five or so, however, and the tuning range was decreased to about $.05 \text{ cm}^{-1}$.

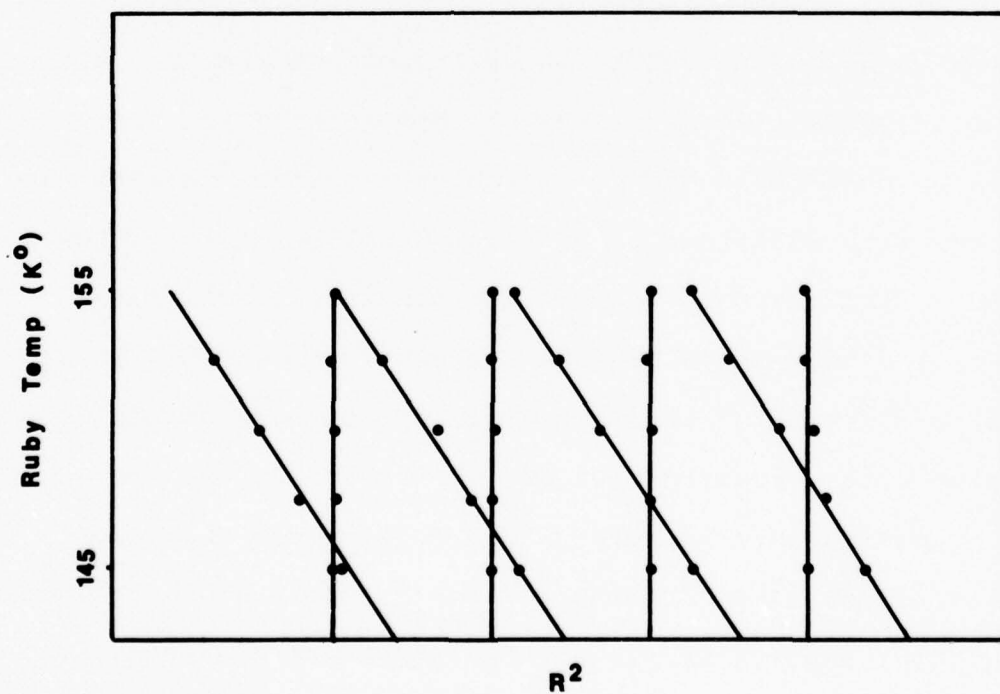
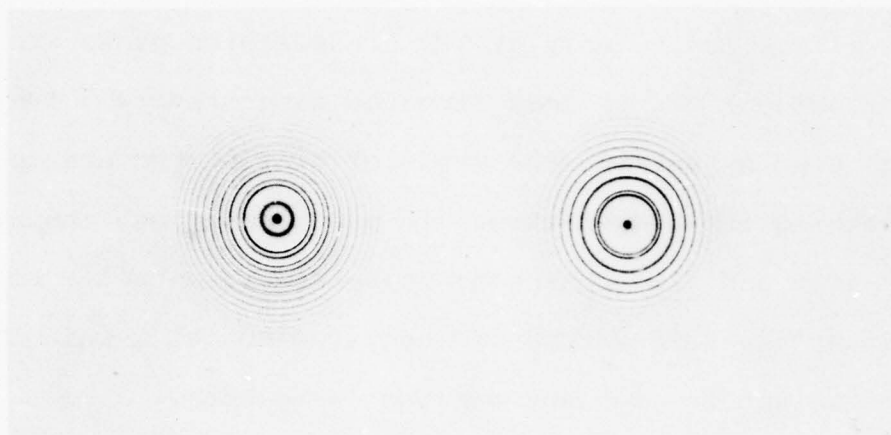


Fig. 2.6
Top: Fabry-Perot interferograms
Bottom: Frequency - ruby temp. calibration

This intracavity etalon is a solid, fused silica, two surface etalon with dielectric coatings of 80% reflectivity and a thickness of 1.47 cm. The finesse is about 15. It allows lasing only at its transmission peaks since reflected light is lost from the laser cavity. Tuning is achieved by varying the angle of tilt of the etalon or by changing its temperature. In practice, rough tuning is by tilt and fine tuning by temperature control. For the latter the temperature is regulated to $.01^{\circ}\text{C}$ which is sufficient to pick any desired laser mode.

Both the Fabry-Perot and a fast oscilloscope-photodiode combination (Tektronix 519 oscilloscope and ITT FW 114A photodiode with a combined rise time less than .5 ns) were used to study the output when the etalon was in place. The Fabry-Perot interference patterns revealed that there were only one or two modes lasing, and study with oscilloscope of the modulation of laser power due to interference between longitudinal laser modes verified this and showed that a single mode could be made to predominate, thus effectively producing a single mode laser with a power of 100 kW.

Unfortunately, this single mode operation was of limited usefulness because of the concomitant sacrifice in power and tuning range. The power was not sufficient for most of the experiments and the limited range made it

inconvenient as well. It was used in a few cases, however, where narrow bandwidth was essential.

CHAPTER 3

BASIC THEORY OF TWO PHOTON ABSORPTION, THIRD HARMONIC GENERATION AND PARAMETRIC GAIN

This chapter presents the basic theory for the three nonlinear processes of interest, and applies it to the specific case of ruby laser radiation interacting with cesium atoms. The primary concerns are evaluating the appropriate χ 's (see definitions in table 3.1), and solving driven wave equations in which the induced polarizations are the driving terms. These calculations indicate the size of the signals to be expected, their dependence upon laser intensity, their resonant behavior, and the effects of dispersion. Other factors such as hyperfine splittings, laser mode structure, absorption, and saturation are necessarily included in a full description of the processes, but a discussion of these is postponed until chapter 4.

Before proceeding with the theory of the individual processes, some discussion of the characteristics of the χ 's is in order. It was mentioned in the introductory chapter that χ is a tensor and depends on the frequencies of the applied fields. Taking a third order χ as an example, the polarization is written in the form

$$P_i^{\omega} = K \chi_{ijkl} (-\omega; \omega_1, \omega_2, \omega_3) E_j^{\omega_1} E_k^{\omega_2} E_l^{\omega_3} \quad (3.1)$$

to account for the tensor nature and frequency dependence of χ . The conventions are the following: P_i^ω is the amplitude of polarization in the direction i ($i=\hat{x}, \hat{y}, \text{ or } \hat{z}$) at the frequency ω produced by the three electric fields on the right hand side; $\omega = \omega_1 + \omega_2 + \omega_3$; K is listed in the definitions in table 3.1; the E 's are Fourier components of the applied field at the frequencies indicated by the superscript and with the polarization directions given by the subscripts; each combination of Fourier components has an element of χ associated with it.

In an isotropic medium such as cesium vapor, symmetry allows only those elements of the tensor $\{\chi_{ijkl}\}$ which are of the form χ_{iiii} , χ_{iijj} , χ_{ijij} , or χ_{ijji} ($j, i=\hat{x}, \hat{y}, \hat{z}; i \neq j$) to be nonzero. In addition the following relation holds

$$\begin{aligned} \chi_{iiii}(-\omega; \omega_1, \omega_2, \omega_3) &= \chi_{iijj}(-\omega; \omega_1, \omega_2, \omega_3) + \\ &\chi_{ijji}(-\omega; \omega_1, \omega_2, \omega_3) + \chi_{ijij}(-\omega; \omega_1, \omega_2, \omega_3) \end{aligned} \quad (3.2)$$

The elements of χ for an atomic gas can be derived from the atomic susceptibility, χ^{atom} , by averaging over angular orientations of the atoms, applying local field correction factors, and averaging over atomic velocities (Doppler averaging). Cesium atoms are symmetric so the orientational averaging has no effect, and the fields at

Table 3.1

Definitions

$$E_{\omega} = \frac{1}{2} \left[E^{\omega} e^{-i(\omega t - kx)} + E^{-\omega} e^{i(\omega t - kx)} \right]$$

$$E^{\omega*} = E^{-\omega}$$

E_{ω} is an electric field

$$P_{\omega} = \frac{1}{2} \left[P^{\omega} e^{-i(\omega t - kx)} + P^{-\omega} e^{i(\omega t - kx)} \right]$$

$$P^{\omega*} = P^{-\omega}$$

P_{ω} is a polarization

$$P_i^{\omega_{\sigma}} = K \chi_{ijk\dots r}(-\omega_{\sigma}; \omega_1, \omega_2, \dots, \omega_m) E_j^{\omega_1} E_k^{\omega_2} \dots E_r^{\omega_m}$$

$$K = 2^n D$$

n = number of nonzero P^{ω} labels minus number of nonzero E^{ω} labels

D = number of distinguishable arrangements of field ω 's. ie., of $\omega_1 \dots \omega_m$

$ij\dots r$ refer to polarization directions \hat{x} , \hat{y} , and \hat{z}

Table 3.1 (cont.)

Complex numbers or functions are written as: $x = x' + ix''$ where x' and x'' are real.

$Z(x, y)$ is the plasma dispersion function

$$Z(x, y) \equiv \frac{1}{\sqrt{\pi}} \int_{-\infty}^{\infty} \{e^{-t^2} / (t - x - iy)\} dt$$

$$\Omega_{nl} \equiv \omega_{nl} - i \frac{\Gamma_{nl}}{2}$$

ω_{nl} is the frequency of the transition from state n to state l and Γ_{nl} is the FWHM for that transition. If state l is the ground state, Ω_{nl} is written Ω_n .

P_{ω} = power of radiation at ω

$$\tilde{\omega} \equiv \frac{\omega}{2\pi c} \quad \tilde{\Omega} = \frac{\Omega}{2\pi c}$$

$$\Delta\tilde{\omega}_{nl} = \tilde{\omega}_{nl} \{2kT/Mc^2\}^{1/2} = \frac{\text{Doppler width}}{2\sqrt{\ln 2}}$$

the atomic sites are just the applied fields if the gas is dilute as it is in our case. Therefore, χ_{ijkl} is simply $N \cdot \langle \chi_{ijkl} \rangle_{\text{Doppler}}$ where N is the number of atoms per unit volume.

The susceptibilities which appear in the remainder of this text are $\chi_{zzzz}^{\text{atom}}$ unless indicated otherwise so the superscript and subscripts will be omitted for brevity. Doppler averaging will be indicated by $\langle \chi \rangle$.

3.1 Two Photon Absorption (TPA)

In this section an expression relating the nonlinear susceptibility χ to a two-photon-absorption cross section is derived by analogy with the one photon absorption case. The numerical value of the cross section is given, Doppler averaging is performed, and the hyperfine splitting of the ground state is discussed.

Just as linear, or single photon, absorption is produced by the imaginary part of the linear refractive index, two photon absorption is caused by an imaginary part of the nonlinear refractive index. Specifically, it will be shown below that two photon absorption depends on $\chi''(-\omega; \omega, \omega, -\omega)$ while single photon absorption depends on $\chi''(-\omega; \omega)$ where χ'' is the imaginary part of χ (see table 3.1).

If all contributions to the polarization at frequency ω , created by a single, linearly polarized applied

field of frequency ω are considered, the polarization in an isotropic medium may be written as

$$\begin{aligned} P^\omega = & NK_1\chi_1(-\omega;\omega) E^\omega + NK_3\chi_3(-\omega;\omega,\omega,-\omega) E^\omega E^\omega E^{-\omega} \\ & + NK_5\chi_5(-\omega;\omega,\omega,-\omega,-\omega,\omega) E^\omega E^{-\omega} E^{-\omega} E^\omega E^\omega + \dots \end{aligned} \quad (3.3)$$

Keeping only the first two terms we have

$$P^\omega = N\{K_1\chi_1(-\omega;\omega) + K_3\chi_3(-\omega;\omega,\omega,-\omega) E^\omega E^{-\omega}\} E^\omega \quad (3.4)$$

The first term accounts for the linear index of refraction and single photon absorption. It is useful to consider the second term an intensity dependent extension of the first. This will produce an intensity dependent refractive index and an intensity dependent absorption cross section. The term inside the brackets is now to be treated as the effective susceptibility. Substituting it in the usual definitions of the dielectric constant (ϵ) and the refractive index (n), we have

$$\epsilon = 1 + 4\pi N \{K_1\chi_1 + K_3\chi_3 E^\omega E^{-\omega}\} \quad (3.5)$$

$$n = \sqrt{\epsilon} \approx 1 + 2\pi N \{K_1\chi_1 + K_3\chi_3 E^\omega E^{-\omega}\} \quad (3.6)$$

In this last step it was assumed $(\epsilon-1) \ll 1$. It is now possible to find the absorption cross section.

$$\sigma = \frac{8\pi^2}{\lambda} \text{Im}\{K_1 \chi_1 + K_3 \chi_3 E^\omega E^{-\omega}\} = \sigma_1 + \sigma_2 \quad (3.7)$$

$$\sigma_1 = \frac{8\pi^2}{\lambda} K_1 \chi_1'' \quad \sigma_2 = \frac{8\pi^2}{\lambda} K_3 \chi_3'' E^\omega E^{-\omega} \quad (3.8)$$

The cross section σ_1 , which produces linear absorption, is independent of intensity and proportional to $\chi_1''(-\omega; \omega)$. The cross section σ_2 , on the other hand, depends on $\chi_3''(-\omega; \omega, \omega, -\omega)$ and on the laser intensity, so the probability that an atom will absorb a photon due to σ_2 is proportional to the intensity squared, as is expected for TPA.

In order to find the value of σ_2 , χ_3'' must be evaluated for a cesium atom in the ground state ($6S_{1/2}$). Keeping only the term which is nearly two photon resonant, we find that when all fields are polarized in the z direction²

$$\chi_3(-\omega; \omega, \omega, -\omega) = (-\hbar)^{-3} 2R_{1,2,3} e^4. \quad (3.9)$$

$$\sum_{nl} \frac{\langle 6S_{1/2} | z | lP \rangle \langle lP | z | 9D_{3/2} \rangle \langle 9D_{3/2} | z | nP \rangle \langle nP | z | 6S_{1/2} \rangle}{(\Omega_{lP}^* - \omega) (\Omega_{nP} - \omega) (\Omega_9 - 2\omega)}$$

where $R_{1,2,3}$ denotes the average obtained by permuting the E fields and Ω_9 is $\Omega_{9D_{3/2}-6S_{1/2}}$. Since $\Omega_{LP} \approx \Omega_{LP}^*$ this simplifies to

$$\chi_3 = e^4 (-\hbar)^{-3} \frac{4}{6} (\Omega_{nP} - 2\omega)^{-1} . \quad (3.10)$$

$$\sum_n \left| \frac{\langle 9D_{3/2} | z | nP \rangle \langle nP | z | 6S_{1/2} \rangle}{(\Omega_{nP} - \omega)} \right|^2$$

This has been evaluated by Orr⁸ as

$$\chi_3 \approx 2.25 \times 10^{-31} (\tilde{\Omega}_9 - 2\tilde{\omega})^{-1} \text{ esu} \quad (3.11)$$

where the units of $\tilde{\Omega}$ and $\tilde{\omega}$ are cm^{-1} . This is the value of χ_3 for a single atom of cesium in the $6S_{1/2}$ state. For comparison with experiments, Doppler averaging must be performed. This yields

$$\langle \chi_3 \rangle = 2.25 \times 10^{-31} \frac{Z(x,y)}{\Delta\tilde{\omega}_9} \quad (3.12)$$

where $Z(x,y)$ is the plasma dispersion function,⁹ $\Delta\tilde{\omega}_9$ is the Doppler width in cm^{-1} divided by $2\sqrt{\ln 2}$, and

$$x = \frac{2\tilde{\omega} - \tilde{\Omega}'_9}{\Delta\tilde{\omega}_9} ; y = \frac{-\tilde{\Omega}''_9}{\Delta\tilde{\omega}_9} ; \Delta\tilde{\omega}_9 = \tilde{\Omega}'_9 \{2kT/Mc^2\}^{1/2} \quad (3.13)$$

Taking the imaginary part of $\langle \chi_3 \rangle$ and using $\Delta\tilde{\omega}_9 = .025 \text{ cm}^{-1}$ gives

$$\langle \chi_3'' \rangle = 9.3 \times 10^{-30} Z''(x, y) \quad (3.14)$$

Finally, using equations 3.8 and 3.16, we find

$$\sigma_2 = 6.7 \times 10^{-26} I Z''(x, y) \quad (3.15)$$

where I is in watts/cm^2 and σ is in cm^2 . It should be mentioned that the maximum value of Z'' is approximately $\sqrt{\pi}$ and occurs when the laser is tuned to half the $6S_{1/2} - 9D_{3/2}$ transition frequency ($x = 0$). The resonance shape of σ_2 is shown in fig. 3.1 where Z'' is plotted as a function of x for $y = .1$. Note that according to its definition in eqn. 3.13, y is approximately the ratio of the homogeneous width to the Doppler width.

The expression for σ_2 is modified if the hyperfine splitting of the ground state ($6S_{1/2}$) is included. The state is split into two hyperfine components with a separation of $.31 \text{ cm}^{-1}$ and the statistical weights 7/16 and 9/16 so eqn. 3.15 becomes

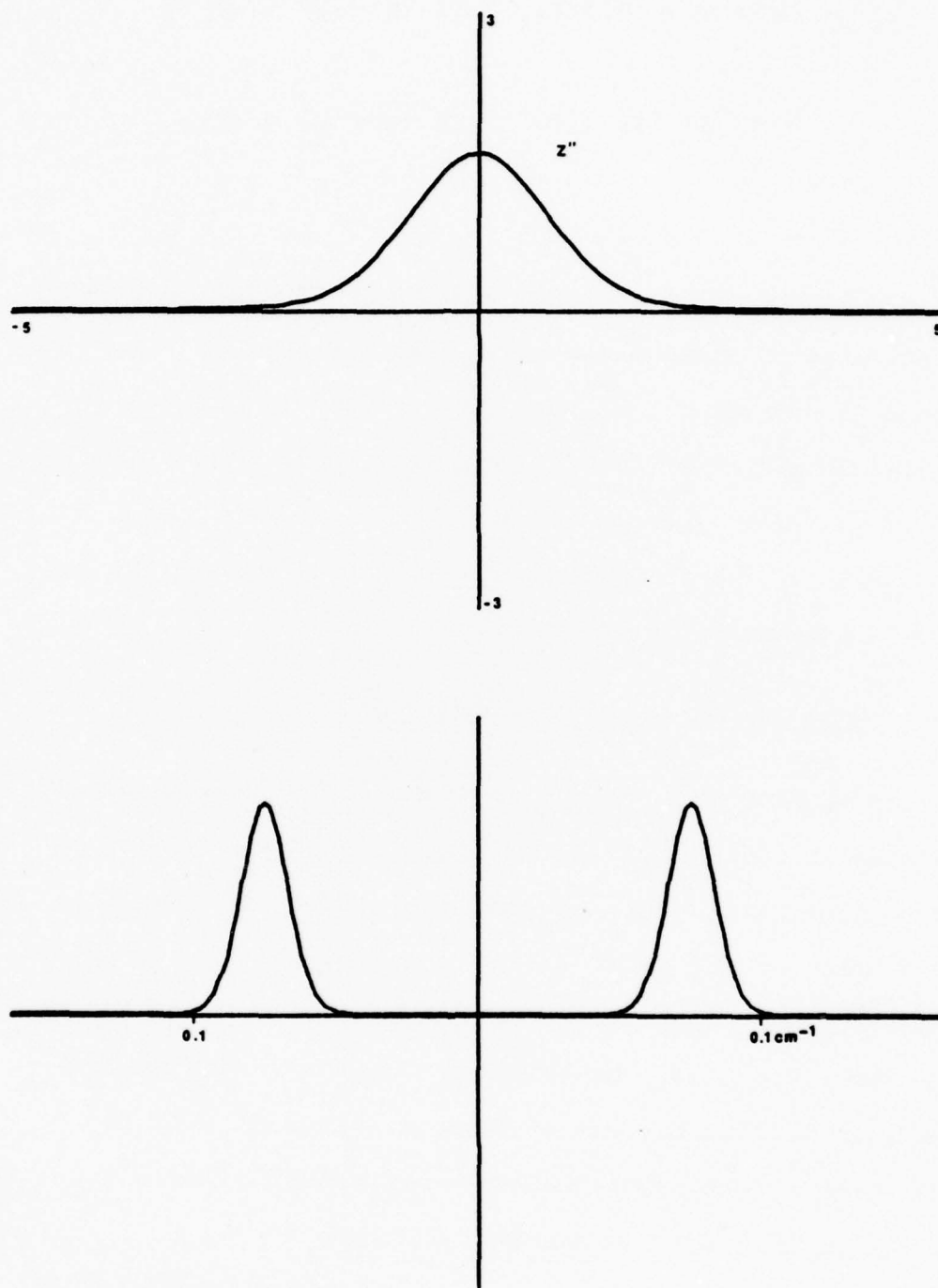


Fig. 3.1

Top: $Z''(x,.1)$

Bottom: hyperfine split TPA cross section

$$\sigma_2 = (7/16) 6.7 \times 10^{-26} \text{ IZ}'' \left\{ x - \frac{9}{16} h, y \right\} + \quad (3.16)$$

$$(9/16) 6.7 \times 10^{-26} \text{ IZ}'' \left\{ x + \frac{7}{16} h, y \right\}$$

where $h = \frac{.31}{\Delta\tilde{\omega}_9}$.

In summary, the rate at which cesium atoms are promoted from the ground state to the $9D_{3/2}$ level is proportional to the square of the laser intensity and exhibits a resonant behavior described by eqn. 3.16 where x is the normalized detuning of the laser from the two photon resonance between the states $6S_{1/2}$ and $9D_{3/2}$, and y (see eqn. 3.13) is much less than unity.

3.2 Third Harmonic Generation (THG)

This section presents some aspects of the theory of two-photon-resonant third harmonic generation in cesium vapor. In particular, we will derive the $\sin^2(\pi N_{CL}/2)$ dependence of the third harmonic signal which we used in chapter 2 to calibrate the amount of cesium vapor in the cell (see fig. 2.2); we will discuss the resonance line shape, including Doppler averaging, since it will be important in the next chapter. The presentation of theory in this section follows that of Leung.⁴

Dispersion in the cesium gas causes the $\sin^2(\pi N_{CL}/2)$ dependence of the third harmonic signal. Here N_{CL} , the number of coherence lengths of Cs, is proportional to

the product of the integral of the cesium density along the length of the cell and Δk_0 , which is a measure of the dispersion. In order to derive this result we consider first a sample of uniform density N and length L in which we wish to generate third harmonic. The third harmonic polarization is locked in space and time to the applied field E^ω so it has the wave vector $3\vec{k}_\omega$, where \vec{k}_ω is the wave vector for E^ω in the sample. The third harmonic radiation, in contrast, has the wave vector $\vec{k}_{3\omega}$ in the sample. Since all the k vectors point in the x direction, we drop the vector notation and define Δk as $3k_\omega - k_{3\omega}$. A nonzero value of Δk means that the phase velocities of laser radiation and its harmonic are different in which case the third harmonic radiation generated at one point in the sample will be out of phase with that produced at a point farther along. This interference in the harmonic waves causes the \sin^2 dependence of THG. This result is derived below by solving the driven wave equation.

The third harmonic polarization $P^{3\omega}$ is given by

$$P^{3\omega}(x) = \frac{1}{4}(E^\omega)^3 N \chi(-3\omega; \omega, \omega, \omega) e^{i3k_\omega x} \quad (3.17)$$

The wave equation for the third harmonic is

$$\nabla \times \nabla \times E^{3\omega}(x) - k_{3\omega}^2 E^{3\omega}(x) = 4\pi(3\omega/c)^2 P^{3\omega}(x) \quad (3.18)$$

where the polarization $P^{3\omega}(x)$ acts as the driving term.

If a solution of the form $E^{3\omega}(x) = A(x)e^{ik_{3\omega}x}$ is assumed, then substitution into eqn. 3.18 gives

$$-2 \frac{\partial A(x)}{\partial x} (ik_{3\omega}) e^{ik_{3\omega}x} = \pi N (3\omega/c)^2 (E^\omega)^3 \langle \chi \rangle e^{i3k_\omega x} \quad (3.19)$$

where $\frac{\partial^2 A(x)}{\partial x^2}$ has been neglected because it is assumed to be small compared with $2k_3 \frac{\partial A(x)}{\partial x}$.

This simplifies to

$$\frac{\partial A(x)}{\partial x} = \pi N (3\omega/c)^2 \frac{(E^\omega)^3}{ik_{3\omega}} \langle \chi \rangle e^{i\Delta k_0 N x} \quad (3.20)$$

where $\Delta k_0 = \frac{\Delta k}{N}$.

Now assuming $A(0) = 0$ and integrating from $x = 0$ to $x = L$ yields

$$A(L) = C (E^\omega)^3 \frac{(e^{i\Delta k_0 N L} - 1)}{\Delta k_0 N} \langle \chi \rangle N \quad (3.21)$$

The power at third harmonic is proportional to $|A(L)|^2$ since A is a field strength, so

$$P_{3\omega} \propto \sin^2(\Delta k_0 NL/2) \{|E^\omega|^2\}^3 \left| \frac{\langle \chi \rangle}{\Delta k_0} \right|^2 \quad (3.22)$$

This is the \sin^2 dependence mentioned earlier.

The density of cesium was assumed uniform in deriving eqn. 3.22. This is not a good approximation to the experimental case but eqn. 3.22 is easily extended to the case of nonuniform density by replacing the argument of the sine by $\frac{\Delta k_0}{2} \int_0^L N(x) dx$ where $N(x)$ is the cesium number density. The sinusoidal behavior makes the measurement of $\int_0^L N(x) dx$ a simple matter as explained in chapter 2.

Equation 3.22 also shows that the intensity of third harmonic radiation produced by an applied field of strength E^ω is proportional to $\{|E|^\omega\}^3$ or the cube of the intensity of the applied radiation.

The resonant behavior for THG depends on the term $|\langle \chi \rangle|^2$ of eqn. 3.22. This χ has the same resonance denominator as that of TPA; namely, $(\Omega_g - 2\omega)$. Consequently, the Doppler average yields

$$\langle \chi(-3\omega; \omega, \omega, \omega) \rangle \propto Z'(x, y) + i Z''(x, y) \quad (3.23)$$

where x and y are defined in eqn. 3.14. Since the signal at third harmonic is proportional to $|\langle \chi \rangle|^2$, the resonance shape is given by

$$P_{3\omega} \propto |\langle \chi \rangle|^2 \propto Z'^2 + Z''^2 \quad (3.24)$$

It is interesting to note that both the real and imaginary parts of χ contribute to the generation of third harmonic. The harmonic generated by the imaginary part of χ is 90° out of phase with that produced by the real part so they add as $\chi'^2 + \chi''^2$ or $Z'^2 + Z''^2$. Far from the resonance THG is due solely to Z' while at the line center only Z'' contributes. The total lineshape $Z'^2 + Z''^2$ has the resonance shape shown in fig. 3.2 with the resonance peak at $2\omega = \Omega'_g$ or $x = 0$.

If the hyperfine splitting of the ground state is to be included, the Doppler averaged χ will have the form

$$\langle \chi(-3\omega; \omega, \omega, \omega) \rangle \propto \quad (3.25)$$

$$(7/16)Z\{x - \frac{9}{16}h, y\} + (9/16)Z\{x + \frac{7}{16}h, y\}$$

where $h \equiv \frac{.31}{\Delta\omega}$. Since $\mathbb{P}_{3\omega}$ is proportional to $|\chi|^2$ it must have the form

$$\mathbb{P}_{3\omega} \propto \quad (3.26)$$

$$\begin{aligned} & \left[(7/16)Z'\{x - \frac{9}{16}x, y\} + (9/16)Z'\{x + \frac{7}{16}h, y\} \right]^2 + \\ & \left[(7/16)Z''\{x - \frac{9}{16}x, y\} + (9/16)Z''\{x + \frac{7}{16}h, y\} \right]^2 \end{aligned}$$

This is graphed in fig. 3.2.

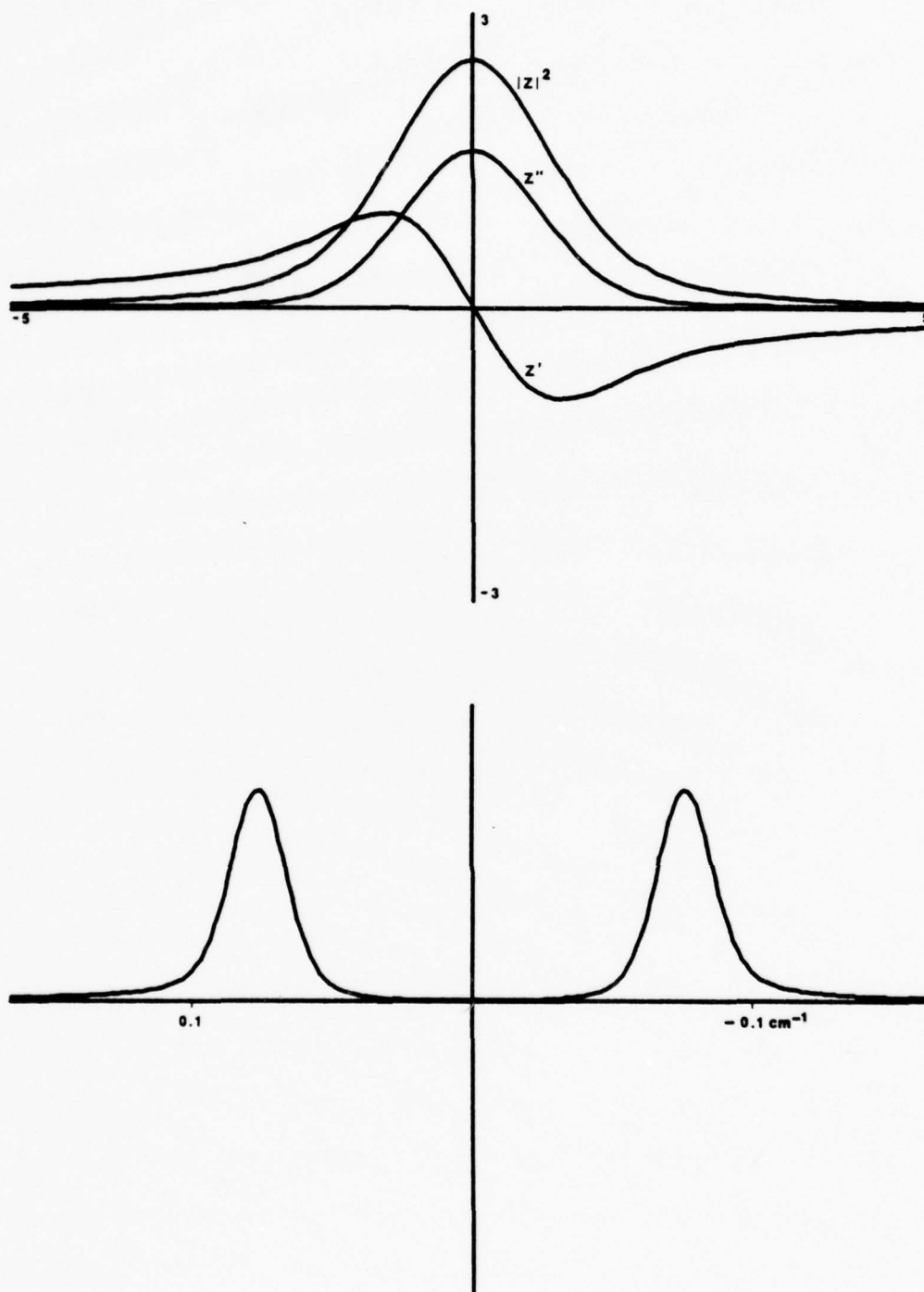


Fig. 3.2

Top: Frequency dependence of $Z'(x,.1)$, $Z''(x,.1)$, $|Z(x,.1)|^2$
 Bottom: hyperfine split THG efficiency

When the laser is tuned between the two resonances the Z' terms have opposite signs whereas they have the same sign if the laser is higher or lower than both. This interference produces asymmetry in the two resonance peaks which moves their centers of weight apart somewhat. The Z'' terms are narrow in relation to their separation, and their interference does not significantly affect the lineshape.

To summarize, the characteristics of the third harmonic process, as predicted by the theory discussed above, are: linear dispersion produces a \sin^2 dependence on the total amount of cesium traversed; the signal varies as the cube of the laser power if the number of coherence lengths of cesium and laser tuning are constant; the resonance shape is the Doppler broadened resonance line shape as shown in fig. 3.2.

3.3 Parametric Gain

In this section we present the theory for the resonantly enhanced parametric process. The section is divided into several subsections, the first of which contains a brief derivation of the equations describing parametric gains. The resonant behavior of gain is deduced from these equations in the second subsection; and, in succeeding subsections, the existence of a threshold power and numerical estimates of gains and threshold powers are discussed.

3.3a The Gain Equations

The parametric process may be considered to be two separate three-wave-mixing processes which produce respectively the signal and idler polarizations. The first of these mixes the pump (laser) wave with itself and with the idler wave via $\chi(-\omega_S; \omega_P, \omega_P, -\omega_I)$. The second mixes the signal and pump waves via $\chi(-\omega_I; \omega_P, \omega_P, -\omega_S)$. The polarizations at the signal and idler frequencies are in turn the source of radiations which, depending on their phases relative to the signal and idler waves, can produce gain or loss in the signal and idler.

The derivation of the gain equations presented in this subsection follows that of Yariv and Pearson.¹⁰ The application to the particular case of the ruby laser-cesium vapor has been developed by Leung.⁴ The derivation is displayed here in order that approximations may be pointed out and to facilitate the discussion of resonance lineshapes in a later subsection.

From the description of the parametric process, it is apparent that in order to find the intensity of the idler and signal fields, we must solve a pair of coupled wave equations in which the polarizations at the signal and idler frequencies act as the source or driving terms. The polarizations are given by

$$\begin{aligned}
P^S(x) &= NK_S \langle \chi_S \rangle E^P E^P E^{-I} e^{i(k_P + k_P - k_I^*)x} \\
P^I(x) &= NK_I \langle \chi_I \rangle E^P E^P E^{-S} e^{i(k_P + k_P - k_S^*)x}
\end{aligned}
\tag{3.27}$$

where $\chi_S \equiv \chi(-\omega_S; \omega_P, \omega_P, -\omega_I)$ and $\chi_I \equiv \chi(-\omega_I; \omega_P, \omega_P, -\omega_S)$.

Note that k is not confined to real values so linear absorption can be included.

The coupled wave equations which are to be solved are

$$\begin{aligned}
\nabla^2 (E^S e^{-i(\omega_S t - k_S x)}) &= \frac{1}{c^2} \frac{\partial^2}{\partial t^2} \{ E^S e^{-i(\omega_S t - k_S x)} + \\
&\quad 4\pi NK_S \langle \chi_S \rangle E^P E^P E^{-I} e^{-i(\omega_S t - 2k_P x + k_I^* x)} \}
\end{aligned}$$

and (3.28)

$$\begin{aligned}
\nabla^2 (E^{-I} e^{i(\omega_I t - k_I^* x)}) &= \frac{1}{c^2} \frac{\partial^2}{\partial t^2} \{ E^{-I} e^{i(\omega_I t - k_I^* x)} + \\
&\quad 4\pi NK_I \langle \chi_I^* \rangle E^{-P} E^{-P} E^S e^{i(\omega_I t - 2k_P x + k_S x)} \}
\end{aligned}$$

We have assumed, in writing this pair of equations that k_P is real and also that there is little loss from the pump wave due to conversion of its energy into signal and idler waves.

If the field strengths E^I and E^S are assumed to change by a very small percentage per wavelength, then the

terms involving $\frac{\partial^2}{\partial x^2}$ are much smaller than those involving $\frac{\partial}{\partial x}$ and may be neglected. We are then left with the following pair of coupled first order differential equations.

$$\frac{\partial E^S}{\partial x} = \frac{i2\pi\omega_S^2}{k_S c^2} \langle \chi_S \rangle N(3/4) E^P E^P E^{-I} e^{i\Delta k x} \quad (3.29)$$

$$\frac{\partial E^{-I}}{\partial x} = \frac{-i2\pi\omega_I^2}{k_I^* c^2} \langle \chi_I^* \rangle N(3/4) E^{-P} E^{-P} E^S e^{-i\Delta k x}$$

where $\Delta k = 2k_P - k_S - k_I^*$.

Equation 3.29 may be solved by conventional methods to yield the following solutions for E^S and E^I .

$$\begin{aligned} E^S &= \{E_O^S (\cosh \gamma x - \frac{i\Delta k}{2\gamma} \sinh \gamma x) + \frac{iA}{\gamma} E_O^{-I} \sinh \gamma x\} e^{\frac{1}{2}i\Delta k x} \\ E^{-I} &= \{E_O^{-I} (\cosh \gamma x + \frac{i\Delta k}{2\gamma} \sinh \gamma x) - \frac{iB}{\gamma} E_O^S \sinh \gamma x\} e^{-\frac{1}{2}i\Delta k x} \end{aligned} \quad (3.30)$$

where

$$\begin{aligned} A &= \frac{2\pi}{c^2} \frac{3}{4} \frac{\omega_S^2}{k_S} N \langle \chi_S \rangle E^P E^P \\ B &= \frac{2\pi}{c^2} \frac{3}{4} \frac{\omega_I^2}{k_I^*} N \langle \chi_I^* \rangle E^{-P} E^{-P} \end{aligned} \quad (3.31)$$

$$G = AB \quad \gamma = \{G - (\Delta k/2)^2\}^{\frac{1}{2}}$$

These are the basic equations describing the parametric process. To arrive at this result we have assumed there is little loss of the pump intensity due to either linear absorption or conversion to signal and idler waves although linear absorption of signal and idler radiation is allowed. We have also assumed that the gain per wavelength is small and have included Doppler averaging in eqn. 3.27 as we must, rather than in eqn. 3.30 where the product $\chi_S \chi_I^*$ would appear.

3.3b Resonant Shape of Parametric Gain

This subsection is devoted to a discussion of the resonant behavior of parametric gain. Since this is a complex matter, we shall consider first the nature of the product $\langle \chi_S \rangle \langle \chi_I^* \rangle$ which occurs in γ (eqn. 3.31), then the behavior of Δk will be discussed, and finally, the resonance shape of the gain itself is considered.

In the case of cesium atoms interacting with ruby laser radiation, the value of each χ is maximized when the laser is tuned to the two-photon resonance and the signal is resonant with the $6S_{\frac{1}{2}} - nP$ transition, where the nP state is any P state with energy less than that of $9D_{\frac{3}{2}}$. This is evident from the following expressions for $\langle \chi_S \rangle$ and $\langle \chi_I \rangle$.

$$\begin{aligned} \langle \chi_S \rangle &= \frac{e^4}{3(hc)^3} \langle 6S_{\frac{1}{2}} | z | nP \rangle \langle nP | z | 9D_{\frac{3}{2}} \rangle \cdot \\ &\sum_m \frac{\langle 9D_{\frac{3}{2}} | z | mP \rangle \langle mP | z | 6S_{\frac{1}{2}} \rangle}{\tilde{\Omega}_{mP} - \tilde{\omega}_P} \end{aligned} \quad (3.32)$$

$$\langle (\tilde{\Omega}_9 - 2\tilde{\omega}_9)^{-1} (\tilde{\Omega}_{nP} - \tilde{\omega}_S)^{-1} \rangle$$

where nP is the state near resonance with the signal frequency. Tuning the laser to resonance maximizes $\{\tilde{\Omega}_9 - 2\tilde{\omega}_9\}^{-1}$ while the factor $\{\tilde{\Omega}_{nP} - \tilde{\omega}_S\}^{-1}$ is maximum if the signal is near the $6S_{\frac{1}{2}} - nP$ resonance. The same is true for $\langle \chi_I^* \rangle$ since

$$\begin{aligned} \langle \chi_I^* \rangle &= \frac{e^4}{3(hc)^3} \langle 6S_{\frac{1}{2}} | z | nP \rangle^* \langle nP | z | 9D_{\frac{3}{2}} \rangle^* \cdot \\ &\sum_m \frac{\langle 9D_{\frac{3}{2}} | z | mP \rangle \langle mP | z | 6S_{\frac{1}{2}} \rangle}{\tilde{\Omega}_{mP} - \tilde{\omega}_P} \end{aligned} \quad (3.33)$$

$$\langle (\tilde{\Omega}_9^* - 2\tilde{\omega}_P)^{-1} (\tilde{\Omega}_{nP} - \tilde{\omega}_S)^{-1} \rangle$$

Performing the Doppler averaging indicated in eqn. 3.30 and 3.31 yields

$$\begin{aligned} \langle (\tilde{\Omega}_9 - 2\tilde{\omega}_P)^{-1} (\tilde{\Omega}_{nP} - \tilde{\omega}_S)^{-1} \rangle &= \\ \frac{1}{\Delta\tilde{\omega}_{nP} \cdot \Delta\tilde{\omega}_9} \cdot \frac{Z(\zeta_{nP}) - Z(\zeta_9)}{\zeta_{nP} - \zeta_9} \end{aligned} \quad (3.34)$$

and

$$\begin{aligned} <(\tilde{\Omega}_9 - 2\tilde{\omega}_P)^{-1} (\tilde{\Omega}_{nP} - \tilde{\omega}_S)^{-1}> = \\ & \frac{1}{\Delta\tilde{\omega}_{nP} \cdot \Delta\tilde{\omega}_9} \cdot \frac{Z(\zeta_{nP}) - Z^*(\zeta_9)}{\zeta_{nP} - \zeta_9^*} \end{aligned} \quad (3.35)$$

where

$$\begin{aligned} \zeta_9 &= (x_9 + iy_9) ; x_9 = \frac{2\tilde{\omega}_P - \tilde{\Omega}'_9}{\Delta\tilde{\omega}_9} ; y_9 = \frac{-\tilde{\Omega}''_9}{\Delta\tilde{\omega}_9} \\ \zeta_{nP} &= (x_{nP} + iy_{nP}) ; x_{nP} = \frac{\tilde{\omega}_S - \tilde{\Omega}'_{nP}}{\Delta\tilde{\omega}_{nP}} ; y_{nP} = \frac{-\tilde{\Omega}''_{nP}}{\Delta\tilde{\omega}_{nP}} \end{aligned} \quad (3.36)$$

and $Z(\zeta)$ is the Plasma Dispersion Function.⁹

Combining these results of Doppler averaging and eqns. 3.30 and 3.31 we arrive at the following expression for $<\chi_S><\chi_I^*>$.

$$<\chi_S> <\chi_I^*> = 5.06 \times 10^{18} (\Delta\tilde{\omega}_{nP} \cdot \Delta\tilde{\omega}_9)^{-2} .$$

$$|<6S_{\frac{1}{2}}|z|nP><nP|z|9D_{\frac{3}{2}}>|^2 \cdot \left| \sum_m \frac{<9D_{\frac{3}{2}}|z|mP><mP|z|6S_{\frac{1}{2}}>}{\tilde{\Omega}_{mP} - \tilde{\omega}_P} \right|^2 .$$

$$\frac{Z(\zeta_{nP}) - Z(\zeta_9)}{\zeta_{nP} - \zeta_9} \cdot \frac{Z(\zeta_{nP}) - Z^*(\zeta_9)}{\zeta_{nP} - \zeta_9^*} \quad (3.37)$$

The resonance shape of $\langle \chi_S \rangle$ $\langle \chi_I^* \rangle$ is just that of the last two terms of eqn. 3.37. Graphs of the real and imaginary parts of each term as a function of x_{np} are shown in figures 3.3 and 3.5 for the laser tuned to resonance ($x_g=0$) and in figures 3.4 and 3.6 for the laser detuned slightly ($x_g=1$). Values of .1 and .05 were chosen for y_{np} and y_g respectively to facilitate demonstrating features of the functions. In reality, somewhat smaller values should be used so the natural linewidth features in figures 3.3 and 3.4 should be narrower and greater in amplitude, but the use of .1 and .05 will not affect the conclusions we shall reach concerning the maximum value of gain itself.

Figure 3.5 shows the real and imaginary parts of the resonance lineshapes of $\langle \chi_S \rangle$ when $x_g = 0$. They have maximum values of about two and widths of a Doppler width. The lineshape shown in fig. 3.6 ($x_g=1$) is somewhat different but the widths and amplitudes are about the same. The values chosen for the y 's makes little difference in either figure as long as they are much less than 1.

The plots of $\langle \chi_I^* \rangle$, shown in figures 3.3 and 3.4, have the interesting feature of a tall spike with the homogeneous linewidth and a height which is sensitive to the values used for the y 's. In fact, it may be seen that for small values of y_{np} and y_g , the shape near $x_{np} = x_g$ is determined largely by the denominator

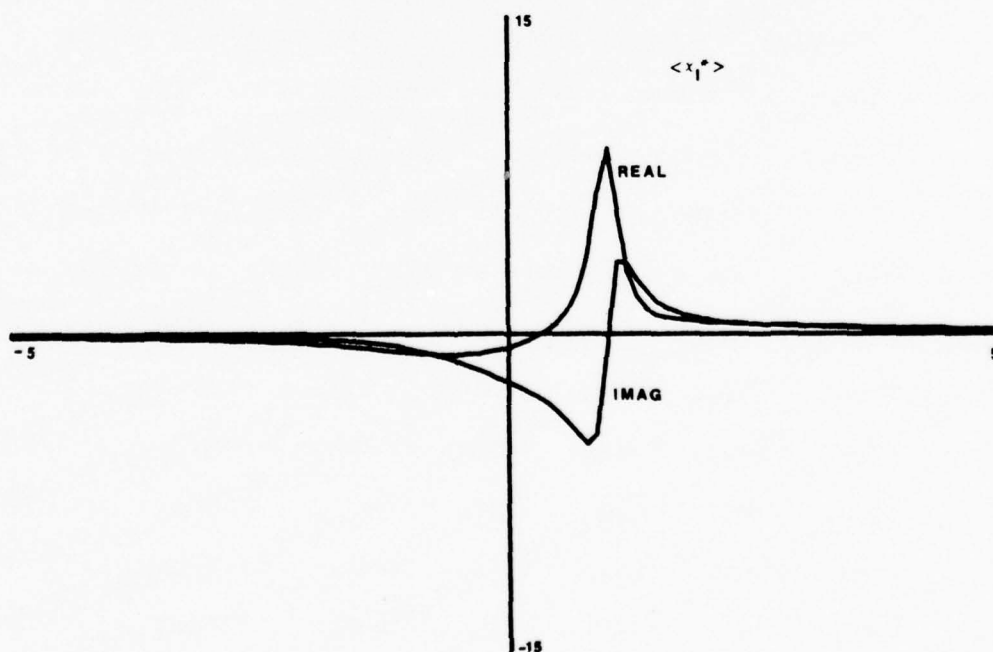
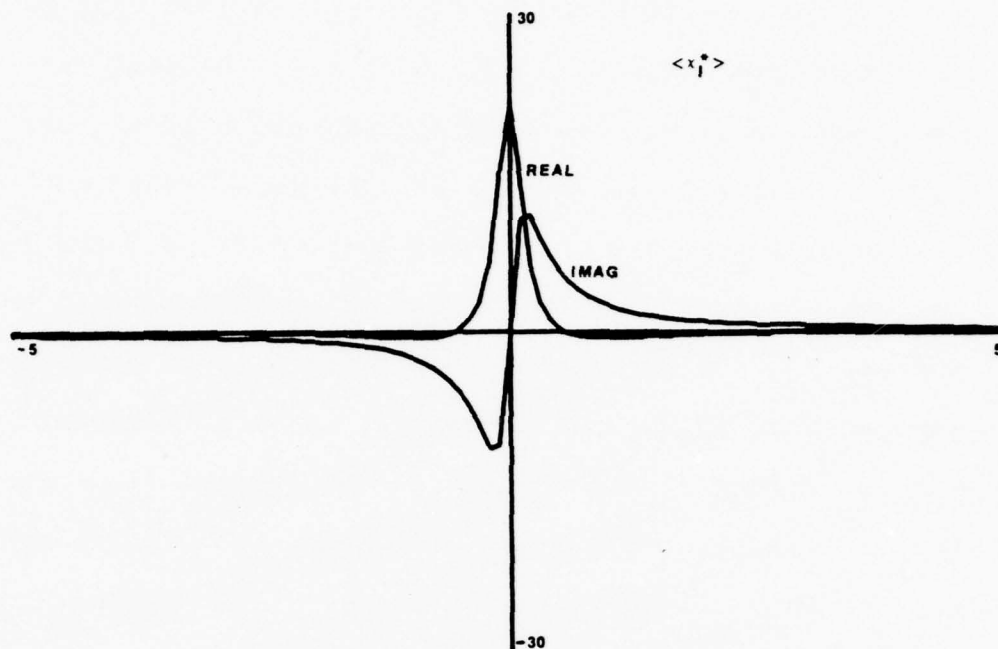


Fig. 3.3 (top): real and imag. parts of $\langle x_I^* \rangle$ for $x_9=0$
 Fig. 3.4 (bottom): same for $x_9=1$

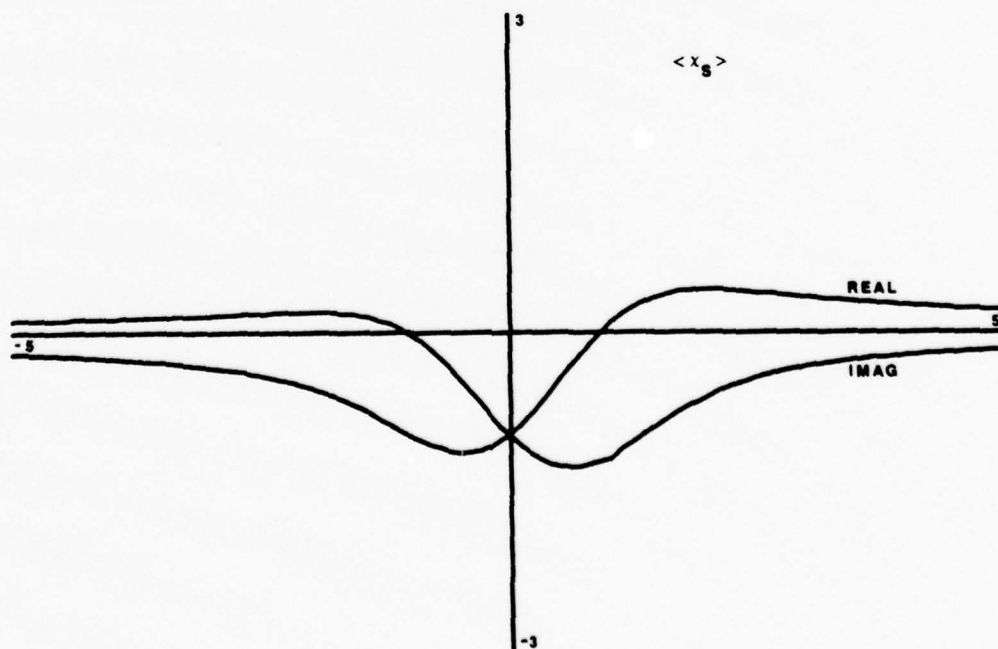
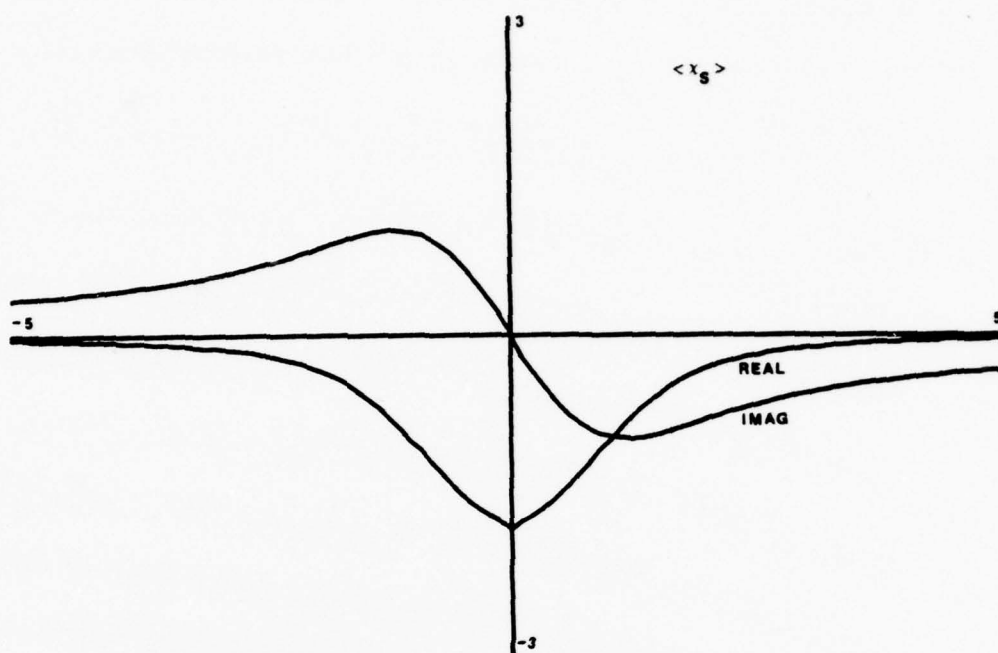


Fig. 3.5 (top): real and imag. parts of $\langle \chi_s \rangle$ for $x_9=0$
 Fig. 3.6 (bottom): same for $x_9=1$

$(x_{nP} - x_9) + i(y_{nP} + y_9)$ since the numerator is a slowly varying function of x_{nP} compared to the denominator.

Thus the width of the narrow peak is just

$$dx_{nP} = y_{nP} + y_9 \quad (3.38)$$

or substituting the definitions of x and y the width $d\omega_n$ is

$$d\omega_{nP} = \Omega_{nP}'' + \frac{\omega_{nP}}{\omega_9} \Omega_9'' \quad (3.39)$$

Furthermore, the maximum amplitude is $2\sqrt{\pi}/(y_{nP} + y_9)$ if x_9 is near zero, since the numerator is about $2i\sqrt{\pi}$ for x_9 and x_{nP} near zero. Notice also that when the laser is detuned by $\delta\omega_9$, the narrow peak occurs at a detuning $\delta\omega_{nP} = \delta\omega_9 (\omega_{nP}/\omega_9)$.

This line narrowing effect is reminiscent of the laser-induced line-narrowing effects discussed by Feld and Javan¹¹ and several other authors. In fact the Doppler averaging integrals which occur above are identical to those appearing in the Feld and Javan paper. The laser-induced line-narrowing occurs in a system of three energy levels when lasing is active between two of the levels. If the small signal gain from one of the lasing levels to a third level is measured, it is found that there are two dips or peaks with characteristic

homogeneous width superimposed on the much broader Doppler profile. One of the bumps is due to two successive single-photon transitions where one transition populates the common energy level with atoms of a selected axial velocity and the second transition involves only those atoms. The other bump is due to two-photon transitions. It does not involve velocity selective population of a level but arises from the nature of Doppler averaging. An intuitive understanding of the effect is difficult to achieve. The line narrowing in our case is of the two-photon type.

The resonance profile of the product $\langle \chi_S \rangle \langle \chi_I^* \rangle$ is plotted in fig. 3.7 for $x_9 = 0$ and fig. 3.8 for $x_9 = 1$. The narrow peak is still a prominent feature in both cases but the real parts are negative near $x_n = x_9$. As we shall see in a moment, the negative sign produces a dip in the gain profile rather than an enhancement so the values chosen for the y 's only changes the width of that dip and have little effect on the maximum gain as long as they are much less than one.

We consider next the resonant behavior of the other terms in the expression for gain. From equations 3.30 and 3.31, the gain coefficient at high pump powers is given by

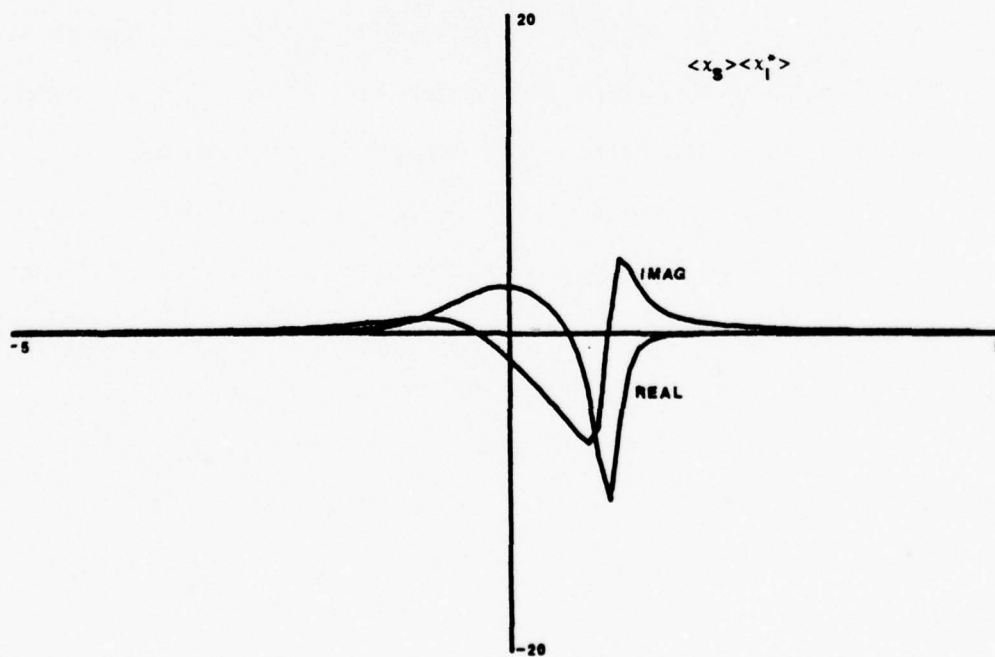
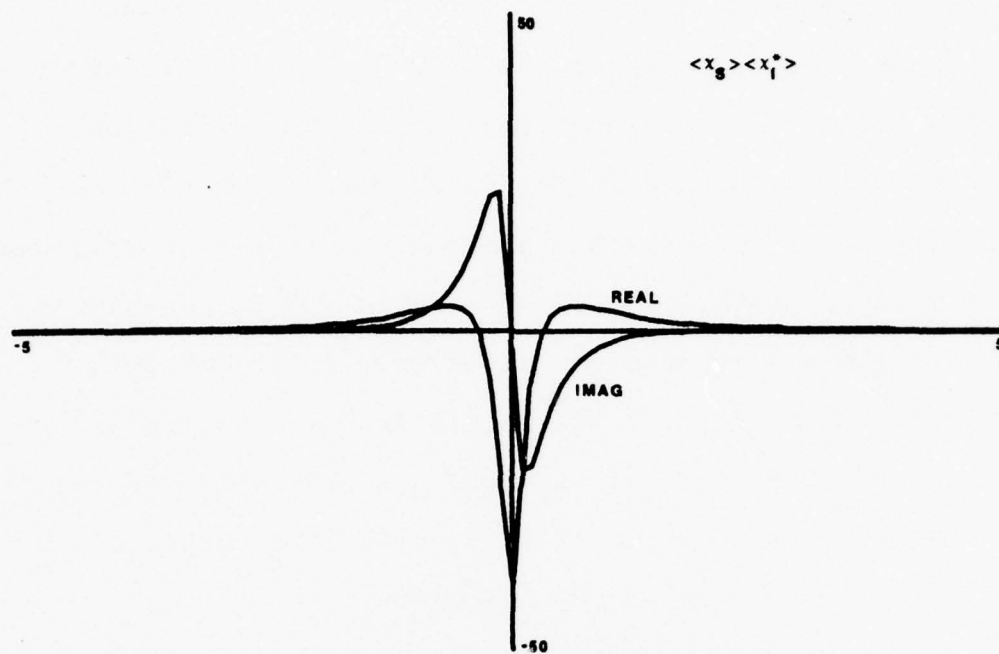


Fig. 3.7 (top): real and imag. parts of $\langle \chi_I^* \rangle \langle \chi_S \rangle$ for $x_9=0$
 Fig. 3.8 (bottom): same for $x_9=1$

$$\text{gain}_e \text{ (high pump power) } = \quad (3.40)$$

$$2\{G - (\Delta k/2)^2\}^{1/2} - \{k_S'' - k_I''\}$$

so we must next find the shapes of Δk and k_S'' and k_I'' . If we assume that all the atoms remain in the ground state, then k_P and k_I are real and constant over the range of interest, but k_S exhibits the usual Doppler broadened resonance behavior. The form of k_S is given by

$$k_S = \beta Z(x_{nP}, y_{nP}) \quad (3.41)$$

where β is a constant.

We can now discuss the resonance shape of the gain. Consider first the case of high pump power. Since G in eqn. 3.40 is proportional to P_ω^2 , the gain will be simply $2\sqrt{G}$ at sufficiently high pump powers and the shape will be that labeled $C = 0$ in figures 3.9 and 3.10. The dip at the line center in fig. 3.9, which was mentioned earlier, has a width of approximately a homogeneous width and occurs because G is negative and real at that point (see fig. 3.3 and eqn. 3.31).

As the laser or pump power is lowered, the other terms (Δk , k_S'' , k_I'') increase in relative importance and the gain profile assumes the shapes labeled $C = 1$ through $C = 4$ in figures 3.9 and 3.10 for successively lower

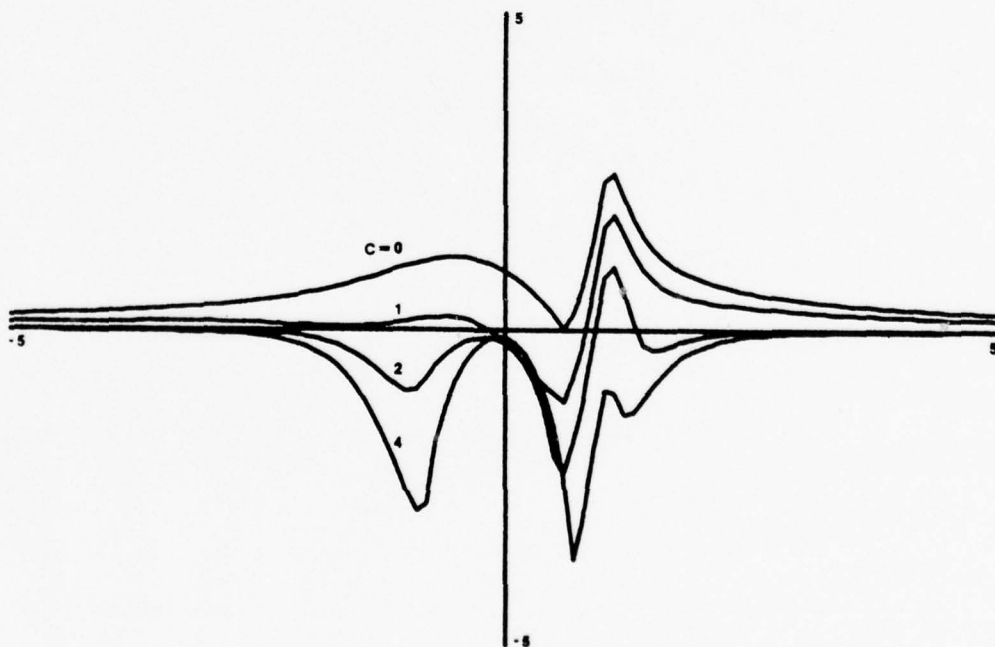
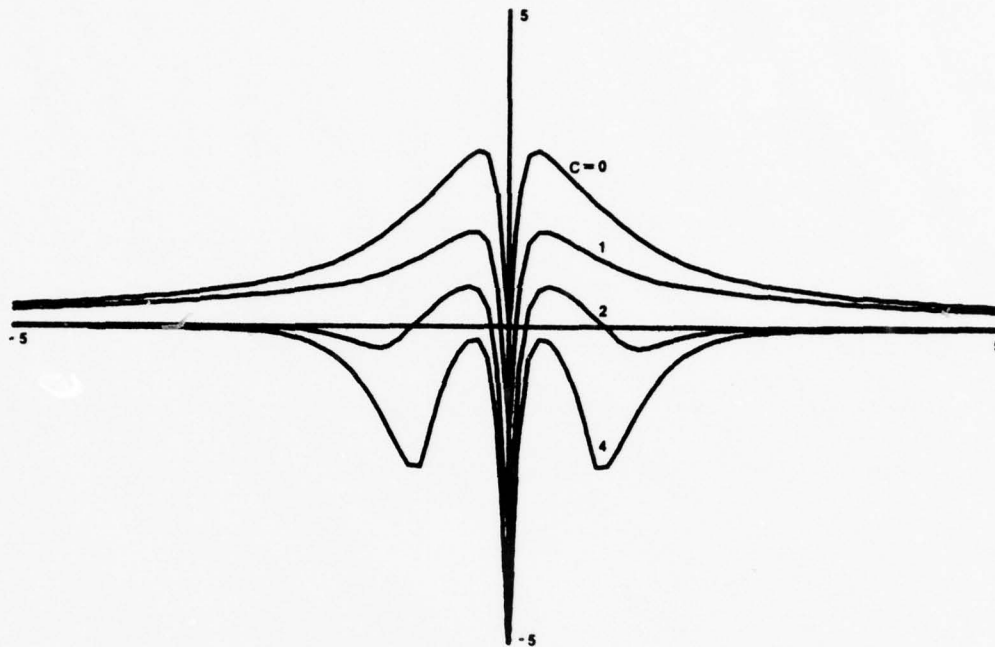


Fig. 3.9 (top): high power gain for $x_9=0$
Fig. 3.10 (bottom): same for $x_9=1$

pump powers. Note that positive values represent gain in these plots, and negative values represent loss.

3.3c Existence of Threshold Pump Power

If the pump power is lowered sufficiently, the gain curve is negative at all frequencies as it is, for instance, in the curve labeled $C = 4$ in fig. 3.9. This suggests that there is a threshold pump power below which gain does not appear. In fact, at low values of P_p , the expression for gain which we have used in generating fig. 3.9 (eqn. 3.40) is not valid since the Sinh terms of eqn. 3.28 become comparable with the Cosh terms. However, eqn. 3.28 reduces to equations describing simple linear loss at $P_\omega = 0$ so there must indeed be a threshold pump power. Furthermore, the threshold power must have a value such that $\sqrt{G} \sim \Delta k$.

3.3d Numerical Estimates of Parametric Gain

It is now possible to calculate the parametric gain coefficients for each of the five possible resonantly enhanced signal waves corresponding to the five intermediate P states. First, we calculate the gain for high pump powers where, according to eqn. 3.30, the gain coefficient is $2\sqrt{G}$. Using the definitions given by eqn. 3.31 we arrive at the following expression

$$\text{gain}_e \text{ (high pump power)} = 2.46 \times 10^{-15} \frac{\tilde{\omega}_S \tilde{\omega}_I}{n_S n_I^*} (\mathbb{P}_P/A)^2 N^2 \langle \chi_S \rangle \langle \chi_I^* \rangle \quad (3.42)$$

Using

$$\sum_m \frac{\langle 9D_{\frac{3}{2}} | z | mP \rangle \langle mP | z | 6S_{\frac{1}{2}} \rangle}{(\Omega_{mP} - \omega_S)} = 6.5 \times 10^{-21} \text{ esu} \quad (3.43)$$

in the expression for $\langle \chi_S \rangle \langle \chi_I^* \rangle$ we find

$$\langle \chi_S \rangle \langle \chi_I^* \rangle = \frac{1}{\tilde{\omega}_S^2 \tilde{\omega}_9} Q^2 F(\zeta_{nP}, \zeta_9) (3.70 \times 10^{-31}) \quad (3.44)$$

Putting this in eqn. 3.42 yields

$$\text{gain}_e \text{ (high pump power)} = \{ 2.74 \times 10^{-26} \frac{\omega_I}{\omega_S} Q^2 \frac{1}{n_S n_I^*} N^2 \mathbb{P}_P^2 F(\zeta_{nP}, \zeta_9) \}^{\frac{1}{2}} \quad (3.45)$$

where .03 has been used as the value for A, the beam area, and \mathbb{P}_P is in megawatts. The factor $F(\zeta_{nP}, \zeta_9)$ is the product of the last two terms of eqn. 3.37 (see plots in figures 3.7 and 3.8) and Q is defined by

$$Q^2 = | \langle 6S_{\frac{1}{2}} | z | nP \rangle \langle nP | z | 9D_{\frac{3}{2}} \rangle |^2 \quad (3.46)$$

The maximum value of $\text{Re} \{F(\zeta_{\text{NP}}, \zeta_9)\}^{\frac{1}{2}}$ is about 1.25 (see $C = 0$ curve of fig. 3.9) so

gain_e (high pump power) =

$$2.07 \times 10^{-13} \left[\frac{\omega_I}{\omega_S} Q^2 \right]^{\frac{1}{2}} N P_P \quad (3.47)$$

For the $10P_{\frac{1}{2}}$ line, $Q^2 \cdot (\omega_I/\omega_S)$ is 3.20×10^{-4} and the estimated value of Nz at one coherence length is 1.75×10^{16} (eqn. 2.1). Finally, expressing Nz in coherence lengths, (N_{CL}) equation 3.47 becomes

$$P_S = P_S^O \exp\{50.8 P_P N_{\text{CL}}\} \quad (3.48)$$

According to equation 3.47 the gains for the other lines can be found by evaluating the appropriate $\{Q^2 (\omega_I/\omega_S)\}^{\frac{1}{2}}$. These values are listed in table 3.2 and the gains relative to the $10P_{\frac{1}{2}}$ line are listed in table 3.3. Thus the equation describing the behavior of all the lines is

$$P_S = P_S^O \exp\{50.8 P_P N_{\text{CL}} R\} \quad (3.49)$$

where R is the relative gain from table 3.3.

Table 3.2

Line	$\omega_I (\text{cm}^{-1})$	$\omega_S (\text{cm}^{-1})$	Q	$\frac{\omega_I}{\omega_S} Q^2$
6P _{1/2}	17651	11178	.741	8.68×10^{-1}
7P _{1/2}	7063	21766	.0930	2.80×10^{-3}
8P _{1/2}	3120	25709	.0644	5.02×10^{-4}
9P _{1/2}	1192	27637	.0834	3.00×10^{-4}
10P _{1/2}	102	28727	-.300	3.20×10^{-4}
6P _{3/2}	17096	11732	.156	3.55×10^{-2}
7P _{3/2}	6882	21947	.0361	4.09×10^{-4}
8P _{3/2}	3037	25792	.0331	1.29×10^{-4}
9P _{3/2}	1147	27682	.0569	1.34×10^{-4}
10P _{3/2}	75	28754	-.198	1.02×10^{-4}

Table 3.3

Line	Relative Gain = R	$P_T \equiv P_{\text{Threshold}}$ (Mw)
6P _{1/2}	92.2	41.5
7P _{1/2}	5.24	2.7
8P _{1/2}	2.22	0.62
9P _{1/2}	1.71	0.17
10P _{1/2}	1.77	0.06
6P _{3/2}	18.7	415
7P _{3/2}	2.00	44
8P _{3/2}	1.12	13
9P _{3/2}	1.15	4.4
10P _{3/2}	1.00	2.4

From the values of R it is evident that for large values of the pump power the gain for the $J = 1/2$ fine structure component of each line is larger than for the $J = 3/2$ component, and that the gain increases for decreasing values of the principal quantum number n .

It should be mentioned that in this calculation we have considered only susceptibilities of the form χ_{zzzz} or, in other words, we have assumed all the fields are polarized in one direction. It is also possible to have the signal and idler waves polarized perpendicular to the pump since this would involve χ_{yyzz} 's which are allowed by symmetry to be nonzero (see eqn. 3.2). The χ_{yyzz} 's are smaller than the χ_{zzzz} 's for both the $P_{1/2}$ and $P_{3/2}$ cases, however, so the predominant process at high pump power is that for the $P_{1/2}$ states with all fields polarized in one direction.

3.3e Numerical Estimates of Threshold Powers

We have just calculated what we call the high pump power gain which is the gain for pump power well above the threshold pump power. In order to know the range of pump power over which that calculated gain applies we must estimate the threshold power. This is done below by finding the value of G for which $G = \Delta k^2$.

The value used for Δk is k_S'' since, near the resonance, k_S'' is the dominant term in the expression for Δk . The value of k_S'' is calculated from

$$k_S'' = 1.71 \times 10^{-7} Z''(\zeta_{nP}) f \lambda_S N \quad (3.50)$$

where f is the oscillator strength of the $6S_{1/2} - nP$ transition. Using this and the definition of G we find an expression for the threshold power.

$$P_T = \frac{1.71 \times 10^{-7} Z''(\zeta_S) f \lambda_S}{\{2.74 \times 10^{-26} \frac{\omega_I}{\omega_S} Q^2 F(\zeta_{nP}, \zeta_9)\}^{1/2}} \quad (3.51)$$

or

$$P_T = 1.1 \times 10^6 \frac{f \lambda_S}{\left[\frac{\omega_I}{\omega_S} Q^2 \right]^{1/2}} \quad (3.52)$$

The values of P_T calculated in this fashion are listed in table 3.3 in megawatt units.

Comparing these threshold powers with the maximum pump power of ~ 1 Mw we see that P_P can be considerably larger than threshold power for $10P_{1/2}$, $9P_{1/2}$, and $8P_{1/2}$. It is about equal to the threshold for $7P_{1/2}$ but is well below it for $6P_{1/2}$. Since the $J = 3/2$ lines are all predicted to have lower gains than their $J = 1/2$ counterparts and also higher thresholds, we consider only the $J = 1/2$ P states in the following discussions.

The gains calculated above can be used for $P_P \gg P_T$ but what is expected when $P_P \sim P_T$? Since the gain is linear in power at high power yet has a threshold, the slope of $\ln P_S$ vs. $N_{CL} \cdot P_P$ must be greater near threshold than at high pump powers.

3.4 Summary

The results of these calculations of parametric gain can be summarized as follows: the gain profile versus signal wavelength is shown in fig. 3.9 for the case of exact resonance pumping and has a characteristic Doppler width centered on the atomic transitions $6S_{\frac{1}{2}} - nP$. The profile for near-resonant pumping is shown in fig. 3.10. The gain has been calculated for the $10P_{\frac{1}{2}}$ line for the experimental conditions encountered and the gains of the other lines have been calculated relative to the $10P_{\frac{1}{2}}$ gain. These are listed in table 3.3. The threshold powers, which have been estimated assuming negligible populations in states other than $6S$, are also listed in table 3.3.

The following two chapters will expand upon the theory just presented and apply it to the analysis of experimental results. Specifically, chapter four will deal with THG and TPA and chapter five will discuss the parametric process. Factors such as saturation of the various transitions, Stark shifts induced by the laser

radiation, and photoionization from the $9D_{\frac{3}{2}}$ level, which might modify the results presented above, will be discussed.

CHAPTER 4

THIRD HARMONIC AND TWO PHOTON ABSORPTION EXPERIMENTS

The topic of this chapter is the description of a detailed model of third harmonic generation (THG) and two photon absorption (TPA) and a comparison of the predictions of the model with our experimental results.¹²

A glance at some typical data such as that in fig. 4.1 reveals that neither THG nor TPA exhibits the power dependence predicted for it in chapter 3. This failure may be understood when the effect of the radiation field on the atomic state populations is considered. If the fraction (R) of atoms excited to the two photon resonance state ($9D_{3/2}$) is estimated using $R = \sigma_{\text{TPA}} \cdot F \cdot T$ where σ_{TPA} is the cross section calculated in chapter 3, F is the photon flux and T is the pulse duration, we find that R may be as large as 10 for a typical laser pulse. This large population redistribution is in contradiction to the assumption of negligible population shift implicit in the perturbation calculation of chapter 3. Thus a more relevant model must include the intensity dependent redistribution of the atomic state populations.

Such a calculation is presented and discussed in the following section. Subsequent sections will

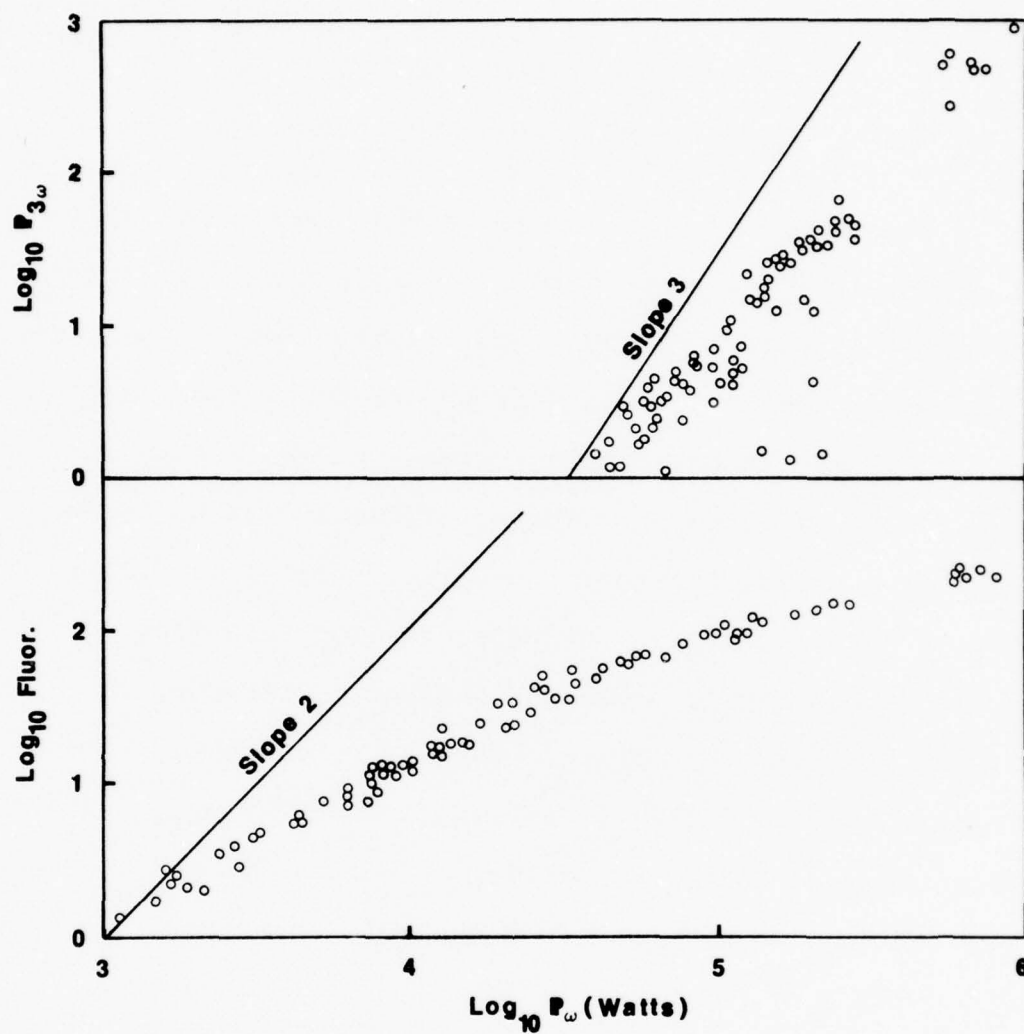


Fig. 4.1

Observed power laws for resonant THG (top) and TPA

compare the model with experimental measurements and discuss the range of validity of the model and present our conclusions.

4.1 Steady State Saturation Model

The calculations presented here are based on a steady state model in which certain transient effects associated with a laser pulse of finite duration are ignored. Expressions for THG and TPA as functions of laser power and frequency will be derived and discussed. Initially only the population redistribution will be considered but later other effects such as Stark shifts and photoionization will be included. Throughout the discussion, the quantities of primary interest will be the lineshapes of the two photon resonance and the power dependences of THG and TPA.

The density matrix formulation of quantum mechanics is well suited to the treatment of process involving large population shifts, and, if a steady state solution is assumed, produces simple expressions for TPA and THG. Such a calculation is presented in Appendix A and the results are discussed here. The steady state assumption means that the population in each atomic state is taken to be time independent during the laser pulse, because the pulse duration is much greater than the relaxation times. For simplicity, we assume that

only the ground state and the two-photon-resonant state attain significant populations. In our case these are the $6S_{\frac{1}{2}}$ and $9D_{\frac{3}{2}}$ states of cesium. For the moment, loss of atoms from the upper state other than by stimulated or spontaneous decay into the lower state are neglected. The incident radiation is assumed to be tuneable and monochromatic.

The expressions derived for the THG and TPA signals are (see Appendix A)

$$\text{TPA} \propto \frac{S}{\sqrt{1+S}} \frac{1}{2T_2 \Delta\omega_9} Z''(x,y) \quad (4.1)$$

$$\text{THG} \propto \frac{1}{\omega} \frac{1}{\Delta\omega_9} \left[Z'^2(x,y) + \frac{1}{1+S} Z''^2(x,y) \right] \quad (4.2)$$

where

$$x \equiv \frac{2\omega - \Omega'_9}{\Delta\omega_9}; \quad y \equiv \frac{\sqrt{1+S}}{T_2 \Delta\omega_9}; \quad \Delta\omega_9 = \Omega'_9 \left[2kT/Mc^2 \right]^{\frac{1}{2}} \quad (4.3)$$

$$S \equiv \frac{1}{2} T_1 T_2 \left(\frac{e}{\hbar} \right)^4 \left| \sum_m \frac{\langle 9D_{\frac{3}{2}} | z | mP \rangle \langle mP | z | 6S_{\frac{1}{2}} \rangle}{(\Omega_{mP} - \omega)} \right|^2 (|E^\omega|^2)^2 \quad (4.4)$$

The quantity S --called the saturation parameter--is a number which indicates the population difference between

the two states $9D_{3/2}$ and $6S_{1/2}$ for those atoms exactly resonant with the radiation. Specifically, for those atoms

$$\rho_{11} - \rho_{22} = (1 + S)^{-1} \quad (4.5)$$

where ρ_{11} is the fraction of atoms in the ground state and ρ_{22} is the fraction in the excited state. The quantities T_1 and T_2 appearing in eqn. 4.4 are respectively the lifetimes of the diagonal and off diagonal terms of the density matrix or, in other words, T_1 is the lifetime of the excited state and T_2 is the inverse of the homogeneous width of $9D_{3/2}$ ($\frac{1}{T_2} = -\frac{\Omega_0''}{2}$). It may easily be shown that an alternative expression for S is

$$S = 2 \cdot \sigma_M \cdot F \cdot T_1 \quad (4.6)$$

where σ_M is the maximum two photon absorption cross section of an atom in the ground state, T_1 is the lifetime of the $9D_{3/2}$ state and F the photon flux in number per cm^2 per second.

We now discuss in detail the expressions for THG and TPA. For this purpose it is convenient to consider three ranges of laser power. The first is the low power range where $S \ll 1$ and $y \ll 1$.

LOW LASER POWER $S \ll 1$ $y \ll 1$

When $S \ll 1$, the quantity $(\rho_{11} - \rho_{22})$ is nearly unity according to eqn. 4.5, so there are few atoms in the excited state. The value of y is also much less than 1 if it is assumed that $(T_2 \Delta\omega_9)^{-1}$ is small. This is equivalent to assuming that the homogeneous line width is much less than the Doppler width. Such is not always the case, of course, but under the conditions of interest to us it is likely to be. In either case, the equations for TPA and THG reduce to

$$\text{THG} \propto P_{\omega}^3 \frac{1}{\Delta\omega_9} Z^2(x, y) \quad (4.7)$$

$$\text{TPA} \propto \frac{P^2}{2T_2 \Delta\omega_9} Z''(x, y) \quad (4.8)$$

where

$$x = \frac{2\omega - \Omega'_9}{\Delta\omega_9} ; y = \frac{1}{T_2 \Delta\omega_9}$$

These are the same results as yielded by the perturbation calculation of chapter 3. This is expected since in both cases it was assumed that $(\rho_{11} - \rho_{22}) = 1$. The salient features in this power range are quadratic and cubic dependences for TPA and THG respectively with lineshapes described by $Z''(x, y)$ for TPA and $Z^2(x, y)$ for THG where x

and y are independent of P_ω . These lineshapes appear in figs. 4.2 and 4.3.

INTERMEDIATE LASER POWER $S \gg 1$ $y \ll 1$

If $(T_2 \cdot \Delta\omega_g)^{-1}$ is sufficiently small, there is a range of laser power over which S is large yet y is still much less than unity. In such a case the equations 4.1 and 4.2 become

$$\text{THG} \propto P_\omega^3 \{ Z'^2(x,y) + \frac{1}{S} Z''^2(x,y) \} \quad (4.9)$$

$$\text{TPA} \propto \sqrt{S} Z''(x,y) \propto P_\omega Z''(x,y) \quad (4.10)$$

where $y = \frac{\sqrt{S}}{T_2 \Delta\omega_g}$.

Recalling that S is proportional to P_ω^2 we see that the TPA lineshape is changed due to the larger value of y . The lineshape is still dominated by Doppler broadening, however, so the change is slight.

The behavior of THG is more complex. At linecenter ($x = 0$) where $Z'(x,y) = 0$, the third harmonic signal is linear in P_ω while off resonance where $Z'(x,y) \gg Z''(x,y)$ it is proportional to P^3 . Thus the linecenter is depressed relative to the wings and a dip appears there. This is illustrated in fig. 4.3.

The physical basis for this is that in this power range a hole is burned in the longitudinal velocity

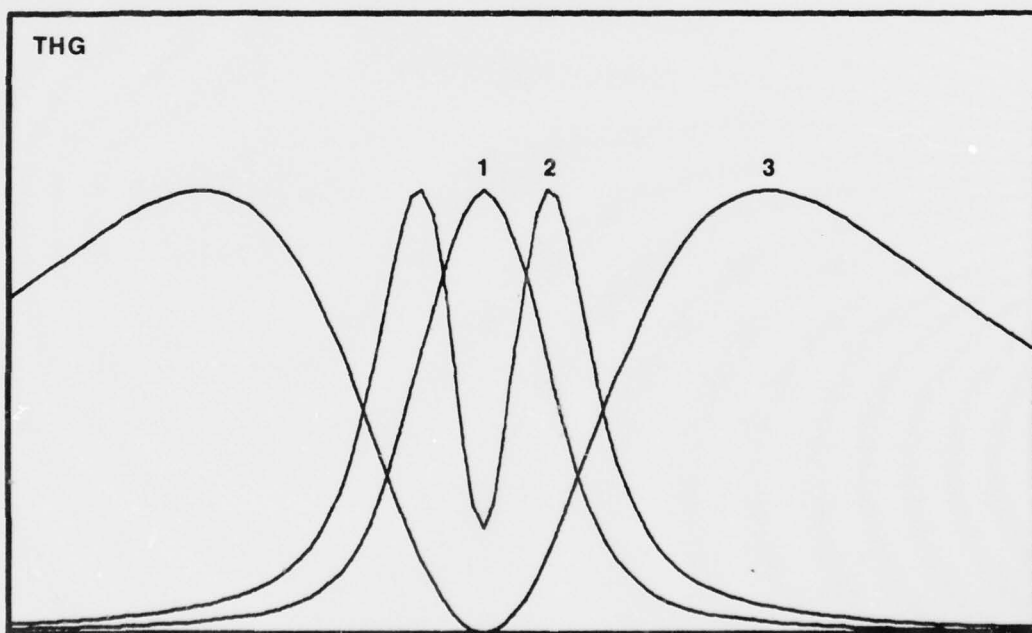
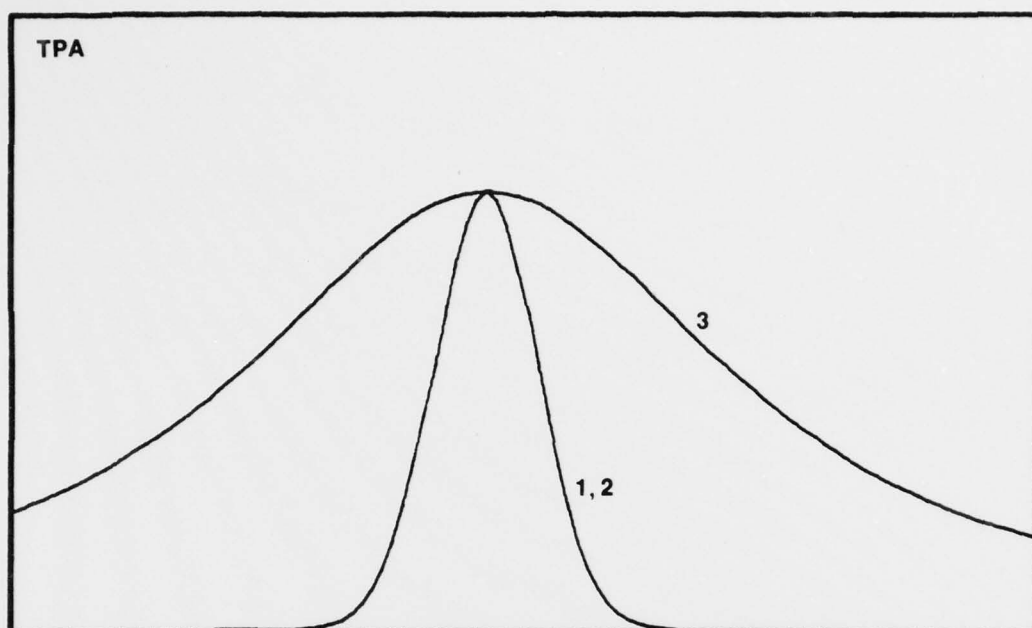


Fig. 4.2 (top): TPA frequency response

Fig. 4.3 (bottom): THG freq. response

$\left\{ \begin{array}{ll} 1 & S \ll 1 \quad y \ll 1 \\ 2 & S = 10 \quad y \ll 1 \\ 3 & S = 10^6 \quad y \approx 13 \end{array} \right.$

distribution of atoms--those atoms which have the necessary velocity along the direction of propagation of the radiation to be Doppler shifted into near-resonance with it are more strongly saturated than nonresonant atoms. Thus, if the quantity $(\rho_{11} - \rho_{22})$ is plotted as a function of the lab frame resonant frequencies, a dip occurs at the radiation frequency. This hole has a width y when measured in units of $\Delta\omega_g$. Since y is proportional to \sqrt{S} or to P_ω , the width of the hole is proportional to laser power, but only a small fraction of all atoms will be saturated since the hole width is much less than the Doppler width ($y \ll 1$). Because the TPA signal is proportional to ρ_{22} , it will be proportional to the hole width multiplied by the density of atoms resonant at the radiation frequency. Thus, the TPA signal should be proportional to P_ω and the lineshape should be nearly the same as at lower radiation intensities.

It is shown in Appendix A that the contribution to the THG signal from atoms of a given resonant frequency is proportional to the value $(\rho_{11} - \rho_{22})^2$ for those atoms. The Z'' term is the contribution from these saturated atoms so THG is expected to be proportional to the square of the number of saturated atoms multiplied by $P_\omega^3 (\rho_{11} - \rho_{22})^2 \cdot Z''^2(x,y)$. Since $(\rho_{11} - \rho_{22})$ is proportional to $1/(1 + S)$, this produces the P_ω power law at linecenter.

The Z' term of eqn. 4.9, on the other hand, is the contribution from non-resonant atoms and retains its P_ω^3 power law so long as $y \ll 1$, which is to say as long as only a small percentage of all atoms is saturated.

HIGH POWER $S \gg 1$ $y \gg 1$

As the radiation intensity increases and y in turn increases, eventually the point is reached where $y \gg 1$. This means that virtually all the atoms will be saturated if $x < y$ (x is the detuning of the radiation from linecenter measured in the same units as y), in which case the TPA signal will be independent of intensity. The signal falls off only if x becomes greater than y , so the TPA linewidth is y . The lineshape for a particular value of y is shown in fig. 4.2. It is nearly Lorentzian in the limit of large y since the Doppler width is then much smaller than the homogeneous width.

For THG, the signal near linecenter ($x < y$) is proportional to P_ω^{-1} . This occurs because all atoms are saturated and the signal is proportional to $(\rho_{11} - \rho_{22})^2$. P_ω^3 or to P_ω^{-1} . For $x \gg y$ the power law is still cubic. The resulting high power THG lineshape is shown in fig. 4.3.

This discussion of the power dependence of line-shapes and power laws for TPA and THG is summarized in the set of figures 4.2 - 4.5. The lineshapes illustrated in figures 4.2 and 4.3 have been referred to above. They

show the lineshapes for TPA and THG for each of the three power ranges.

The corresponding power laws are shown in figs. 4.4 and 4.5. Fig. 4.4 shows the dependence of the TPA signal on P_ω for $x = 0$ and for $x = 1.4$. At the linecenter ($x = 0$) the three power ranges produce the P_ω^2 , P_ω^1 , and P_ω^0 slopes as illustrated in the figure. When $x = 1.4$, the signal saturates to the same value as when $x = 0$ and is proportional to P_ω^2 at low power. The THG power dependence is shown in fig. 4.5. The $x = 0$ curve has the P_ω^3 , P_ω^1 , and P_ω^{-1} slopes discussed above. Notice that detuning from linecenter improves THG efficiency at high powers. This is expected considering the dip at linecenter (see fig. 4.3). In fact, maximum efficiency at high power is achieved for $x \approx y$. Thus, as P_ω increases and y increases, the driving radiation must be detuned in proportion to P_ω to obtain maximum THG. If this is done, the signal will be proportional to P_ω rather than P_ω^{-1} . Thus, if only the contribution from the $9D_{3/2}$ two-photon-resonant state is considered, there is a limiting efficiency of THG and increasing the laser power further would not improve it. Furthermore, this maximum efficiency is obtained by detuning from linecenter by an amount proportional to the laser intensity.

In practice, it may not be necessary to detune the radiation source from linecenter to obtain a P_ω^1 power

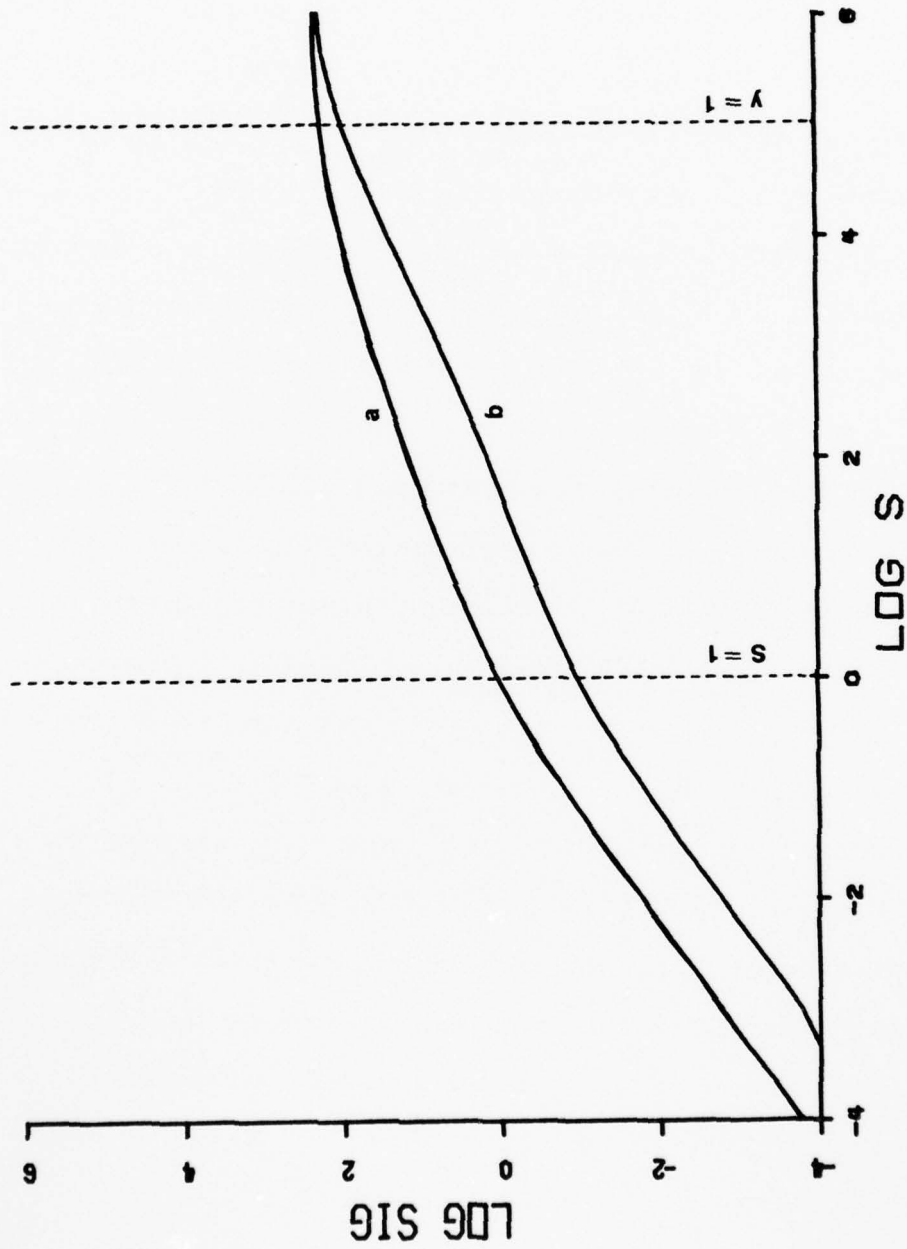


Fig. 4.4
TPA power dependence for $x=0$ (a) and $x=1.4$ (b)

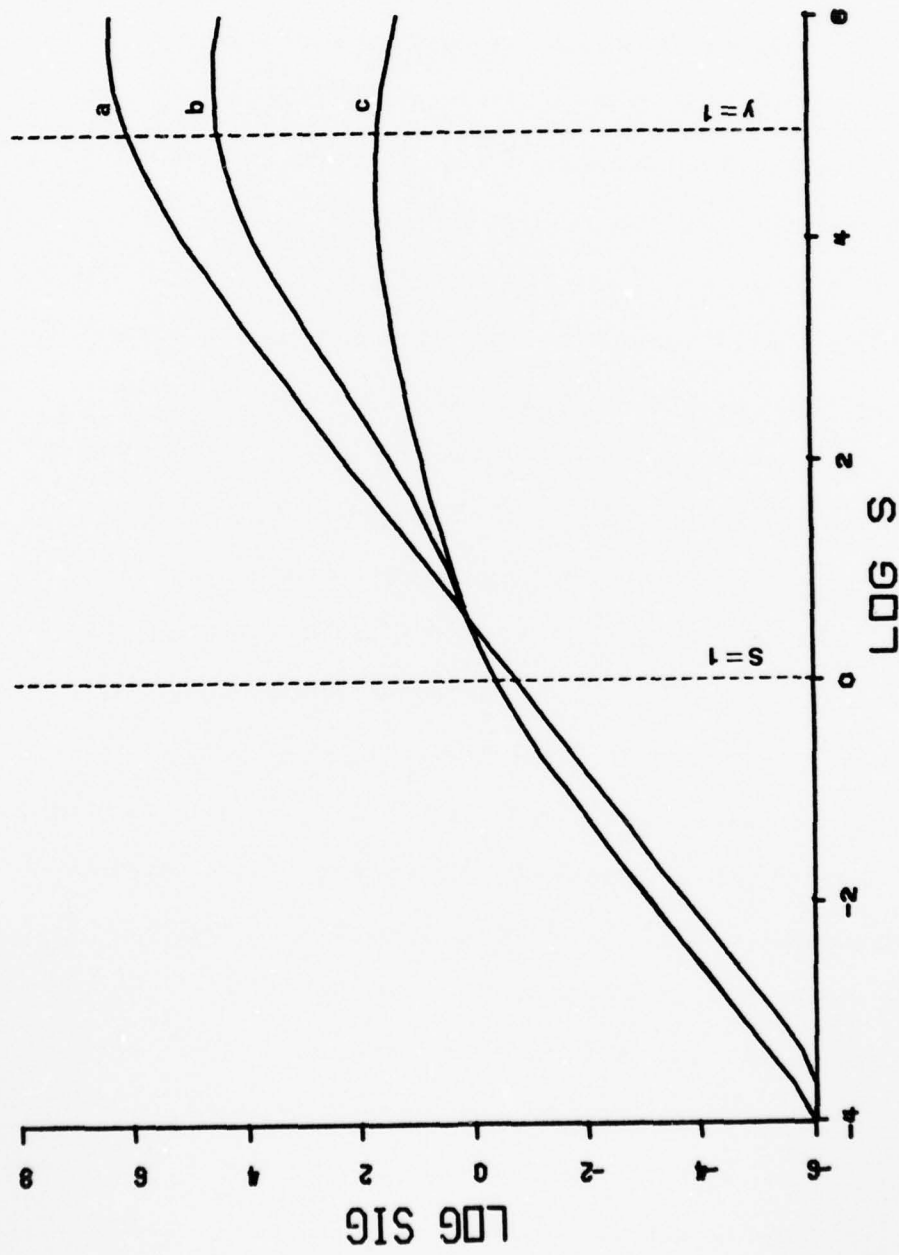


Fig. 4.5
THG power dependence for $x=0$ (a), $x=0.13$ (b), and $x=1.4$ (c)

dependence since the A. C. Stark effect will shift the frequency of the atomic resonance by an amount proportional to the instantaneous intensity.¹³ The shift need not be exactly equal to y to produce a linear intensity dependence. Any shift which is proportional to E_ω will produce the same linear dependence at sufficiently high power, although, of course, it may produce less than the maximum efficiency. The effect of Stark shifts (for $x = 0$) are shown in fig. 4.6. As the Stark effect shifts the dip at linecenter away from the radiation frequency, the THG efficiency is improved. While this is occurring, the exponent of the power law may even be greater than three as in the case illustrated. At high powers ($y \gg 1$, $S \gg 1$) the THG signal becomes linear in pump intensity.

Thus far in the analysis of THG as a function of laser intensity, the role of the wave vector mismatch Δk has been ignored. We have dealt only with the influence of χ , assuming Δk to be constant. However, changing the population distribution also affects Δk because the linear polarizability of the sample at frequencies ω and 3ω changes with population. In addition, the intensity dependent refractive index may be significant in some situations. So long as the sample is only a fraction of a coherence length, our discussion remains valid since index matching is not important. If, however, a sample of several coherence lengths is employed or if index

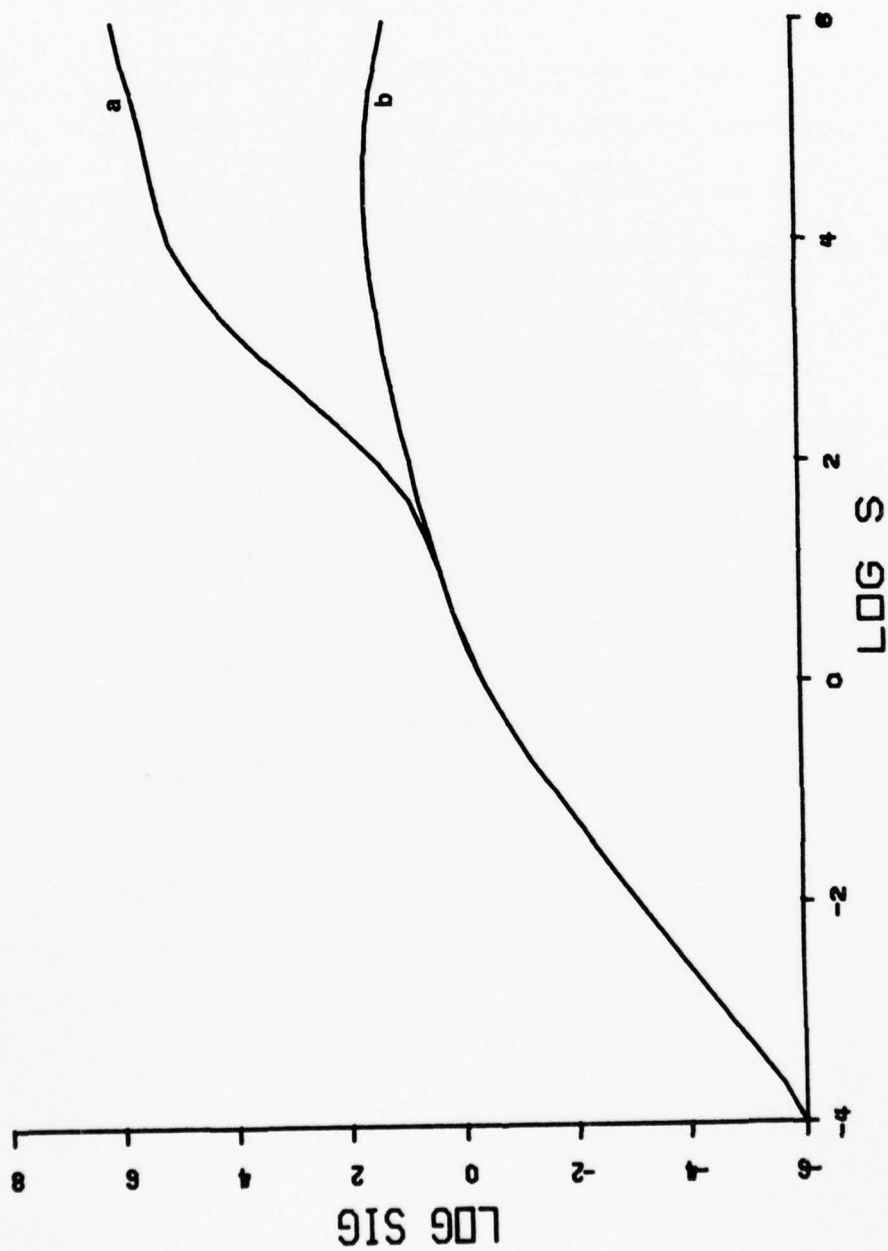


Fig. 4.6
THG power dependence with (a) and without (b) A.C. Stark shift

matching by a second species of atom or molecule with Δk of opposite sign is attempted, then the intensity dependence of Δk can have a significant influence in THG. In our experiments we have about one coherence length of vapor and since Δk increases or decreases by less than one coherence length, the contribution of Δk is not as significant as the changes in χ .

Another process which may be important in TPA and THG is the loss of atoms from the two state system. While this is at odds with the restrictions imposed by the steady state assumption, it will certainly be significant in some experimental situations. The loss can occur by spontaneous or stimulated decay of the upper state to states other than the lower state or by collisional energy transfer or photoionization from either resonant state. Consider, for example, single laser photon ionization of the $9D_{3/2}$ state of cesium. At sufficient radiation intensities the lifetime of this state to photoionization will become less than the low power lifetime. A significant fraction of atoms which are pumped into $9D_{3/2}$ will then be ionized. This will tend to reduce the saturation or increase the value of $(\rho_{11} - \rho_{22})$ and consequently improve THG so long as the population fraction ρ_{11} is not depleted too severely.

In addition, the change in upper state lifetime produced by photoionization may alter the value of γ .

This lifetime broadening of the resonance may change the optimum detuning and perhaps the power law at high intensities.¹⁴

The steady state model cannot accommodate a full description of the system including loss of atoms because the loss is incompatible with the steady state assumption. Other methods which can take these factors into account will be discussed in a later section.

4.2 Comparison of Model and Experimental Results

In order to compute the lineshapes and power laws for the cesium - ruby laser system, it is necessary to know the values of line widths, hyperfine structure, Stark shifts, etc. The estimates of these will be discussed first and then the predictions of the steady state model based upon these will be compared with observations.

A list of values for various parameters (at one coherence length) is given below

$9D_{\frac{3}{2}}$ Lifetime	=	25	ns
Homogeneous Linewidth	\geq	6.5	Mhz
Doppler Linewidth	=	1200	Mhz
2 x Laser Mode Separation	=	250	Mhz
2 x Laser Mode Width	\geq	5	Mhz
$6S_{\frac{1}{2}}$ Hyperfine Splittings	=	9200	Mhz
$9D_{\frac{3}{2}}$ Hyperfine Splittings	\approx	10	Mhz

$$\begin{aligned}\text{Stark Shift } (6S_{\frac{1}{2}} - 9D_{\frac{3}{2}}) &= 825 \text{ Mhz} \times E(\text{MW}) \\ \text{Photoionization Lifetime } 9D_{\frac{3}{2}} &= 4 \text{ ns}/E(\text{MW})\end{aligned}$$

These are discussed individually below.

The $9D_{\frac{3}{2}}$ lifetime was measured in two ways. The first consisted of estimating the decay time of $9D_{\frac{3}{2}}$ from oscilloscope traces of the fluorescence at the $9D_{\frac{3}{2}} - 6P_{\frac{3}{2}}$ transition frequency (See fig. 4.7). Since the decay time is comparable to or longer than the laser pulse at low cesium densities, the time constant can be estimated. It is about 30 ns at one coherence length and about 100 ns at 1/3 CL so it is density dependent with a lifetime of ~ 30 ns at the density of interest. This is to be compared to a calculated radiative lifetime of 210 ns.⁴ These estimates were confirmed by measurements of the total fluorescence signal from the same transition integrated over the time from the beginning of the laser pulse to 100 ns after the end of the pulse as a function of cesium density. This data (shown in fig. 4.8) was fit by a simple model including photoionization of $9D_{\frac{3}{2}}$, spontaneous decay, and collision induced decay at a rate proportional to cesium density. The proportionality constant for the latter was chosen to provide a fit to the data and from it the collision induced lifetime was estimated. Assuming a square laser pulse, the change in population of $9D_{\frac{3}{2}}$ may be approximated by

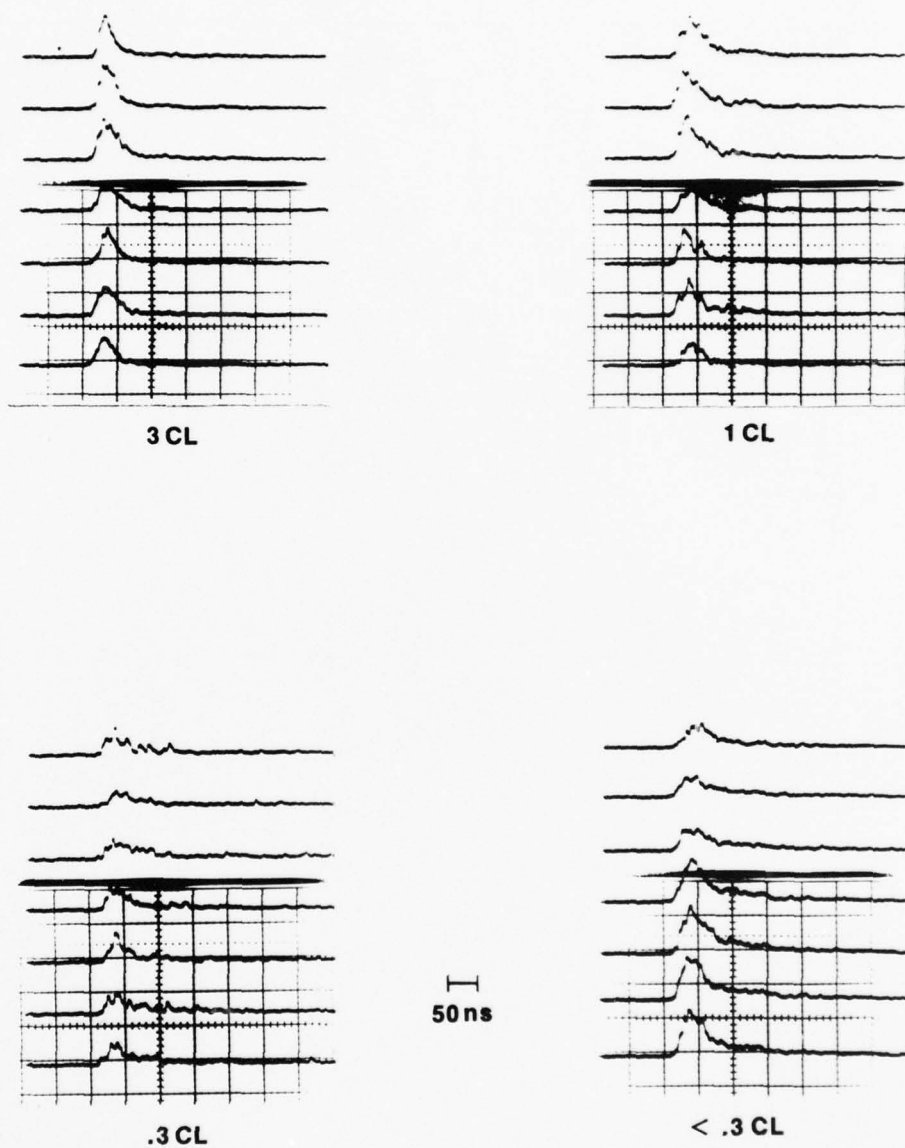


Fig. 4.7

Oscilloscope traces of fluorescence signal at various cesium densities (50 ns/major div.)

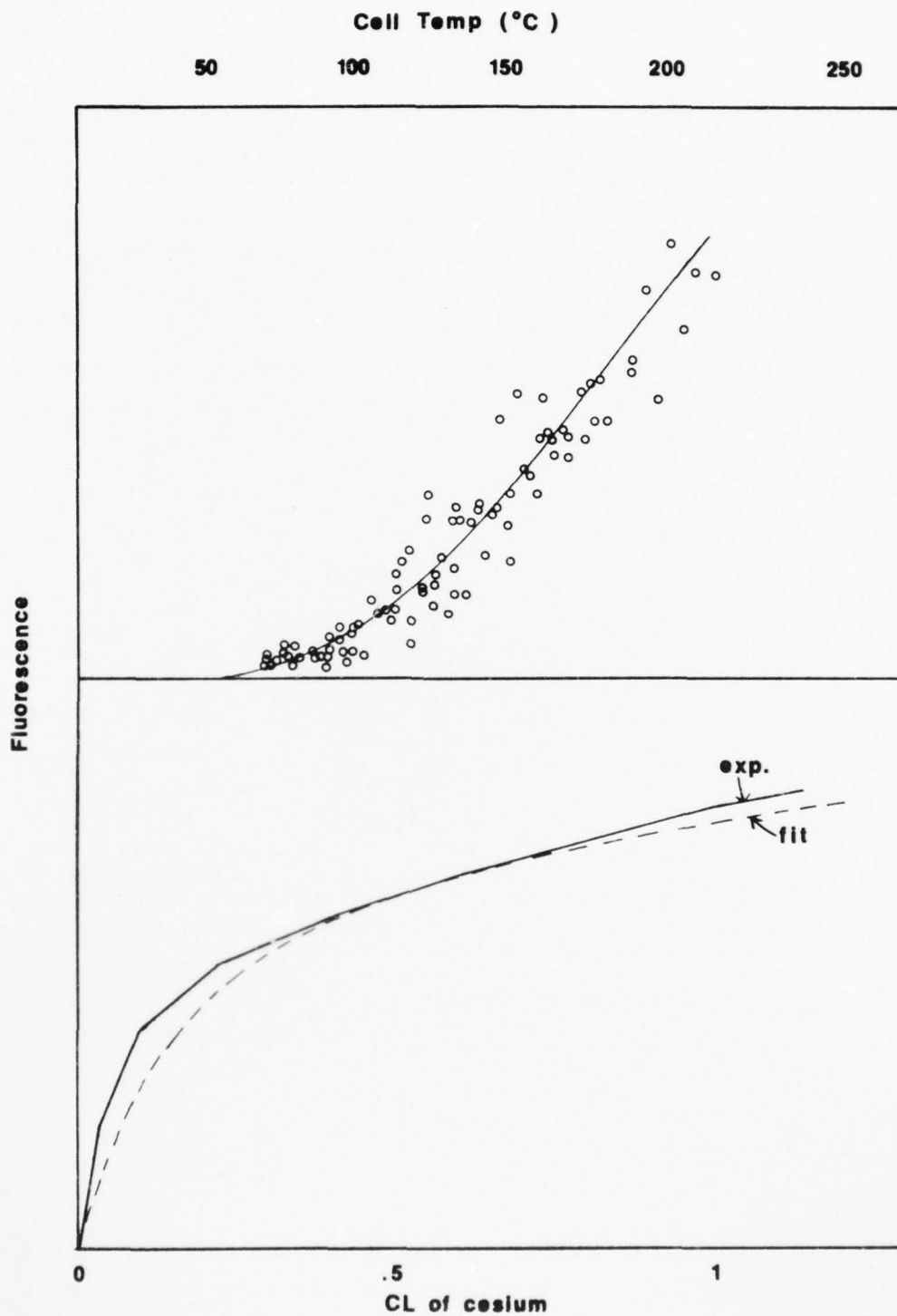


Fig. 4.8

Top: Fluorescence as a function of cell temperature
 Bottom: exp. curve is from data in top part, fit
 curve is for a lifetime of 25ns/#CL

$$\frac{dn}{dt} = \rho A - nC - n\rho D - nB \quad (4.11)$$

where ρ is the cesium density in coherence lengths, C^{-1} is the natural or radiative lifetime of $9D_{3/2}$, B^{-1} the photoionization lifetime, and D the constant we wish to find. When this equation is integrated over time to find $\int_0^\infty n(t)dt$ which is proportional to the TPA signal, and the best estimates for A , B and C are used, ($B^{-1} \approx 10$ ns, $C^{-1} \approx 150$ ns, $T \approx 20$ ns), a value for D^{-1} of 25 ns produces the curve labeled "Fit" in fig. 4.8. This is insensitive to small changes in T and B . The conclusion is that the collision induced lifetime is 25 ns/ ρ_{CL} .

The value listed for the homogeneous linewidth is a minimum value deduced from the $9D_{3/2}$ lifetime. In all likelihood the actual value is considerably larger than this due to line broadening from Cs - Cs collisions. For the present the homogeneous width will be written as $\beta \times 6.5$ Mhz where β is a number greater than unity.

The next width on the list, the Doppler width, is calculated using a temperature of 210°C corresponding to the cesium density at one coherence length.

The laser mode separation is the separation of adjacent longitudinal modes calculated using $\Delta\nu = c/2L$ where L is the optical length of the laser cavity. This value is confirmed by observing the beat frequency between cavity modes.

AD-A067 075

MICHIGAN UNIV ANN ARBOR DEPT OF PHYSICS
THREE RESONANT NONLINEAR OPTICAL PROCESSES IN ATOMIC CESIUM.(U)
MAY 77 A V SMITH

F/G 7/4

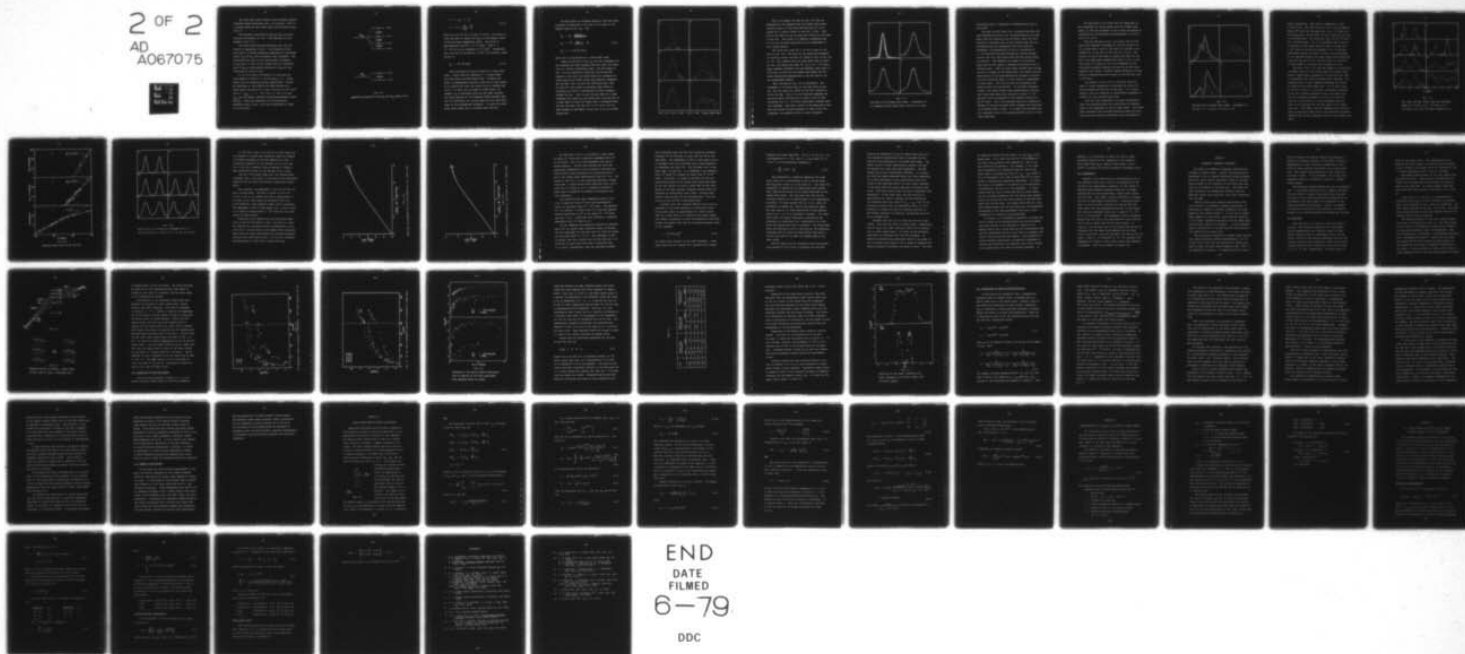
AFOSR-77-3225

UNCLASSIFIED

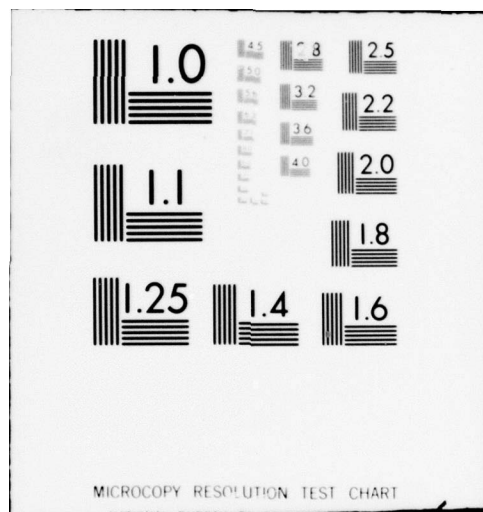
AFOSR-TR-79-0366

NL

2 OF 2
AD
A067075



END
DATE
FILMED
6-79
DDC



The laser mode width listed is the transform limited frequency spread associated with a 30 ns pulse. This is a minimum value but the actual value should differ little from it.

The hyperfine splittings of $6S_{1/2}$ and $9D_{3/2}$ are those reported by Svanberg, et. al.¹⁵ The structure is diagrammed in fig. 4.9.

The Stark shift and photoionization rate are calculated in appendices B and C. The direction of the Stark shift is toward increasing separation of the energy levels $6S_{1/2}$ and $9D_{3/2}$ with increasing laser intensity. The photoionization rate is for single photon ionization of $9D_{3/2}$ only, as this is much larger than the ionization rate of $6S_{1/2}$ or multi-photon ionization of $9D_{3/2}$ for the conditions of interest here.

We now have enough information to calculate the laser powers at which $S = 1$ and at which $y = 1$. These powers will be labeled P_S and P_Y respectively. Earlier we found that R , the fraction of atoms excited by a laser pulse, was unity for a laser intensity of 10^7 w/cm² where $R = \sigma_{TPA} \cdot F \cdot T$. The value of T was 30 ns and σ_{TPA} was the Doppler averaged two-photon-absorption cross section. Using the expression for the saturation parameter given in eqn. 4.6, S may be expressed in terms of R as follows.

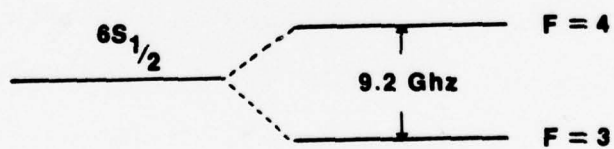
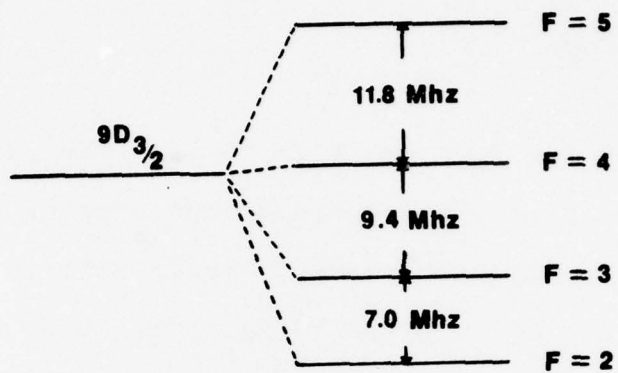


Fig. 4.9

Hyperfine structure of the $6S_{1/2}$ and $9D_{3/2}$ states of Cs

$$S = 2 \sigma_M \cdot F \cdot T_1 \quad (4.12)$$

$$S = 2 R \cdot \frac{\sigma_M}{\sigma_{TPA}} \cdot \frac{T_1}{T}$$

where T_1 is 25 ns for 1 CL and T is 30 ns. The ratio of cross sections is simply the ratio of the Doppler width to the low power homogeneous width. This ratio is approximately $1200/(6.5 \times \beta)$ or $185/\beta$. Thus $S = (3 \times 10^3)/\beta$ for an intensity of 10^7 W/cm^2 . Considering that the area of the beam is $.03 \text{ cm}^2$, this yields a value for P_S of

$$P_S = 10^4 \sqrt{\beta} \text{ watts} \quad (4.13)$$

This calculation of P_S was based on a single mode laser. Since there are typically 4 - 6 laser modes, the power must be divided among them. Assuming the power is predominantly shared by only two or three modes, as is usually the case, the value of P_S is changed very little. If there are two modes of equal power, for example, P_S is unchanged since the two modes saturate the atoms resonant at the frequency midway between them just as effectively as a single mode with the same total power at the intermediate frequency. If there are three equal power modes, P_S is increased less than 50%.

As laser power is increased above P_S , the hole width increases in proportion to P_ω until it is equal to the Doppler width at $P_\omega = P_Y$. Thus

$$P_Y = P_S \cdot \frac{\text{Doppler}}{\text{Homogeneous}}$$

$$P_Y = 10^4 \cdot \frac{1200}{6.5 \times \beta} \cdot \sqrt{\beta} \quad (4.13)$$

$$P_Y = 2 \times 10^6 / \sqrt{\beta} \text{ watts}$$

Again this is calculated for a single mode laser.

These calculations of P_S , P_Y , and the lineshapes are now compared with data obtained when the laser was operating on a single longitudinal mode. The data shown in fig. 4.10 was obtained by measuring the TPA and THG signals as the laser was tuned across the resonance between $9D_{3/2}$ and the higher energy $6S_{3/2}$ hyperfine component. The top pair (Fig. 10a and 10d) and bottom pair (Fig. 10c and 10f) were taken on alternate laser shots to eliminate any drift in calibration of laser frequency between the two. Pair 10a and 10d was taken at a laser intensity well below P_S ; the second pair (10b and 10e) at a laser power of about 10^5 watts with a collimated beam; and the last pair (10c and 10f) at 10^5 watts with the beam focused at the center of the cell by an 18 cm focal length lens.

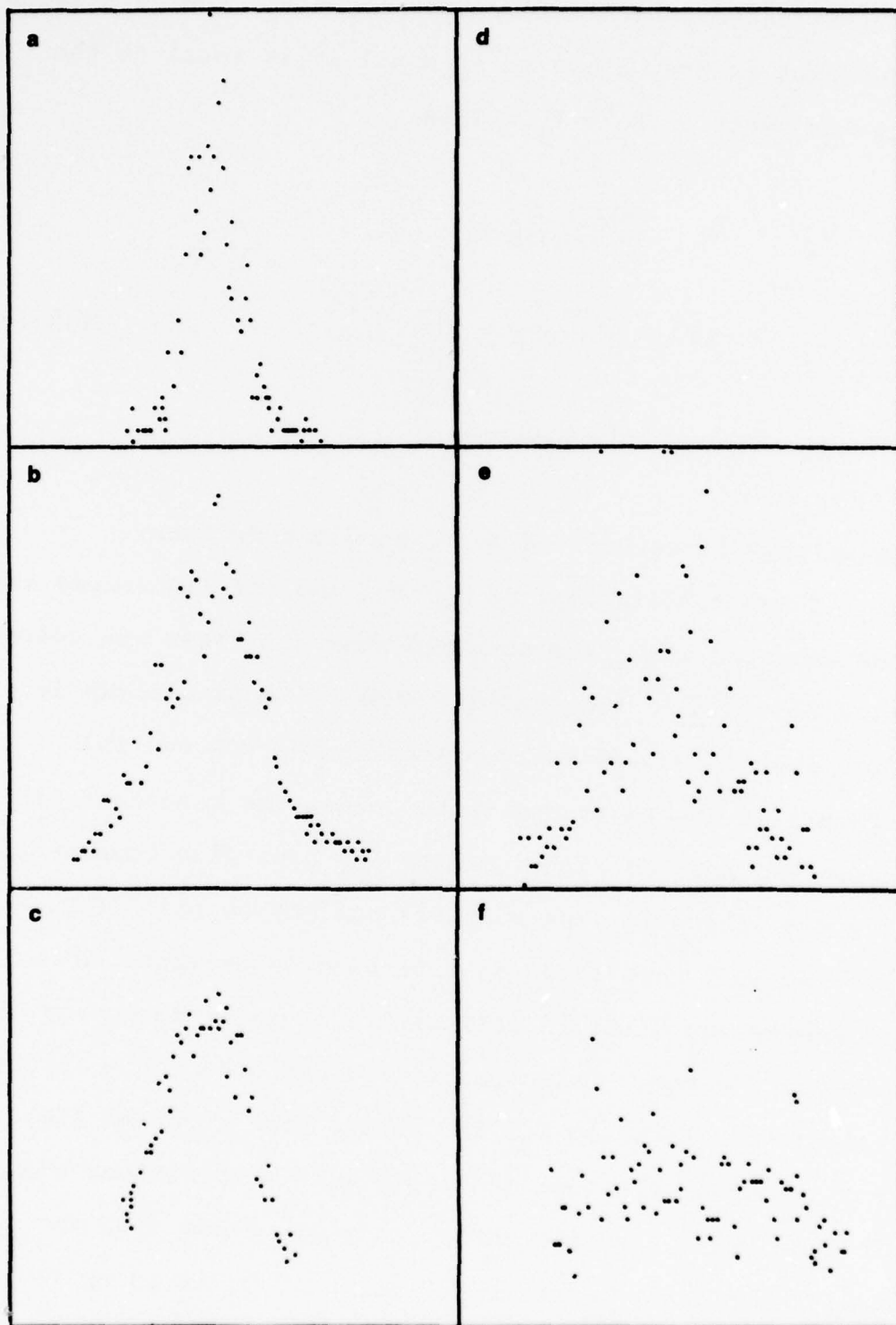


Fig. 4.10 a,b,c = TPA d,e,f = THG Single mode laser

First, we compare the data of fig. 10a with the lineshape for TPA computed from the steady state model. Various values of β are tried and the best fit is obtained for a value of about 50 (see fig. 4.11a). That this is the best fit may be seen most clearly in the wings of the line. This value of β implies a dephasing time of 1 ns for the state $9D_{3/2}$ which is not unreasonable at this cesium density.

Now using this value for β , we fit a curve to the data in fig. 10b. The value of the saturation parameter is varied to obtain the best fit (shown in fig. 4.11b) for $S = 40$. This implies that the laser power used to generate fig. 10b should have been $\sqrt{S} \cdot P_S$ or 4.5×10^5 watts which compares favorably with the measured laser power of 10^5 watts, so thus far the steady state model has provided satisfactory explanations of the TPA data at low and intermediate powers.

Next, the data of fig. 10c is considered. The lineshape is fit fairly well by the same curve as was fig. 10b, but there is a shift to the left relative to 10a by 300 Mhz. This is in the direction expected for the Stark shift and the size is close to the 375 Mhz calculated for 4.5×10^5 watts laser power inferred from the lineshape. Note that a shift in 10b should be of the same size since the same intensity is used to fit the lineshape, but possible drifts in laser frequency

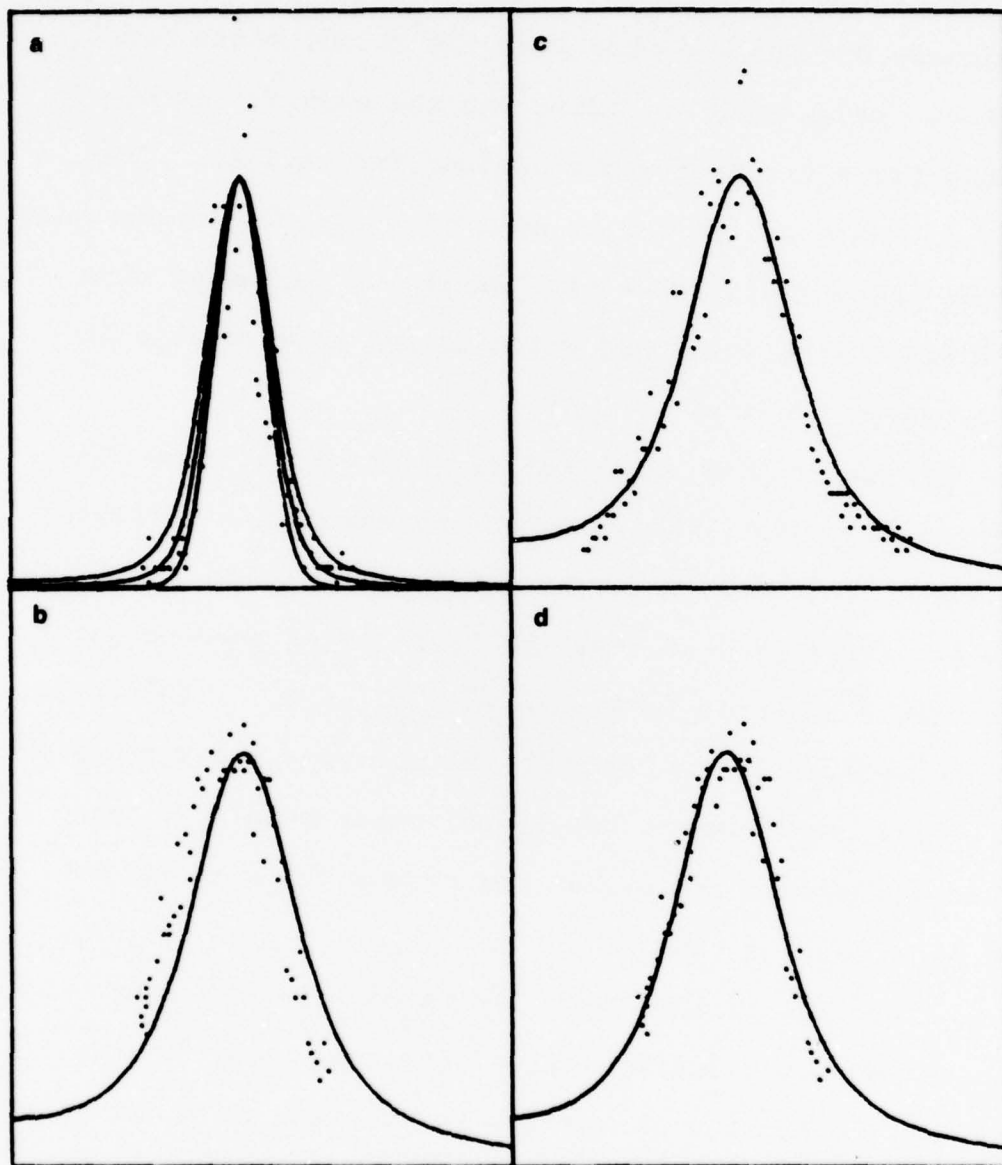


Fig. 4.11

TPA data fit by steady state model. Lineshape in b is computed without Stark shift; that in d is with.

calibration make it impossible to determine the size of this shift.

Why does the TPA signal for a focussed beam have the same resonance profile as the collimated beam of the same power when the intensity near the focus (where the fluorescence is observed) must be much greater than for the collimated beam and consequently the line should be broadened? The explanation is that at intensities of 5×10^5 watts/cm² the photoionization lifetime becomes shorter than the laser pulse width and most cesium atoms are ionized. This depletes the number of fluorescing atoms and the TPA signal is expected to decrease with increasing power. When the laser power becomes great enough for this to happen at the beam center, the signal from the weaker parts of the beam dominate and instead of decreasing with increasing power, the TPA signal is independent of laser power. This can be shown by integrating the signal across the beam profile. As the power increases further, the signal always comes predominantly from that part of the beam where the intensity is about 3×10^6 watts/cm² which corresponds to the maximum intensity at $\frac{P}{\omega} 10^5$ watts. Thus, the lineshape should not continue to broaden nor should the Stark shift increase with intensity if a Gaussian beam is used. In a sense this verifies that the calculated value of the photoionization rate is of the right magnitude.

The conclusion to be drawn from the comparison of TPA lineshapes at various powers with the steady state model, is that the agreement is well within the bounds of uncertainty of calculations and measurements in all details if β is 50.

Next the THG data in fig. 4.10e and 4.10f are compared with computed lineshapes for various values of S . It is found that S must be less than 5 to provide a reasonable fit to the data of 10e (see fig. 4.12a). The value of 40 which was found to provide the best fit for TPA at the same power produced the result in fig. 4.12b. Thus there is a factor of 10 or so difference in the saturation parameter deduced from the TPA and THG lineshapes at this power. Another notable difference is that there is substantially more scatter in the THG data than in TPA data.

The scatter in fig. 4.10f is likewise large and makes it almost impossible to determine the value of S which provides the best fit to the data. It is clear, however, that the resonance is considerably broadened or shifted for this focussed beam case.

With the laser operating on a single longitudinal mode, the available power was insufficient for measurements of the dependence of THG on laser power. The higher power available from multimode operation makes this possible and also provides information about lineshapes at

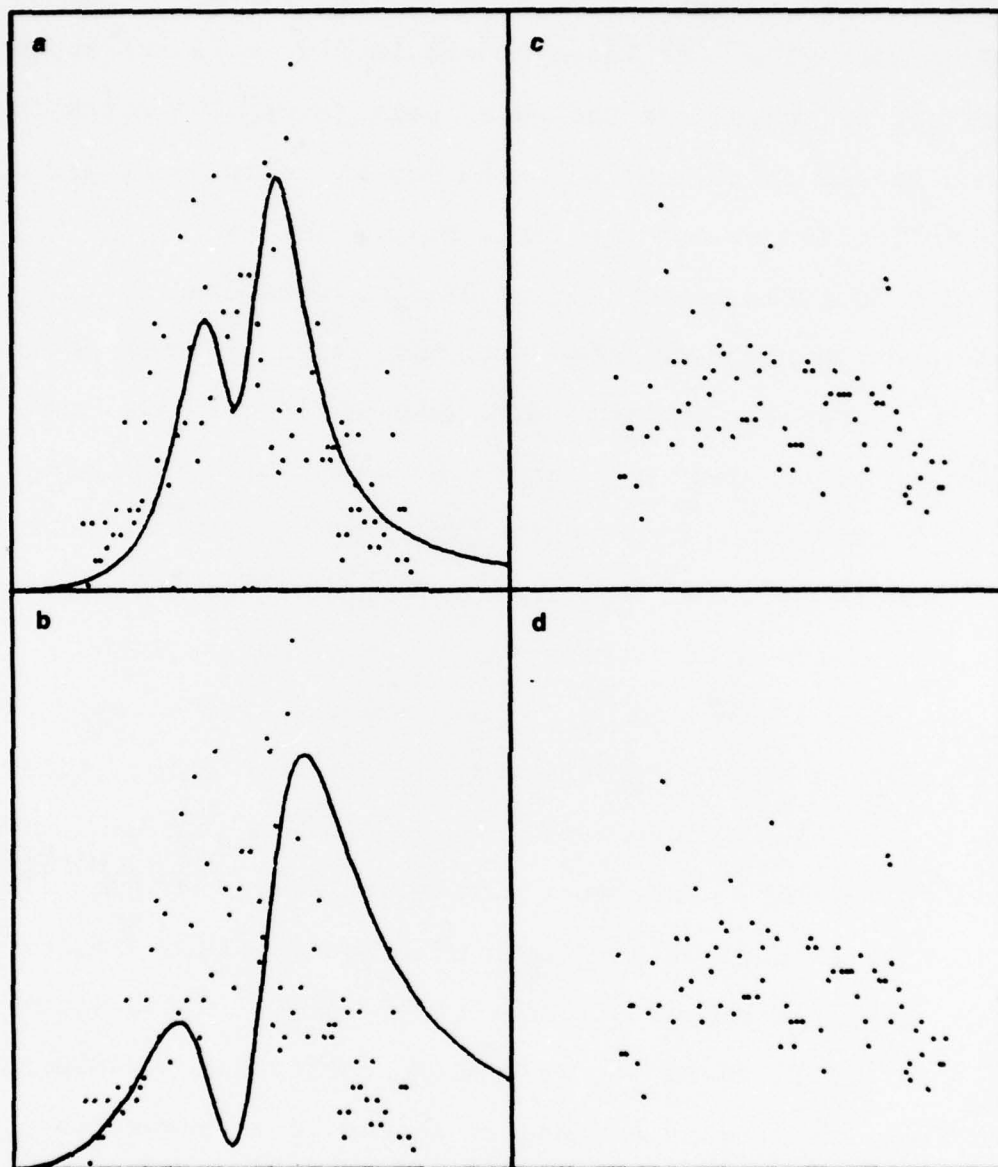


Fig. 4.12

THG data fit by steady state model. Lineshape in a is for $S = 4$; that in b is for $S = 40$.

higher intensities. This data is reproduced in figs. 4.13 and 4.14. The laser powers in fig. 4.13 are approximately 10^4 watts for the upper pair (a,e), 10^5 watts for the second pair, and 10^6 watts for the third pair all with a collimated beam. The final pair (d,h) is for 10^6 watts and a focussed beam. Fig. 4.14a presents data on THG as a function of laser power when the laser is tuned about 1 cm^{-1} from the two photon resonance, 14.b is the same measurement except the laser is tuned to the linecenter of the resonance between the upper ground state hyperfine level and $9D_{\frac{3}{2}}$, and 14.c is the TPA signal as a function of laser power at the same laser frequency as 14.b.

The data of fig. 4.13 has been compared to calculated lineshapes much as in the single mode case except three modes of equal power separated by 700 Mhz have been used to approximate the actual multimode laser spectrum. The characteristics of the computed lineshapes are similar to those for the single mode case. At 10^5 watts (figs. 4.13b and f) there is, as before, noticeable broadening of the TPA lineshape compared to the lower power case, and the saturation parameter is found to be about 20 (see fig. 4.15b) which is in good agreement with the value of 40 estimated for the same power in the single mode case. Once again, the THG lineshape shows less evidence of saturation than TPA and the saturation parameter deduced from the THG lineshape cannot be much greater than unity.

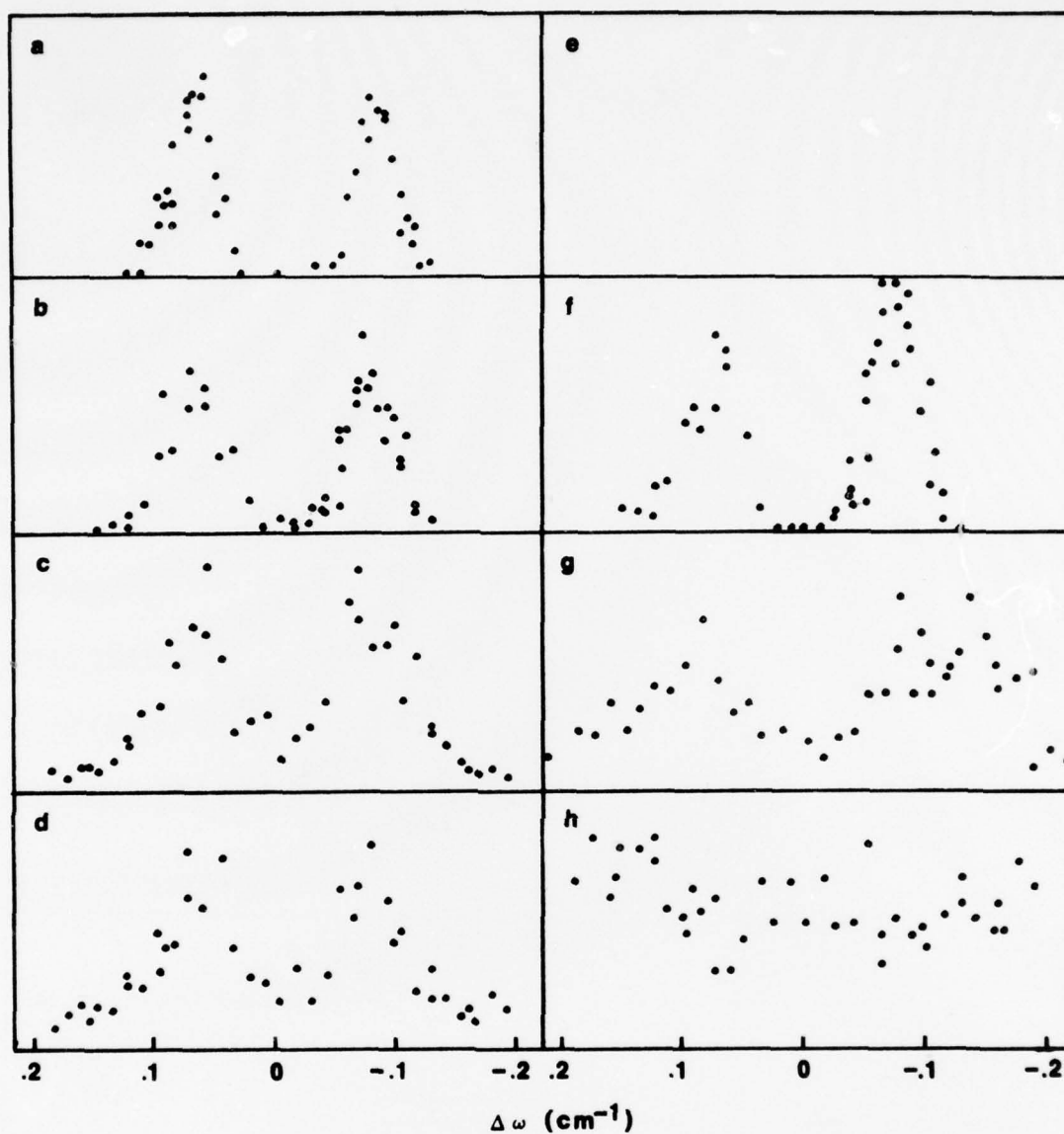


Fig. 4.13

TPA (left) and THG (right) data for multimode laser at 10^4 watts (a,e), 10^5 watts (b,f), 10^6 watts (c,g), and 10^6 watts focussed (d,h).

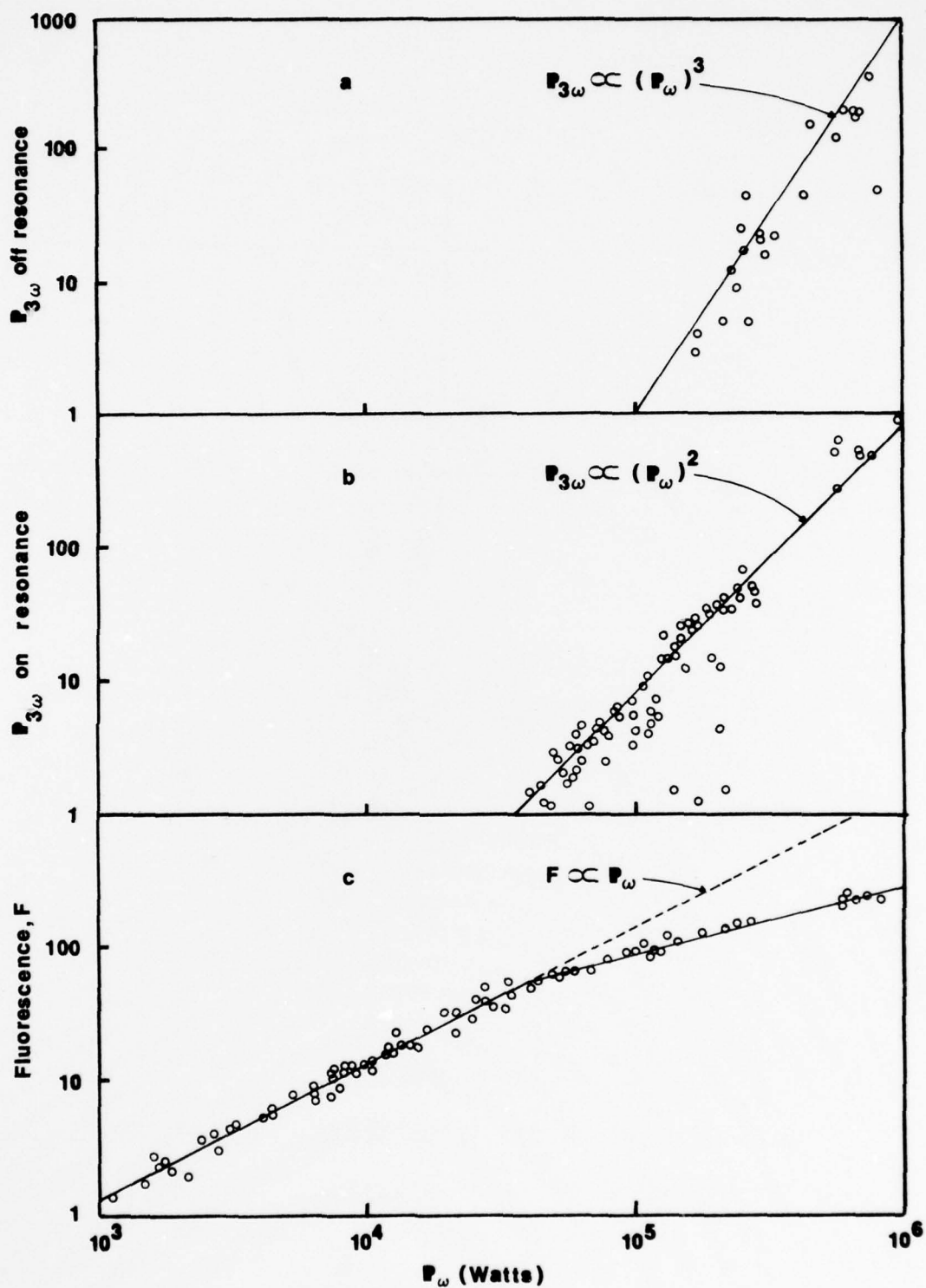


Fig. 4.14

Observed power laws for TPA and THG

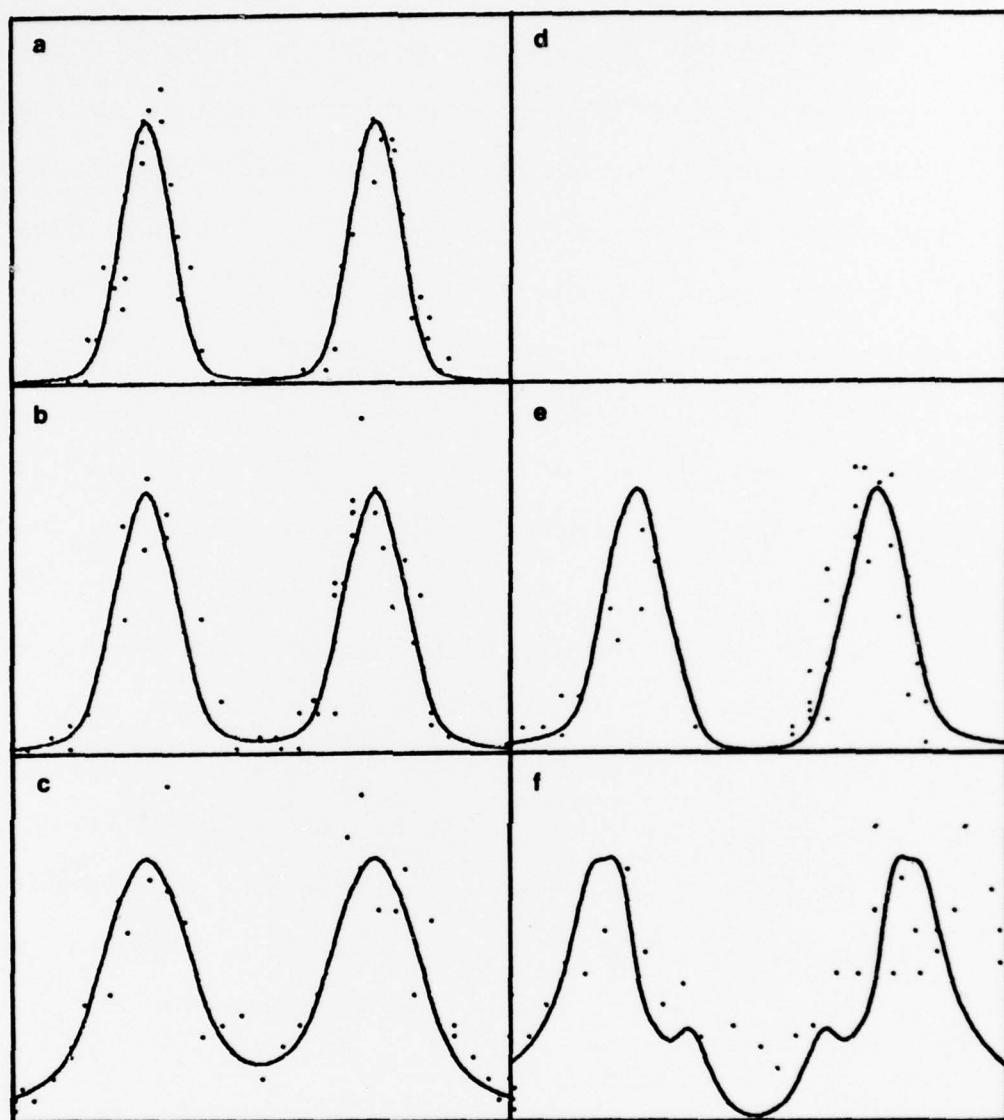


Fig. 4.15

Data of fig. 4.13 fitted by lineshapes for $S = .1$

(a), $S = 20$ (b), $S = 200$ (c), $S = .1$ (e), $S = 40$ (f)

At 10^6 watts (figs. 4.13c and g)--a power which was not possible in single mode operation--there is evidence of further broadening of TPA and especially of THG. A saturation parameter of 140 provides a fit to TPA (see fig. 4.15c) but a smaller value of perhaps 40 yields a more satisfactory match to the THG data (fig. 4.15g).

Just as in the single mode case, the focussed beam lineshape (fig. 4.13d and h) is the same as the unfocussed shape for TPA but again THG exhibits considerable broadening.

Next consider the dependence of the TPA and THG signals on laser power. The data is shown in fig. 4.14. In fig. 4.14a it is evident that THG is proportional to the cube of the laser power off resonance while fig. 4.14b indicates a near quadratic power law on linecenter. The dependence of TPA on laser power (fig. 4.14c) is seen to be linear at powers below 5×10^5 watts and less than linear at higher powers.

These are to be compared with the calculated power laws for THG and TPA shown in figs. 4.16 and 4.17, which are computed for linecenter tuning corresponding to fig. 4.14b and c, and are based on the steady state saturation model using the three laser modes and including hyperfine structure and Stark shifts with $\beta = 50$ but not including photoionization or other loss of atoms from $9D_{3/2}$.

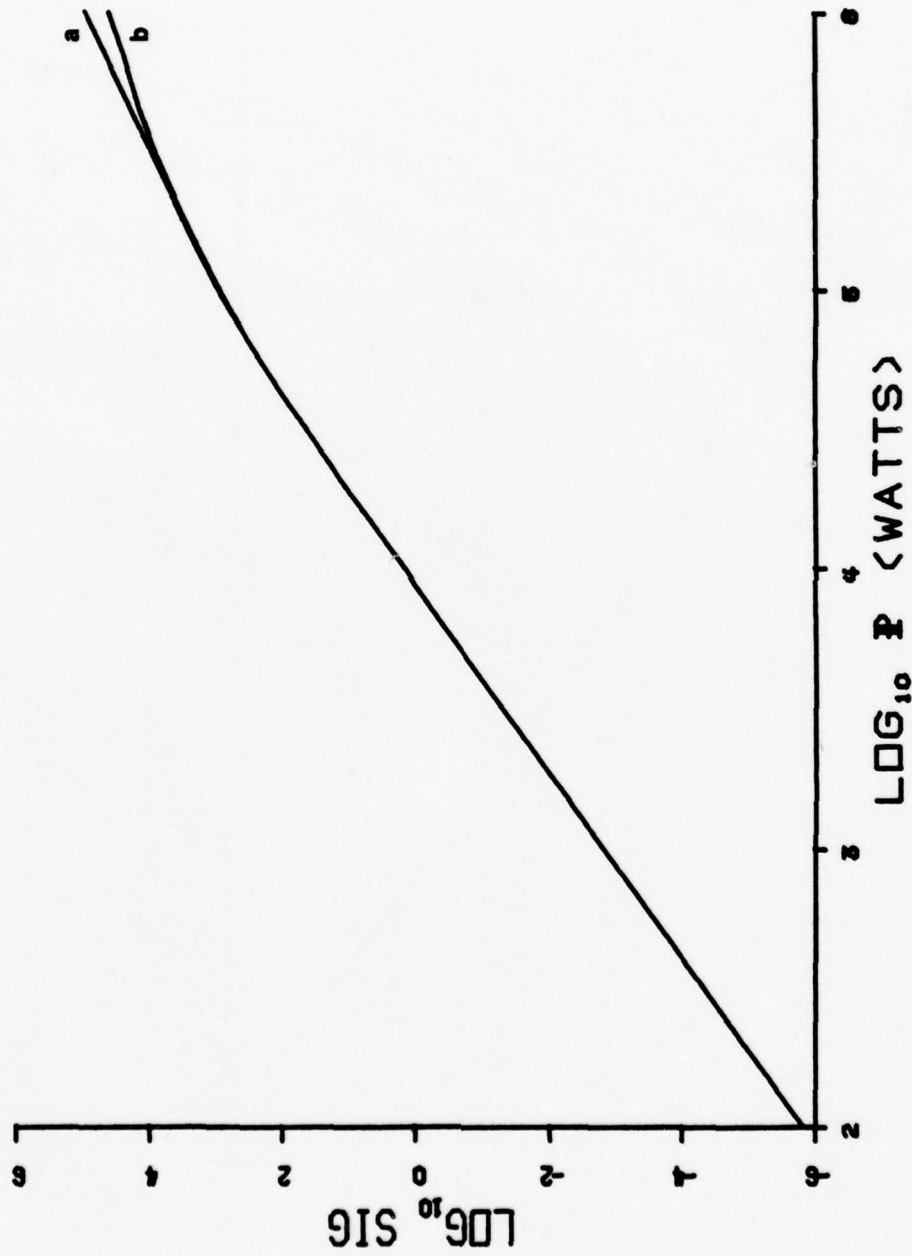


Fig. 4.16

TPA power law computed with (a) and without (b) A.C. Stark shift

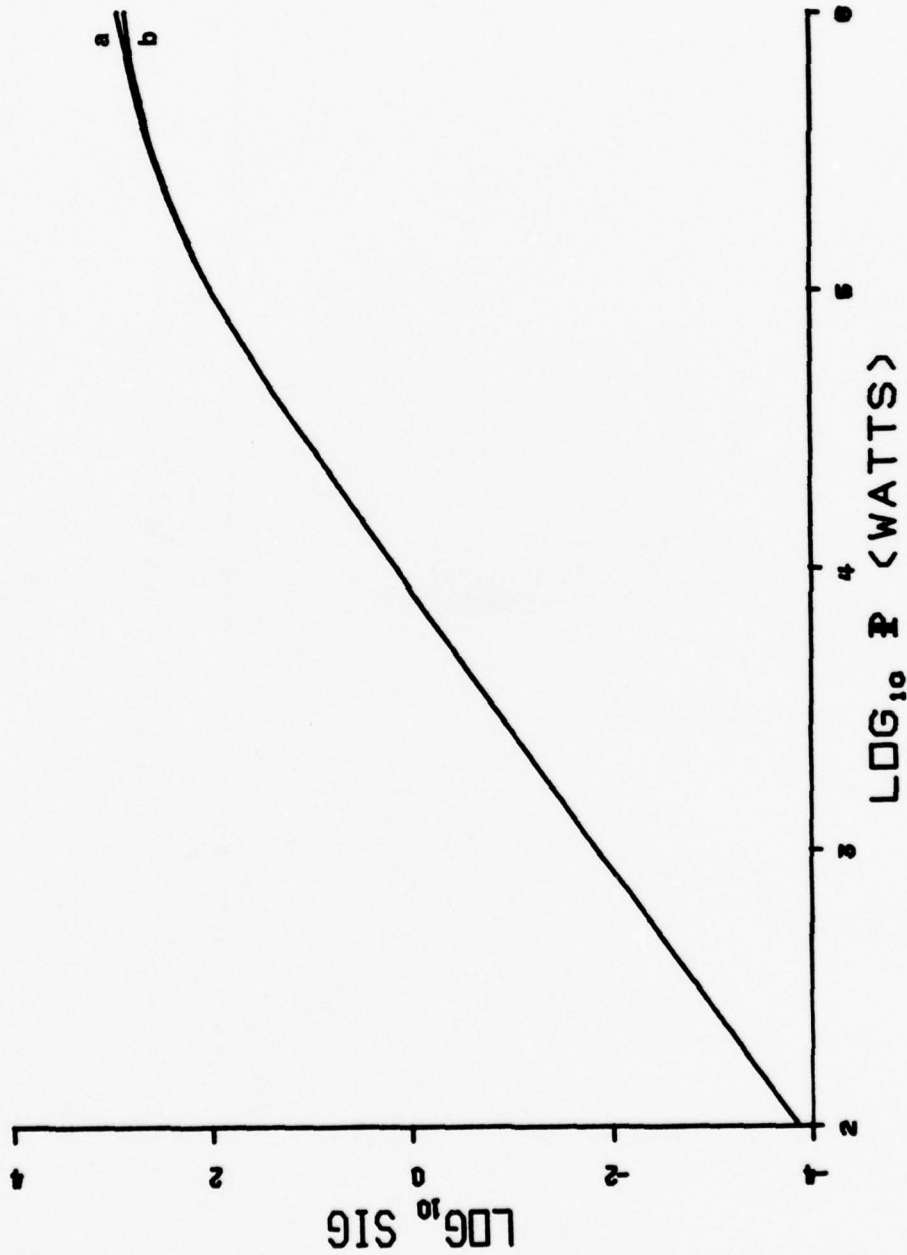


Fig. 4.17

THG power law computed with (a) and without (b) A.C. Stark shift

The THG curve of fig. 4.17 exhibits a cubic power law below 10^5 watts and a quadratic dependence from 10^5 to 10^6 watts. This is in good agreement with the observed behavior. You may have noticed that this computed power dependence is quite different from that presented earlier when discussing the characteristics of THG in the steady state approximation (see fig. 4.5). The reason is that fig. 4.5 was calculated assuming a single laser mode, a single ground state hyperfine level, and a value for β of unity so it is a somewhat unrealistic model used to dramatize the effects of saturation and line broadening.

The calculated TPA power dependence shown in fig. 4.16 is quadratic below 10^5 watts and approximately linear in the power range $10^5 - 10^6$ watts. The measured law, in contrast, is linear below 10^5 watts and approximately proportional to $P^{1/2}$ in the range $10^5 - 10^6$ watts (see fig. 4.14c). Additional data indicates a quadratic dependence below 10^3 watts or so.

We can summarize the comparison between our measurements and the steady state saturation model as follows. The TPA lineshapes fit the model well for both the single and multimode cases if β is 50. The lineshapes of THG in general show more scatter than the TPA data and it is difficult to match each curve with a calculated one. It is clear, nevertheless, that the resonance broadens

with increasing power and that the saturation parameter necessary to fit THG data is lower than for TPA at the same power. The dependence of THG on laser power also is in agreement with the calculated value, being quadratic at linecenter and cubic off. The TPA power law, on the other hand, is puzzling. It is expected to be quadratic below 10^5 watts but instead is linear from 10^3 to 10^5 watts. Once again, it should be pointed out that the calculations based on the steady state saturation model do not take account of loss of atoms from the two state system nor do they consider transient effects which are important at sufficiently short times. Perhaps these effects could account for the discrepancies. The role of each in TPA and THG is discussed below.

Consider first the transient behavior which will be important if the pulse duration is sufficiently short. If the laser pulse is approximated as a square pulse, then for a time after it is turned on the atomic system will exhibit precession in which the population oscillates between the ground state and the two-photon-resonant state at the frequency

$$\omega = \left[S / (2T_1 T_2) \right]^{1/2} \quad (4.14)$$

for those atoms resonant at the laser frequency. Those atoms which are not resonant will precess with a higher

frequency but lower amplitude. For $T_1 = 25$ ns, $T_2 = 1$ ns (corresponding to $\beta = 50$), and $S = 1$, the value of ω is $(7 \text{ ns})^{-1}$, so the precession frequency is

$$\nu = \frac{P_\omega}{P_S} \cdot \frac{1}{7} \text{ GHz} \cdot \frac{1}{2\pi} \quad (4.15)$$

This precession is damped by dephasing the atoms which occurs on a characteristic time T_2 and by decay from $9D_{\frac{3}{2}}$ which occurs on a time scale T_1 . Only after the precession is damped and the populations have reached their equilibrium values is the system described by the steady state model. How long does this take and can transient behavior be of significance in our experimental situation? At times greater than T_2 (1 ns), after the precession is damped out, simple rate equations apply. The time required to reach equilibrium is then approximately $T_1/(1 + S)$ or T_2 whichever is greater. For those atoms which are highly saturated at equilibrium the precession is significant for a nanosecond or so after which the equilibrium value is achieved. For those atoms which are saturated little at equilibrium, the population difference may not reach its equilibrium value until a time of the order of T_1 after the leading edge of the laser pulse.

The TPA signal will be influenced little by precession because it is so short in duration but the slow

build up of population in $9D_{3/2}$ for those atoms which are only slightly saturated will tend to decrease the TPA from the value predicted by the steady state model. The effect is not of major significance, however, and does not explain the linear TPA power dependence. The THG signal may be more significantly affected. It is possible that the signal generated during the first nanosecond or so when precession is most significant could be as large as that generated during the much longer remainder of the pulse since the signal then may be strongly saturated. This would tend to make the dip at linecenter less pronounced. On the other hand, the slow build up to equilibrium will tend to increase the THG coefficient off resonance since the value of $(\rho_{11} - \rho_{22})$ will on the average be greater than its equilibrium value, so it is difficult to assess the role of transient behavior on THG without resorting to numerical calculations which we do not attempt here.

Consider next the loss of atoms from the two state system. This loss may occur in several ways. Photoionization of $9D_{3/2}$ by the laser radiation field will be significant at laser powers above $\sim 10^5$ watts as was discussed previously in connection with the TPA lineshape. In addition stimulated and spontaneous decay of $9D_{3/2}$ atoms to any of several lower energy P and F states is possible and several parametric processes are known to occur. The loss

of atoms will affect the TPA signal, Δk , and χ_{THG} in different ways. It is clear that TPA will be decreased by the loss of $9D_{3/2}$ atoms but the response of χ and Δk are more difficult to ascertain. For example, χ will under some circumstances be increased since the loss of $9D_{3/2}$ atoms tends to increase the value of $(\rho_{11} - \rho_{22})$ while it will be decreased if the loss of atoms from $6S$ is severe enough to decrease the population difference. Of course, the value of Δk depends on the details of the population redistribution and like χ is time dependent. It seems likely that the loss of atoms from the two state system and the resulting departure from the steady state approximation can account for the large scatter in THG data compared with the TPA data. The losses affect THG in a much more complex manner than TPA and there may be considerable differences in the time development from shot to shot considering the variety of loss mechanisms.

Of course, it is conceptually possible to include the loss of atoms due to photoionization and other processes plus Stark shifts in the equations of motion of the density matrix and to solve them for the instantaneous THG and TPA coefficients and for Δk and then to integrate over time to find the TPA and THG signals. This procedure requires extensive application of numerical techniques in solving and integrating the equations with little insight to be gained about the roles of various processes. In

addition, it is difficult to model the loss of atoms accurately because of the complexity of the system in which decay from $9D_{3/2}$ to several lower energy P and F states is possible and several parametric processes occur.

4.3 Conclusions

Because of the difficulties in characterizing all of the processes which play a role in the production of TPA and THG in our experimental situation, we have chosen to identify those physical processes which are of primary significance and have constructed a simple model including only them. This model is quite successful in accounting for our experimental observations. Saturation broadening of the two photon resonance for TPA and THG with laser power have been demonstrated and are in good agreement with the predicted values over a range of 33×10^3 to 33×10^6 watts/cm². The broadening of TPA is somewhat greater than for THG at any given power but this could be due to loss of atoms from the two level system. In addition, the THG power law fits the model both on and off resonance over the power range examined and the Stark shift is verified. Only the TPA power law does not fit the model. From 33×10^3 watts/cm² to 33×10^7 watts/cm² the dependence is linear in laser power rather than quadratic as expected. This we are unable to account for.

CHAPTER 5

PARAMETRIC FREQUENCY CONVERSION

The theory of parametric frequency conversion was outlined in chapter three. Briefly, the process may be considered to be two coupled three-wave mixing processes which can, under certain conditions, result in an exponential growth of the intensity of the signal and idler waves at the expense of the pump wave. The signal and idler typically have frequencies different from the pump and, before being amplified, much lower intensities than the pump.

Several authors have reported observations which they attribute to parametric frequency conversion, in particular in vapors of rubidium, potassium, and water pumped by high powered lasers.¹⁶ In the case of cesium vapor pumped by a ruby laser, Leung observed radiation at two signal frequencies emanating from the sample when only the pump (laser) was incident.⁴ We have extended Leung's observations to include detailed observations of four signal and two idler waves.

The calculations presented in chapter three indicate that under conditions achieved experimentally (1 CL of Cs and 1 MW at 693.5 nm) the conversion of energy from pump to signal and idler should approach 100%. This is not achieved in practice. To understand why not and to

discover whether the observed signals are indeed produced by a parametric process, we have made a series of measurements of signal and idler intensities as functions of laser intensity and tuning, and of cesium density. The temporal characteristics of the signal has also been studied. To our knowledge, this is the first systematic study of a parametric process in a simple atomic system.

The following section presents most of our parametric data. In succeeding sections we will compare this data with the theory of chapter three and discuss the modifications of that theory necessitated by population redistribution and other effects not considered in the simple perturbation calculation. Finally, we examine the question of whether we have observed a parametric process of the type postulated and conclude that we have.

5.1 The Data

When the laser, at a power of 1 MW, was tuned to the $6S_{1/2} - 9D_{3/2}$ two-photon resonance of Cs and passed through approximately one coherence length of vapor, strong radiation near the wavelengths 348 nm, 362 nm, 389 nm, and 457 nm was observed emanating from the cell colinear with the laser radiation. These are the wavelengths associated with transitions from nP to $6S$ when $n = 10, 9, 8$, and 7 respectively. We shall refer to

these as the signal waves. The wavelengths were not measured precisely enough to resolve the fine structure of the P states so the signal waves are indicated in fig. 5.1 without specifying which j level is involved.

The maximum combined power of the four signal waves was about ten watts. Each wave was collimated and co-linear with the pump beam and had nearly the same diameter as the pump beam. No strong signals other than those mentioned were present in the range of 350 to 450 nm.

Idler waves at 1.4 μm and 3 μm corresponding to transitions from $9D_{3/2}$ to 7P and to 8P were also studied. Again, fine structure of the P state was unresolved. The other idlers expected at the $9D_{3/2}$ - 9P and $9D_{3/2}$ - 10P transition frequencies were outside the spectral range of our detector and so were not observed.

The temporal behavior of the total combined signal wave power is illustrated in fig. 5.2. The first pulse of each trace is the parametric signal and the second is the pump pulse delayed by about 35 nanoseconds. They were recorded with a photodiode - oscilloscope combination with a subnanosecond risetime. Notice that the signal wave pulses follow quite closely the pump pulses, but the modulation of the pump is generally exaggerated in the signal. Further analysis of similar data reveals a power dependent shift in the time delay between the points

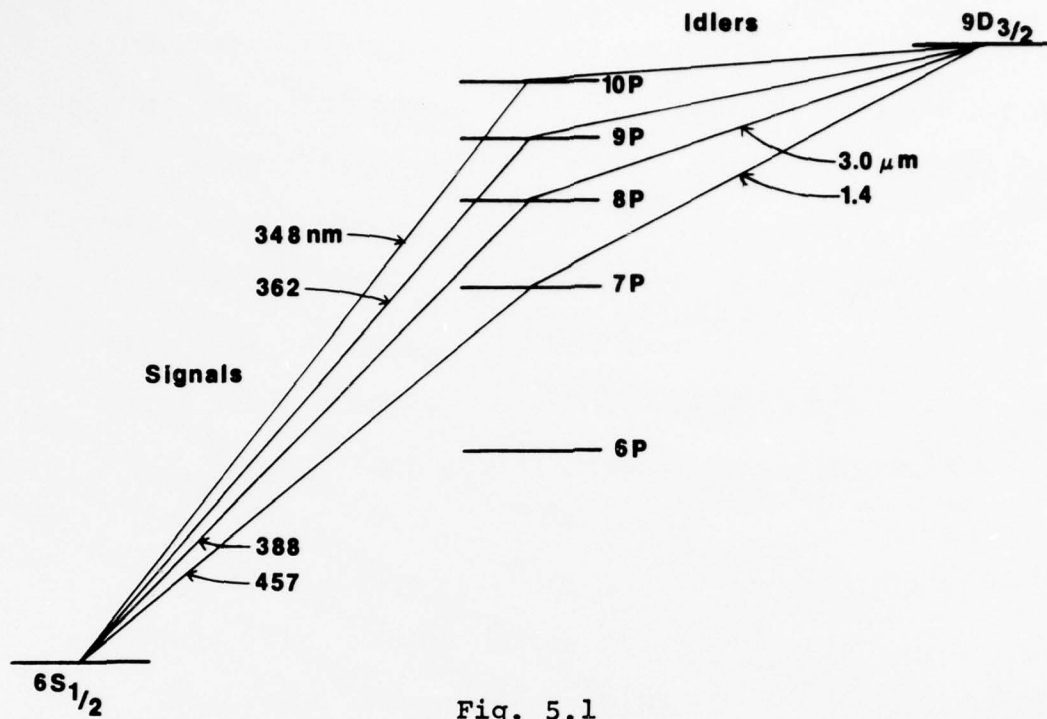


Fig. 5.1

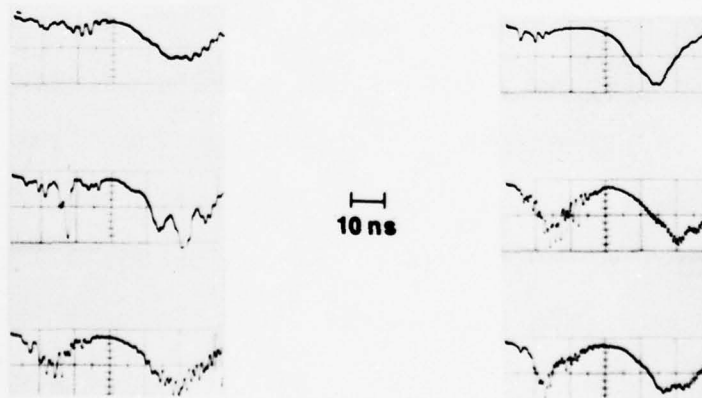


Fig. 5.2

Temporal behavior of signal. Signal pulse on left, pump on right. (10ns/major div.)

of maximum power of the two pulses. The delay increases by about two to four nanoseconds when laser power is doubled in the range of a megawatt, but the pulse shape is not substantially altered.

The strength of the individual signal waves were measured as functions of laser (pump) power, cesium density, and laser frequency. This data is presented in figures 5.3 - 5.6. Figure 5.3 depicts the dependence of the 10P signal (348 nm) energy on laser or pump power for three values of cesium density. Notice that the energy ranges over more than nine decades which is typical for the signal waves; the lower limit of detectable signal being about ten photons and the maximum power produced being typically about a few watts. Similar data for the other three signal waves are shown in fig. 5.4. Fig. 5.5 shows the density dependencies of the 8P and 10P signal waves. Like the power function curves, these indicate that the signal gain is large at low signal powers but saturates at a signal power of a few watts. The dependence on laser frequency of the 10P signal may be seen in fig. 5.6. The upper curve is for a laser power of 1 MW; the lower is for 100 kW. Saturation is again evident in flat tops of these curves.

5.2 Comparison of Data and Theory

From the data presented in figures 5.3 - 5.5 we deduce the small signal gains for the four parametric

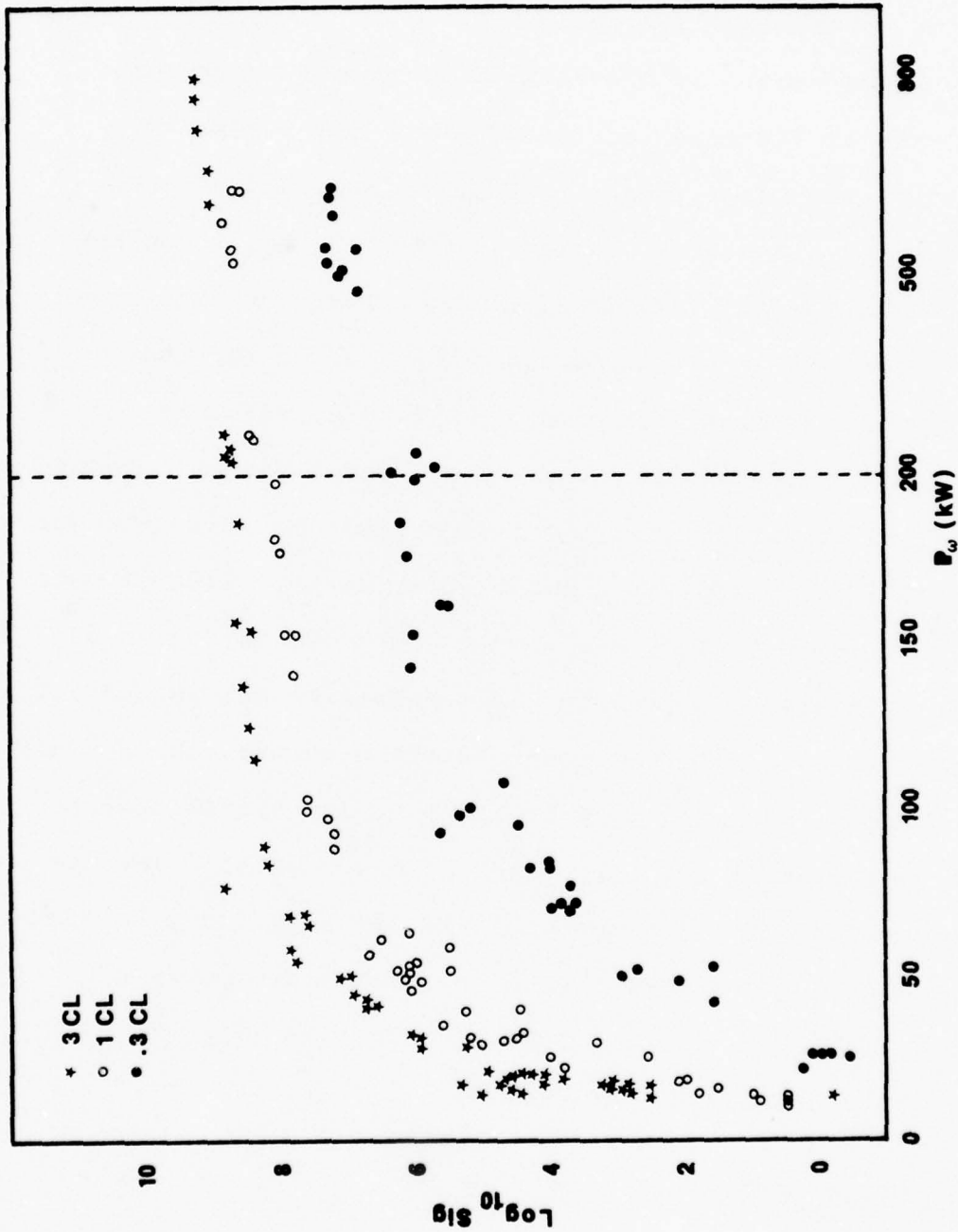


Fig. 5.3
10P parametric signal as function of pump power. Note scale change at 200 kW.

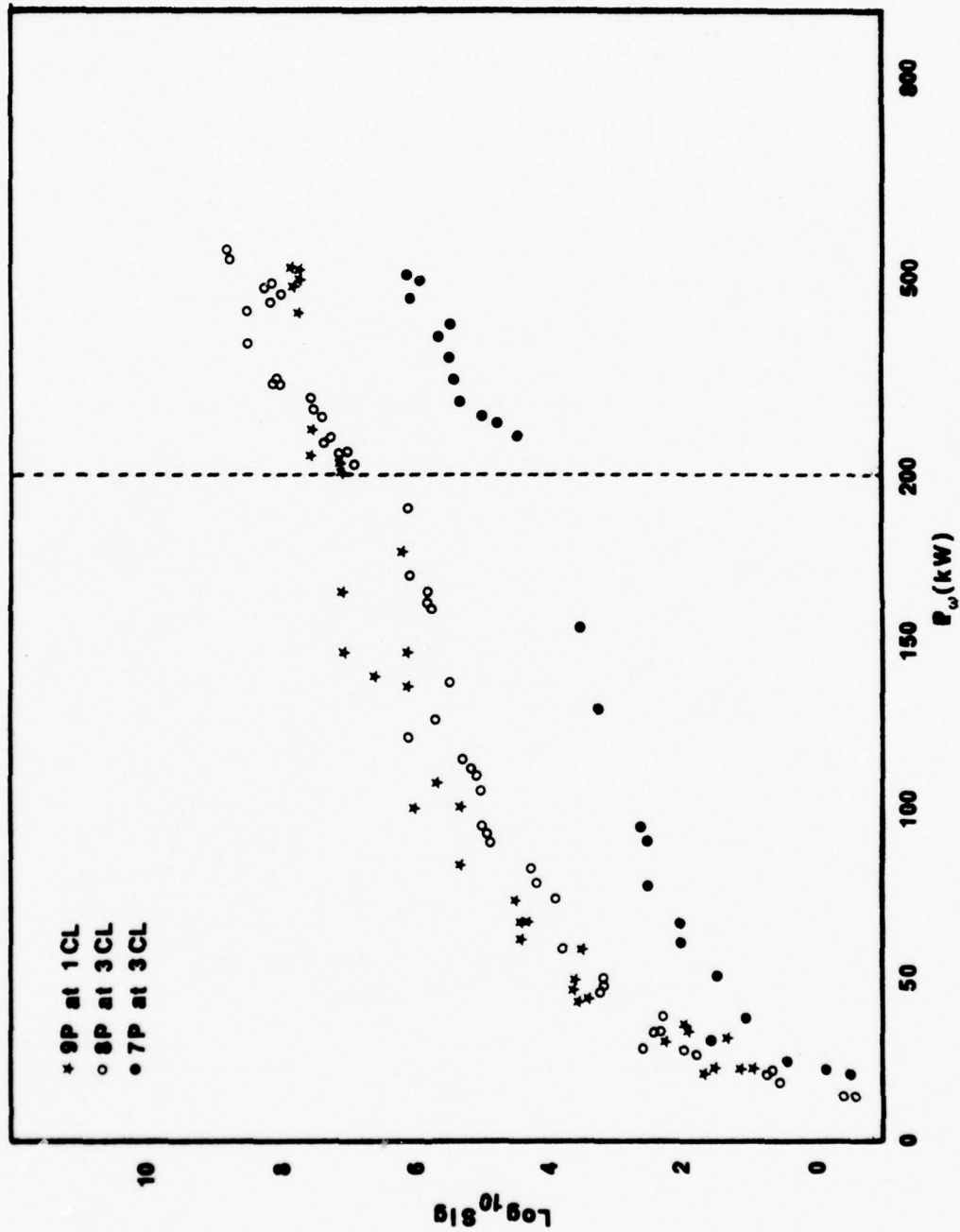


Fig. 5.4 9P, 8P, and 7P parametric signals as functions of pump power.

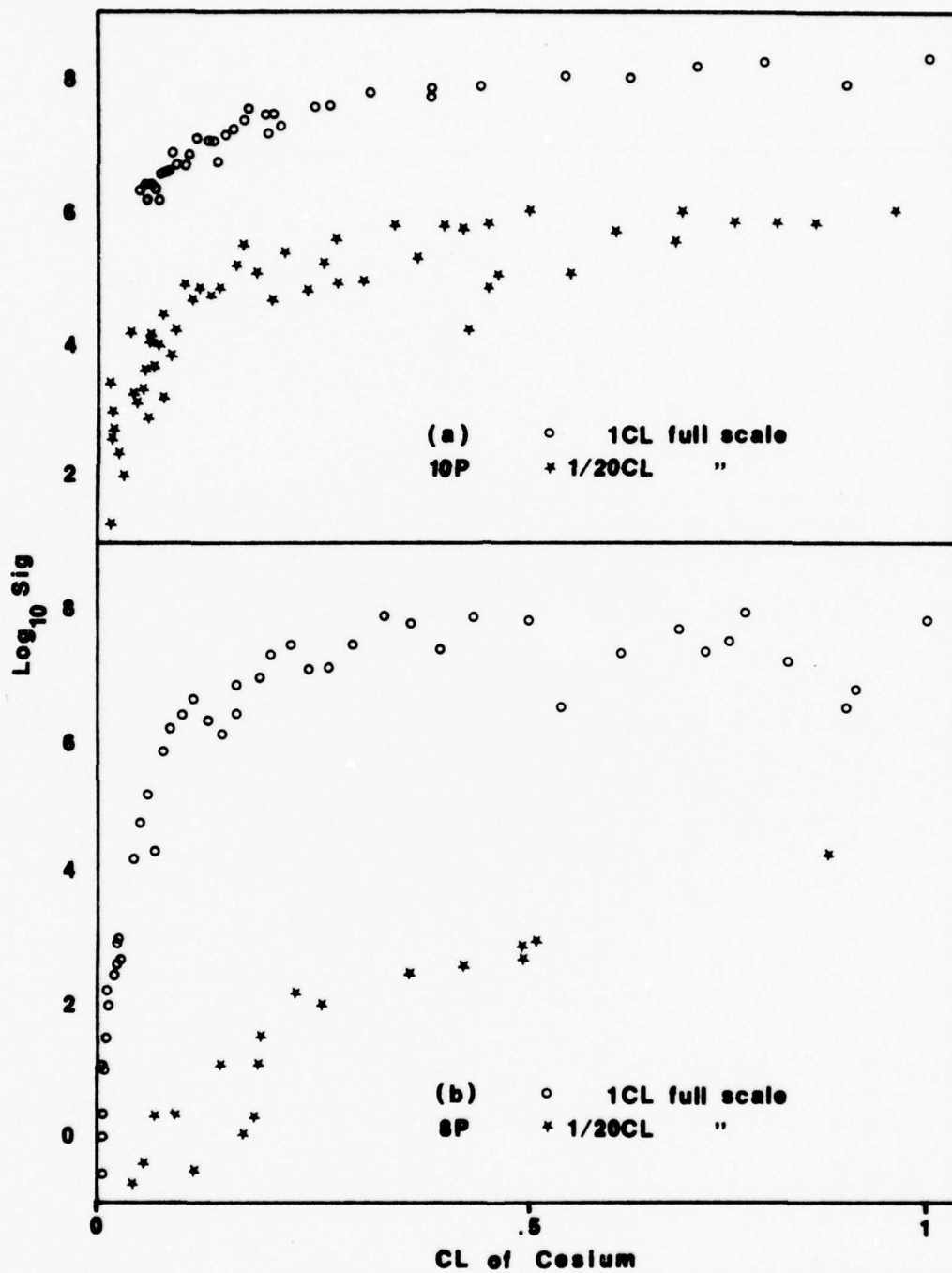


Fig. 5.5

Variation of 10P and 8P signal intensities
with Cs density at 10^6 watts pump power.

Note expanded scale for stars.

lines and estimate the pump threshold powers and these values are then compared with those computed in chapter three. From figs. 5.3 and 5.4, the small signal gains at a density corresponding to one coherence length are found to be in proportion of 1, .5, .3, .2 and for the 10P, 9P, 8P and 7P lines respectively and the gain for the 10P line is approximately 200 decades/MW. From fig. 5.5, the experimental small signal gain as a function of density at a constant laser power of one megawatt is 750 decades/CL for the 10P line and 250 decades/CL for the 8P line. The experimental parametric thresholds are estimated from figures 5.3 and 5.4 to lie in the range of 10 - 20 kW for all four lines. These measured values are listed in Table 5.1 next to the values calculated in chapter three.

Recall that the calculated expression for the gain of the $10P_{\frac{1}{2}}$ line was

$$\text{gain}_e = 51 \cdot P \cdot N \quad (5.1)$$

where P is in Mw and N is in coherence lengths, so the small signal power gain is 22 decades/MW if N is unity or 22 decades/CL if P is one megawatt. The gains of the other lines were calculated relative to this and since the $j = \frac{1}{2}$ lines always have greater gain than the $j = \frac{3}{2}$ lines, only the former are listed. Threshold powers were estimated by calculating the power at which parametric gain

Table 5.1

Line	Power Gain (Decades/Mw)		Density Gain (Decades/CL)		Threshold Power (Kilowatts)	
	EXP.	THEOR.	EXP.	THEOR.	EXP.	THEOR.
10P	200	22	750	22	10 - 20	60
9P	100	21			10 - 20	170
8P	70	28	250	28	10 - 20	620
7P	40	65			10 - 20	2,700
6P	0	1,150			-----	40,000

overcomes linear loss of the signal due to $6S - nP$ absorption.

Comparison of the power gains listed in the table indicates that the experimental small signal power gain of 10P is a factor of ten larger than the calculated gain and the gain measured for the other three signals decrease with decreasing signal frequency while the calculations indicate the gain should increase. The factor of 10 difference in absolute gains is within uncertainties of calibration or calculation, but the trends of gain with signal frequency are significant because they are independent of the uncertainties.

Comparison of the density gains reveals a similar pattern. The ratio of the measured 10P to 8P gain is about 3:1 while the calculated ratio is about 3:4. In this instance, however, the difference of 750 to 22 in absolute gain of 10P is even larger than for the power gain. Threshold powers, listed in the last two columns, also show discrepancy between theory and experimental values.

Finally, perhaps the most striking feature of the data in figures 5.3 to 5.5, is the saturation in signal power evident in each instance. Saturation always occurs at powers of about a watt although the shape is somewhat different for the density curves (fig. 5.5) than for the power curves (figs. 5.3 and 5.4).

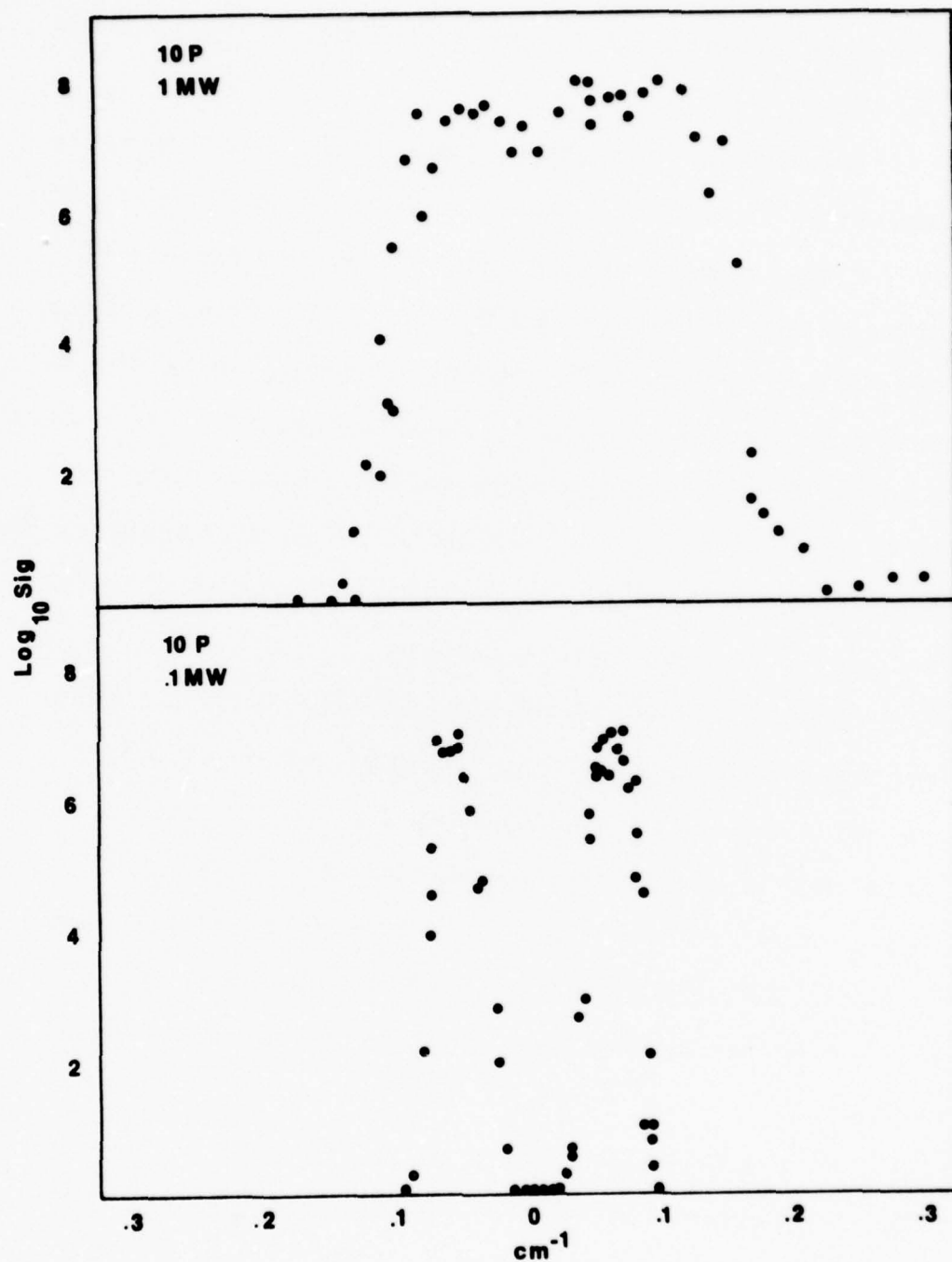


Fig. 5.6

Variation of 10P signal intensity with laser frequency at 10^5 watts (lower) and 10^6 watts (upper).

5.3 Limitations of Theory and Modifications

In calculating the parametric gain, lineshape and threshold power in chapter three, we assumed that all cesium atoms were in the ground state. However, since we have shown that population in other states, especially $9D_{3/2}$, is important in other nonlinear processes, we should modify the theory to include that possibility. When $9D_{3/2}$ is populated as well as $6S$, the susceptibilities for signal and idler frequencies become

$$\chi_S = N_6 \chi_S(6S) + N_9 \chi_S(9D) \quad (5.1)$$

$$\chi_I = N_6 \chi_I(6S) + N_9 \chi_I(9D)$$

where N_6 is the number of atoms in $6S$ and N_9 is the number in $9D_{3/2}$. Thus²

$$\begin{aligned} \chi_S &\propto \frac{N_6}{(\Omega_{96} - 2\omega_P)(\Omega_{P6} - \omega_S)} + \frac{N_9}{(\Omega_{96} - 2\omega_P)(\Omega_{9P}^* - \omega_I)} \\ \chi_I &\propto \frac{N_6}{(\Omega_{96}^* - 2\omega_P)(\Omega_{P6} - \omega_S)} + \frac{N_9}{(\Omega_{9P}^* - \omega_I)(\Omega_{96}^* - 2\omega_P)} \end{aligned} \quad (5.2)$$

The Doppler averaged susceptibilities $\langle \chi_S \rangle$ and $\langle \chi_I^* \rangle$ each have a narrow, tall spike at $\omega_S = \omega_{P6}$ when $2\omega_P = \omega_{96}$ similar to that described and graphed in chapter 3. This

spike comes from the 9D term of $\langle \chi_S \rangle$ and the 6S term of $\langle \chi_I^* \rangle$. The product $\langle \chi_S \rangle \langle \chi_I^* \rangle$ therefore also has a large spike at $\omega_S = \omega_{PS}$ of amplitude $\langle \chi_S(9D) \rangle \langle \chi_I^*(6S) \rangle \cdot N_9 \cdot N_6$ which causes a large gain at linecenter. This replaces the dip which appears at linecenter when N_9 or N_6 is zero. The maximum amplitude of the gain is then larger than the previously calculated maximum by a factor of approximately $(\Delta\omega_{\text{Doppler}} / \Delta\omega_{\text{Homogeneous}}) \cdot \sqrt{N_6 N_9}$ so the gain is very sensitive to the homogeneous widths and hence to laser power and cesium density.

The complete description of the gain profile and its variation with power and density requires more detailed knowledge of the homogeneous widths than is available. We can, however, by making certain reasonable assumptions, determine whether including the $9D_{3/2}$ population leads to a more accurate description of the parametric process. In the range of laser power over which the parametric signals are observed ($10^4 - 10^6$ watts), we found in analyzing THG and TPA that the fraction of atoms in $9D_{3/2}$ varies from perhaps .1 to .5. Depending on the linewidths involved, even the lower value of .1 could be sufficient to significantly enhance the parametric gain. In this case, if the homogeneous linewidths of the P states increase with decreasing principal quantum number, the gain would tend to be larger for higher frequency signal waves as observed (see table 5.1) instead of lower as would be the case when $N_9 = 0$.

The effect of $9D_{\frac{3}{2}}$ population also provides a reasonable explanation of the difference in the power and density gains (see table 5.1). The density gain is measured at low densities and high power while the power gain is measured at high density and low power. The density gain should thus be greater than the power gain both because the homogeneous widths are less at low density and because the $9D$ population is larger at high laser intensities.

When $9D$ is populated, the increase in parametric gain, the decrease in linear absorption of the signal wave and the contribution to the idler linear gain all contribute in lowering threshold powers from those calculated for a $6S$ only population (see table 5.1) so it is not surprising that the thresholds are lower than had been predicted.

We conclude that including a $9D_{\frac{3}{2}}$ population in the simple perturbation calculation of parametric gain results in a significantly improved description of the observed low power gains and threshold powers. Exact calculations are not possible given our lack of knowledge of homogeneous linewidths but reasonable values suffice.

Might this or a similar mechanism also explain the saturation of the signals at about a watt? If so, judging from the shape of the gain curves (see figs. 5.3 - 5.6), it must depend primarily on the strength of the signal or

idler itself rather than the laser power or the cesium density. This suggests that population of the P state, either by absorption of the signal wave by atoms in 6S, or by emission of idler by $9D_{3/2}$ atoms, is responsible. Such a P state population might reduce the gain substantially. Under certain conditions the gain can become zero when the populations of 6S, $9D_{3/2}$, and nP are equalized. Calculations show that approximate equalization of populations can occur via signal wave absorption by 6S atoms if the signal powers are approximately 1, 15, 70, 180 watts for the 7P, 8P, 9P, or 10P lines respectively. Although 180 watts is considerably larger than the actual saturated value of 1 - 10 watts, this is a more likely saturation mechanism than population of nP by decay of $9D_{3/2}$ since population of 7P by $9D_{3/2}$ - 7P transitions would require the emission of 500 watts of 3 μ m radiation whereas we measured about .1 watts at this wavelength.

Thus far we have compared our observations only with calculations of parametric gain. Other processes such as lasing or Raman gain at the idler frequency in conjunction with difference frequency generation at the signal frequency, or lasing at the signal frequency must be considered. These are compared with the parametric process below and rejected as the dominant process.

The existence of populations in excited atomic states admits the possibility of lasing action at various

frequencies including idler or signal. The expressions for gain described in chapter three take into account any changes in linear loss or gain due to population shifts via the inclusion of Δk so lasing should not be considered a process independent of parametric mixing. Nevertheless, if lasing gain is much larger than parametric gain, the process resembles lasing rather than parametric gain. In this extreme, gain in the reverse direction would be equal to that in the forward direction, for example, and phase mismatch would lead to modulation of waves produced by mixing the lasing and the pump waves. Raman gain shares these characteristics. Parametric gain, in contrast, is much larger in the forward than reverse direction and modulation is absent.

To verify that we are observing a parametric process rather than lasing or Raman gain, we have looked for signal and idler waves propagating in the reverse direction and find that the combined signal wave intensity is less than a thousandth that in the forward direction. Thus lasing at the signal frequency is not significant. The ratio for the 3 μm idler, on the other hand, is between 3 and 10 although there is considerable uncertainty in this measurement. On this basis, it would seem that lasing or Raman gain at the idler could make a significant contribution. However, the temporal dependence of the signal exhibits little of the spikey or noisy appearance

associated with superradiant emission; the modulation of the signal instead follows that of the laser quite well as expected for parametric gain. Additionally, if the signals are attributed to lasing at the idler frequency it is estimated that the strength of the idler at which saturation due to depletion of $9D_{3/2}$ atoms should occur is about 500 watts for the 3 μ m line instead of approximately .1 watt.

A third possible lasing process, two-photon stimulated emission from state $9D_{3/2}$ to 6S, would produce signal and idler frequency photons because of the resonant enhancement provided by the P states. This process is ruled out because no signal wave is observed in the reverse direction and because population inversion between $9D_{3/2}$ and 6S is unlikely.

We conclude that lasing and Raman gain are not dominant in the production of the radiation we have studied. That is, the contribution of population inversions to Δk is not so large that the process resembles lasing although population shifts are large enough to create power dependent changes in Δk .

Our analysis has been based on a steady state model and the further idealizations of a parallel undepleted pump beam, no significant Stark shifts, no diffraction losses of the idler, or absorption of the idler by Cs_2 molecules, or ionization losses. In principle the system

could be described completely by the solution of the equations of motion of the density matrix including these effects and all the relevant atomic states of cesium. This would take into account population shifts generated by the four parametric processes as well as linear gain or loss, Raman processes, ionization losses, beam geometries and so on. At this stage we are content with a qualitative explanation of the main features. If a more detailed investigation is desired, it should be undertaken in a more suitable experimental system in which competing processes and complications introduced by loss of atoms and frequency shifts are minimized.

5.4 Summary & Conclusions

We have made the first detailed measurements of the power and density dependence of the intense resonant radiation generated in an atomic vapor pumped by a powerful laser. In particular we have studied them in cesium vapor pumped by a ruby laser tuned near the $6S - 9D_{3/2}$ two-photon resonance. These measurements are shown to be in reasonable agreement with a simple steady state calculation of the parametric gain for small signal and idler intensities. Considering the extremely complex nature of the actual interaction which involves four signal and idler fields all simultaneously present and interacting with one another through the various state populations,

and the possibility of lasing between various levels and possible higher order processes, these calculations are not expected to yield a precise fit to the data, but we believe we have demonstrated the existence of parametric gain, and we have made a detailed investigation of saturation and qualitatively explained the saturation mechanism.

APPENDIX A

STEADY STATE DENSITY MATRIX CALCULATION

Expressions describing third harmonic generation and two photon absorption which are applicable to our experimental situation are derived in this appendix. The density matrix formulation is used and a steady state solution is assumed. Doppler averaging is included. The model quantum system upon which the calculation is based consists of an electromagnetic field of angular frequency ω incident upon a multilevel quantum system consisting of levels $6S_{\frac{1}{2}}$, $9D_{\frac{3}{2}}$, and the series of states nP (see fig. A.1). Only states $6S_{\frac{1}{2}}$

and $9D_{\frac{3}{2}}$ are allowed to have significant populations.

First the populations of the states $6S_{\frac{1}{2}}$ and $9D_{\frac{3}{2}}$ will be calculated, then the expectation value of the dipole matrix element $\mu(3\omega)$ is derived. The former is related to the amount of TPA; the latter to the THG signal.

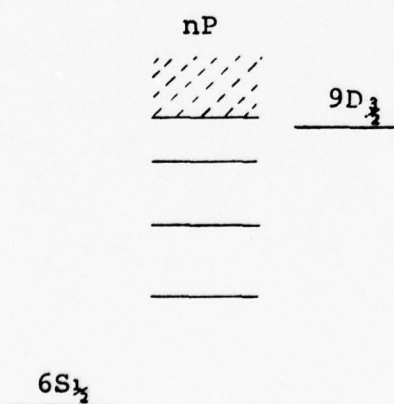


fig. A.1

The density matrix ρ is defined in the conventional manner so ρ_{nn} is the population in state n and the expectation value of the operator A is given by $\langle A \rangle = \text{Trace}\{\rho A\}$.

TPA

The equations of motion used to find ρ_{22} (the population in state $9D_{3/2}$) are

$$\begin{aligned}
 i\hbar\dot{\rho}_{12} &= \hbar\omega_{12}\rho_{12} + [H, \rho]_{12} - \frac{i\hbar}{T_2} \rho_{12} \\
 i\hbar\dot{\rho}_{21} &= -\hbar\omega_{12}\rho_{21} + [H, \rho]_{21} - \frac{i\hbar}{T_2} \rho_{21} \\
 i\hbar\dot{\rho}_{11} &= [H, \rho]_{11} + \frac{i\hbar}{T_1} \rho_{22} \\
 i\hbar\dot{\rho}_{22} &= [H, \rho]_{22} - \frac{i\hbar}{T_1} \rho_{22} \\
 \rho_{11} + \rho_{22} &= 1
 \end{aligned} \tag{A.1}$$

where T_1 is the lifetime of state 2, T_2 is the lifetimes of ρ_{12} and ρ_{21} , and H is the perturbation Hamiltonian.

$$H = \frac{-e^2}{\hbar} \begin{bmatrix} 0 & d_{12} \\ d_{21} & 0 \end{bmatrix} \frac{1}{4} (E e^{-i\omega t} + E^* e^{i\omega t})^2 \tag{A.2}$$

where $d_{12} = d_{21}^*$ and

$$|d_{12}|^2 = 2 \left| \sum_n \frac{\langle 1 | z | nP \rangle \langle nP | z | 2 \rangle}{\Omega_{nP} - \omega} \right|^2 \tag{A.3}$$

If a steady state solution is assumed ($\dot{\rho}_{11} = \dot{\rho}_{22} = 0$) and ρ has the form

$$\rho = \begin{bmatrix} \rho_{11} & \rho_{12} e^{-2i\omega t} \\ \rho_{21} e^{2i\omega t} & \rho_{22} \end{bmatrix} \quad (\text{A.4})$$

then the set of equations A.1 may be solved for ρ . The result is

$$\rho_{12} = \frac{1}{4} (e/\hbar)^2 \frac{d_{12} e^{-2i\omega t} (\rho_{11} - \rho_{22}) E^2}{2\omega - \omega_{12} + \frac{i}{T_2}} \quad (\text{A.5})$$

$$\rho_{11} - \rho_{22} = \left[1 + \frac{T_1}{T_2} (e/\hbar)^4 \frac{|d_{12}|^2 (|E|^2)^2}{(2\omega - \omega_{12})^2 + (1/T_2)^2} \right]^{-1} \quad (\text{A.6})$$

If the quantities S and D are defined as

$$S \equiv \frac{1}{4} T_1 T_2 (e/\hbar)^4 |d_{12}|^2 (|E|^2)^2 \quad (\text{A.7})$$

$$D \equiv (2\omega - \omega_{12})^2 + (1/T_2)^2 \quad (\text{A.8})$$

then the expression for $(\rho_{11} - \rho_{22})$ and ρ_{22} may be written

$$\rho_{11} - \rho_{22} = \frac{1}{1 + S/(DT_2^2)} \quad (\text{A.9})$$

$$\rho_{22} = \frac{S}{2T_2^2} \frac{1}{D + S/T_2^2} \quad (\text{A.10})$$

When $2\omega = \omega_{12}$, the expression for ρ_{22} becomes

$$\rho_{22} = \frac{1}{2} \frac{S}{1 + S} \quad (\text{A.11})$$

This describes the population in state 2 for exact resonance tuning. At low field intensities of the applied field, ρ_{22} is proportional to the square of the intensity while at very high intensities it is .5. When the incident radiation is detuned away from the resonance, ρ_{22} decreases from its resonant value. Equation A.10 describes the shape of the resonance. It has a Lorentzian lineshape with the FWHM value of $2\sqrt{1 + S}/T_2$. Thus the linewidth is $2/T_2$ at low intensities but broadens in proportion to the intensity when S is much larger than unity.

Doppler averaging will now be included. The Doppler averaged form of eqn. A.10 is

$$\langle \rho_{22} \rangle = \frac{S}{\sqrt{1 + S}} \frac{1}{2T_2} \frac{1}{\Delta\omega_2} z''(x, y) \quad (\text{A.12})$$

where

$$\Delta\omega_2 \equiv 2\omega_{12} \{2kT/Mc^2\}^{1/2} \quad (\text{A.13})$$

and $Z''(x,y)$ is the imaginary part of the Plasma Dispersion Function with the arguments

$$x = \frac{\omega_{12} - 2\omega}{\Delta\omega_2} \quad y = \frac{\sqrt{1+S}}{T_2 \Delta\omega_2} \quad (\text{A.14})$$

Finally, note that the fluorescence from state 2 is proportional to $\langle \rho_{22} \rangle$ so the TPA signal is

$$\text{TPA} \propto \langle \rho_{22} \rangle = \frac{S}{\sqrt{1+S}} \frac{1}{2T_2 \cdot \Delta\omega_2} \quad (\text{A.15})$$

THG

The polarization at the frequency 3ω is proportional to the 3ω component of the expectation value of the dipole transition operator μ . Since the expectation value is found from

$$\langle \mu \rangle = \text{Trace}(\rho\mu) \quad (\text{A.16})$$

we must find the third harmonic components of ρ . This is done by solving the equations of motion of ρ in the presence of a second perturbation Hamiltonian H_2 . For simplicity only one of the nP states is considered. It is labeled state 3. Later the contributions from each of the nP states will be added to produce the total $\langle \mu(3\omega) \rangle$.

$$H_2 = -\frac{e}{2} (E e^{-i\omega t} + E^* e^{i\omega t}) \begin{bmatrix} 0 & 0 & 0 \\ 0 & 0 & \mu_{23} \\ 0 & \mu_{32} & 0 \end{bmatrix} \quad (\text{A.17})$$

The equations of motion ρ are displayed below where ρ_{11} , ρ_{22} , ρ_{12} and ρ_{21} are assumed to have the values calculated above.

$$\begin{aligned} i\hbar \dot{\rho}_{13} &= \hbar\omega_{13}\rho_{13} + [H_2, \rho]_{13} - \frac{i\hbar}{T_3} \rho_{13} \\ i\hbar \dot{\rho}_{31} &= -\hbar\omega_{31}\rho_{31} + [H_2, \rho]_{31} - \frac{i\hbar}{T_3} \rho_{31} \end{aligned} \quad (\text{A.18})$$

These are solved for ρ_{31} and ρ_{13} and used in

$$\langle \mu(3\omega) \rangle = \text{Trace}(\rho \mu_{13}) = \rho_{13} \mu_{31} + \rho_{31} \mu_{13} \quad (\text{A.19})$$

The result is

$$\begin{aligned} \langle \mu(3\omega) \rangle &= (e/2\hbar) \frac{\mu_{13}\mu_{32}d_{21} E^{*3} e^{3i\omega t} (\rho_{11} - \rho_{22})}{(\omega_{13} - 3\omega + iT_3^{-1})(\omega_{12} - 2\omega + iT_2^{-1})} \\ &\quad + \text{complex conjugate} \end{aligned} \quad (\text{A.20})$$

The terms $\frac{\mu_{13}\mu_{32}}{(\omega_{13} - 3\omega + iT_3^{-1})}$ must now be replaced by a

sum of similar terms, one from each of the nP states, plus a continuum contribution.

Since $\chi(3\omega; \omega, \omega, \omega) E e^{i3\omega t}$ is the second term of eqn. A.20 and $\text{THG} \propto |\langle \chi \rangle|^2$,

$$\text{THG} \propto P_{\omega}^3 \left| \left\langle \frac{1}{1 + S/(DT_2^2)} \frac{1}{\omega_{12} - 2\omega - iT_2^{-1}} \right\rangle \right|^2 \quad (\text{A.21})$$

Performing the Doppler averaging yields⁹

$$\text{THG} \propto \frac{P_{\omega}^3}{(\Delta\omega_g)^2} \left\{ Z'^2(x, y) + \frac{1}{1 + S} Z''^2(x, y) \right\} \quad (\text{A.22})$$

where D , $\Delta\omega_g$, x , y and z are defined above.

APPENDIX B

PHOTOIONIZATION OF $9D_{3/2}$ AND $6S_{1/2}$ STATES IN ATOMIC CESIUM

The calculation of the rates of photoionization of the $9D_{3/2}$ state of cesium by 14414 cm^{-1} radiation and of the $6S_{1/2}$ state by 43243 cm^{-1} radiation (14414 cm^{-1} is the wave number of the ruby laser and 43243 is its third harmonic) is outlined in this appendix.

The method of calculation is the quantum defect method of Peach.¹⁷ Equation 23 of Peach gives the following formula for the photoionization cross section σ of an atom:

$$\sigma_{\tilde{\nu}}(\epsilon', \nu) = \frac{8\alpha a_0 \nu^3}{3z^2 \zeta(\nu, l)} \{1 + \epsilon' \nu^2\}^3. \quad (\text{B.1})$$

$$\sum_{l'=l \pm 1} C_{l'} [G(\nu l; \epsilon' l') \cos \pi \{ \nu + \mu'(\epsilon') + X(\nu l; \epsilon' l') \}]^2$$

The quantities have the following definitions:

unprimed state is bound state; primed state is

ionized state

$$\alpha = e^2 / \hbar c; \quad a_0 = .529 \times 10^{-8} \text{ cm}$$

$$\tilde{\nu} = \text{frequency of radiation}$$

$$\epsilon' = \text{kinetic energy of ejected } e^- \text{ in Rydberg units}$$

$$z = \text{charge of core} = 1 \text{ for neutral cesium}$$

$$\nu = \text{effective principal quantum number}$$

$$\text{ie. } \nu^2 = z^2 / I_{nl}$$

I_{nl} = threshold ionization energy of nl electron
in Rydbergs

n = actual principal quantum number

μ = $n - \mu$; μ is called the quantum defect
 $\mu'(\epsilon')$ is the extrapolated quantum defect
in the continuum

$C_{\ell'}$ = a coefficient depending on ℓ and ℓ'

$$C_{\ell'} = \begin{cases} (\ell + 1)/(2\ell + 1) & \ell' = \ell + 1 \\ \ell/(2\ell + 1) & \ell' = \ell - 1 \end{cases}$$

$$\zeta(v, \ell) = 1 + \frac{2}{v^3} \frac{\partial \mu(\epsilon)}{\partial \epsilon}$$

G and X are tabulated by Peach for $\ell, \ell' \leq 3$

In order to calculate the cross section for a particular case one calculates v , ϵ' , and $C_{\ell'}$, and estimates the value of $\mu'(\epsilon')$ by extrapolating from $\mu(\epsilon)$ (the quantum defect of the bound states) and estimates $\zeta(v, \ell)$. The values of $G(v\ell; \epsilon' \ell')$ and $X(v\ell; \epsilon' \ell')$ are interpolated from the tables of Peach. The results are expected to be correct to within a few percent for the calculations of interest here.

The formula above did not include fine structure. This can be included, however, by using the following values (which are correct for atoms which are excited to state $9D_{3/2}$ by linearly polarized light and ionized by light of the same polarization or for atoms ionized from the state $6S_{1/2}$ by polarized light) in place of $C_{\ell'}$.

$$\begin{aligned}
 C(S_{\frac{1}{2}} \rightarrow \text{Continuum P}) &= 1 \\
 C(D_{\frac{3}{2}} \rightarrow \text{Continuum P}) &= 17/25 \\
 C(D_{\frac{3}{2}} \rightarrow \text{Continuum F}) &= 18/25
 \end{aligned}
 \tag{B.2}$$

The values of the ionization rates which were calculated in this manner are:

$$\begin{aligned}
 W(9D_{\frac{3}{2}} m_j = \pm \frac{1}{2} \rightarrow \text{Continuum P}) &= \\
 &.457 \text{ I sec}^{-1} ; \lambda = 693.5 \text{ nm} \\
 W(9D_{\frac{3}{2}} m_j = \pm \frac{1}{2} \rightarrow \text{Continuum F}) &= \\
 &7.16 \text{ I sec}^{-1} ; \lambda = 693.5 \text{ nm} \\
 W(6S_{\frac{1}{2}} \rightarrow \text{Continuum P}) &= \\
 &.33 \text{ I sec}^{-1} ; \lambda = 231.4 \text{ nm} \\
 &(\text{I in watts/cm}^2)
 \end{aligned}
 \tag{B.3}$$

APPENDIX C

A.C. STARK SHIFTS OF THE $6S_{\frac{1}{2}}$ AND $9D_{\frac{3}{2}}$ STATES OF ATOMIC CESIUM BY 693.5 nm RADIATION

This appendix contains the outline of the calculation of the Stark shifts induced by the ruby laser radiation field (at 693.5 nm) on the $6S_{\frac{1}{2}}$ and $9D_{\frac{3}{2}}$ states of cesium. The shift of a state is proportional to the linear polarizability of that state so there is a contribution to the shift from the bound electron states and from the continuum states. First, the bound state contribution is calculated for both states ($9D_{\frac{3}{2}}$ and $6S_{\frac{1}{2}}$) and later the continuum contribution is calculated. Linear polarization of the radiation field is assumed and only the shift of $m_j = \pm \frac{1}{2}$ states is of interest (states of different m shift by different amounts.)

Bound State Contributions

The size of an A.C. Stark shift is given by

$$\Delta E_{nljm_j} = \alpha_{nljm_j} I \cdot (1.05 \times 10^{-11}) \quad (C.1)$$

where I is in watts/cm², ΔE is in cm⁻¹, and α is in (A⁰)³. α_{nljm_j} will be written $\tilde{\alpha}$ below since it is not the polarizability as usually defined but is the polarizability of a particular m_j state for linearly polarized

light. The definition of $\tilde{\alpha}$ is

$$\tilde{\alpha} = \frac{2Ne^2}{\hbar} \sum_i \{ |\langle n'\ell's'j'm_j | z | n\ell s j m_j \rangle|^2 \cdot (\omega') / (\omega'^2 - \omega^2) \} \quad (C.2)$$

where ω' is the transition frequency between the initial and final states and the sum is over final states.

This definition is to be contrasted with the usual definition of polarizability which is just the average of $\tilde{\alpha}$ over the m_j states, ie.,

$$\alpha = \frac{1}{2j+1} \sum_{m_j} \tilde{\alpha} \quad (C.3)$$

It can be shown that $\tilde{\alpha} = C\alpha$ where C is listed below.

<u>Transition</u>	<u>C</u>	<u>Transition</u>	<u>C</u>
$D_{3/2} \rightarrow P_{1/2}$	2	$S_{1/2} \rightarrow P_{1/2}$	1
$D_{3/2} \rightarrow P_{3/2}$	1/5	$S_{1/2} \rightarrow P_{3/2}$	1
$D_{3/2} \rightarrow F_{5/2}$	6/5		

Now α is related to f numbers by

$$\alpha = \frac{Ne^2}{m} \sum_i \frac{f_i}{\omega_i^2 - \omega^2} \quad (C.4)$$

where

$$f = \frac{8\pi^2 mc}{3\hbar e^2 \lambda} \frac{S}{2j + 1} \quad (C.5)$$

$$S = \sum_{\substack{m_j' \\ m_j}} |\langle n' \ell' s' j' m' | r | n \ell s j m_j \rangle|^2 \quad (C.6)$$

The values of f for the various transitions can be calculated in the Coulomb approximation by the methods of Bates and Damgaard¹⁸ or taken from Stone.¹⁹ Then α can be calculated and $\tilde{\alpha}$ follows. The discrete state contribution to the $\tilde{\alpha}$'s calculated in this manner are listed below.

$$\begin{aligned} \tilde{\alpha} 9D_{\frac{3}{2}} (m_j = \pm \frac{1}{2}) &= -28.43 \text{ A}^0{}^3; \text{ Coul. } f\# \text{'s, } \lambda = 693.5 \text{ nm} \\ \tilde{\alpha} 6S_{\frac{1}{2}} &= -100.02 \text{ A}^0{}^3; \text{ Coul. } f\# \text{'s, } \lambda = 693.5 \text{ nm} \\ \tilde{\alpha} 6S_{\frac{1}{2}} &= -116.03 \text{ A}^0{}^3; \text{ Stone } f\# \text{'s, } \lambda = 693.5 \text{ nm} \end{aligned}$$

Continuum States Contribution

From the Kramers - Kronig relations it can easily be shown that

$$\alpha(\omega_0) = \int_0^\infty \frac{1}{4\pi^3} \frac{1}{109737} \frac{\sigma(\omega') d\omega'}{\omega'^2 - \omega_0^2} \quad (C.7)$$

where the units are $[\sigma] = \text{cm}^2$, $[\omega] = \text{Rydbergs}$, $[\alpha] = \text{cm}^3$.

The formula for finding σ is contained in Appendix B equation B.1. According to the definitions used there,

$$\omega' = \varepsilon' + \frac{1}{v^2} \quad \text{and} \quad \omega_0 = \varepsilon_0 + \frac{1}{v^2} \quad (\text{C.8})$$

Combining equation B.1 with C.7 and C.8 yields

$$\tilde{\alpha}(\omega_0) = 4.00 \times 10^{-26} . \quad (\text{C.9})$$

$$\int_0^\infty d\varepsilon' \frac{v^7 \sum C^* \{G \cos \pi(v + \mu' + \chi)\}^2}{\zeta \{1 + \varepsilon' v^2\}^3 \{(\varepsilon' v^2 + 1)^2 - (\varepsilon_0 v^2 + 1)^2\}}$$

where $\tilde{\alpha}$ is in units cm^3 .

Using the tables of Peach for G and χ this expression has been evaluated to be

$$\begin{aligned} \tilde{\alpha} \{9D_{3/2}(m_j = \pm \frac{1}{2}) \rightarrow \text{Continuum P}\} &= -1.38 \text{ A}^0{}^3 \text{ at } 693.5 \text{ nm} \\ \tilde{\alpha} \{9D_{3/2}(m_j = \pm \frac{1}{2}) \rightarrow \text{Continuum F}\} &= -3.13 \text{ A}^0{}^3 \text{ at } 693.5 \text{ nm} \\ \tilde{\alpha} \{6S_{1/2} \rightarrow \text{Continuum P}\} &= +0.69 \text{ A}^0{}^3 \text{ at } 693.5 \text{ nm} \\ \tilde{\alpha} \{6S_{1/2} \rightarrow \text{Continuum P}\} &= -0.006 \text{ A}^0{}^3 \text{ at } 231.4 \text{ nm} \end{aligned}$$

Total Stark Shift

When these values for $\tilde{\alpha}$ are used to find the shifts, using equation C.1, it is found that both states shift to lower energy but $6S_{1/2}$ shifts more so the separation between the states is increased by

$$\Delta(\Delta E) = \left[\begin{array}{ll} 67.77 \text{ A}^{\circ 3} & \text{Coul.} \\ 83.78 \text{ A}^{\circ 3} & \text{Stone} \end{array} \right] \times .315 \text{ I} \quad (\text{C.10})$$

where ΔE is in Mhz, I is in MW/cm^2 , and $\tilde{\alpha}$ is in $\text{A}^{\circ 3}$.

REFERENCES

1. J. A. Giordmaine, *Scientific American* 4, 38 (1964).
P. A. Franken and J. F. Ward, *Rev. Mod. Phys.* 35, 23 (1963).
N. Bloembergen, Nonlinear Optics (Benjamin Book Co. Inc., 1965).
2. B. J. Orr and J. F. Ward, *Molecular Physics* 20, 513 (1971).
3. R. T. Hodgson, P. P. Sorokin, and J. J. Wynne, *Phys. Rev. Lett.* 32, 343 (1974).
D. M. Bloom, James T. Yardley, J. F. Young, and S. E. Harris, *App. Phys. Lett.* 24, 427 (1974).
I. D. Abella, *Phys. Rev. Lett.* 9, 453 (1962).
A. Penzkofer, A. Laubereau, and W. Kaiser, *Phys. Rev. Lett.* 31, 863 (1973).
Peter P. Sorokin and John R. Lankard, *IEEE Jour. Quant. Elec.* QE-9, 227 (1973).
4. K. M. Leung, Thesis (University of Michigan, Ann Arbor) (1972).
5. I. J. Bigio, Thesis (University of Michigan, Ann Arbor) (1974).
6. J. R. Izatt, R. C. Mitchell, H. A. Daw, *J. App. Phys.* 37, 1558 (1966).
7. D. Peterson and A. Yariv, *Applied Optics* 5, 985 (1966).
8. B. J. Orr, (private communication).
9. B. D. Fried and S. D. Conte, The Plasma Dispersion Function (Academic Press, Ltd., 1961).
10. A. Yariv and J. Pearson, *Progress in Quantum Electronics* 1, 1 (1969). Ed. K.W.H. Stevens and J.H. Sanders (Pergamon Press Ltd.).
11. M. S. Feld and A. Javan, *Phys. Rev.* 177, 540 (1969).

12. J. F. Ward and A. V. Smith, Phys. Rev. Lett. 35, 653 (1975).
13. J. N. Elgin and G. H. C. New, Optics Comm. 16, 242 (1976).
E. A. Stappaerts, Phys. Rev. A 11, 1664 (1975).
A. T. Georges, P. Lambropoulos, J. H. Marburger, Phys. Rev. A 15, 300 (1977).
14. A. T. Georges, P. Lambropoulos, J. H. Marburger, Phys. Rev. A 15, 300 (1977).
15. S. Svanberg, P. Tsekeris, W. Happer, Phys. Rev. Lett. 30, 817 (1973).
16. A. Penzkofer, A. Laubereau, and W. Kaiser, Phys. Rev. Lett. 31, 863 (1973).
Peter P. Sorokin and John R. Lankard, IEEE Jour. Quant. Elec. QE-9, 227 (1973).
17. G. Peach, Mem. Ray. Astro. Soc. 71, 13 (1967).
18. D. R. Bates and A. Damgaard, Phil. Trans. Ray. Soc. London A242, 101 (1949).
19. P. Stone, Phys. Rev. 127, 1151 (1962).